

Numerical modeling of the thermal force for impurity transport in fusion plasmas

March 2014

Yuki HOMMA

学位論文

博士（工学）

慶應義塾大学大学院 理工学研究科

Numerical modeling of the thermal force
for impurity transport in fusion plasmas

2014年3月

本間 裕貴

主 論 文 要 旨

報告番号	甲 乙 第	号	氏 名	本間 裕貴
主 論 文 題 目： Numerical modeling of the thermal force for impurity transport in fusion plasmas (核融合プラズマ中の不純物輸送に関する熱力の数値モデリング)				
(内容の要旨) 次世代エネルギー源の一つとして期待される制御熱核融合発電の実現には、高温・高密度プラズマを生成し、長時間磁場中に閉じ込め、維持することが必要である。しかし、プラズマ閉じ込め容器壁で発生した不純物粒子が高温のコアプラズマに混入すると、プラズマ温度は低下し、核融合反応の維持が困難となる。従って、境界層プラズマ中の不純物輸送現象のモデル化とコアプラズマへの混入量の予測は必要不可欠であり、従来から世界各国で様々な不純物輸送シミュレーションコードの開発が行われてきた。しかしながら、急峻な温度勾配が存在する境界層プラズマにおいて、不純物粒子とプラズマイオンとのクーロン相互作用が原因となり生じる熱力と、この熱力に起因する不純物輸送に関する数値シミュレーションモデルは、十分正確とは言いがたかった。特に、閉じ込め磁場に垂直な方向の熱力による境界層プラズマ中の不純物輸送は、従来の運動論的数値シミュレーションにおいては全く考慮されていなかった。以上を踏まえ、本研究では、境界層プラズマ中の熱力による不純物輸送に関する新たな数値シミュレーションモデルを開発し、プラズマ中への不純物混入量に関する信頼性の高い予測シミュレーション実現に寄与することを目的とした。 第1章では、本研究の背景と目的・意義を述べた。 第2章では、本研究の基礎となるプラズマ中のテスト荷電粒子の運動論モデルについてまとめた。このモデルでは、テスト不純物粒子と背景プラズマ粒子群とのクーロン衝突による運動量変化を速度空間における速度ベクトルの酔歩過程として定式化した。解析的な扱いが可能な、密度が一定、かつ、線形な温度勾配を持つ背景プラズマの場合について運動量変化の期待値を求め、熱力の理論式を導き、典型的な核融合プラズマ中での熱力の大きさを計算し、まとめた。 第3章では、第2章の酔歩モデルおよび多体問題を二体問題に帰着させる、いわゆる「二体衝突モデル」に基づき、本研究で新たに開発した熱力の数値シミュレーションモデルについて説明した。本章では、特に磁力線に平行な方向の熱力に関して、モデルの詳細を述べた。その特徴は、1) 背景プラズマの速度分布関数に温度勾配を有する変形マクスウェル分布を用いたこと、さらに、2) この速度分布関数から背景粒子速度のランダムサンプリングを高速かつ正確に行う手法を提案したことにある。 第4章では、第3章のモデルをさらに拡張し、磁力線と垂直方向の温度勾配を有する変形マクスウェル分布を用いることにより、従来の運動論的シミュレーションでは全く考慮されていなかった磁力線垂直方向の熱力に関する数値シミュレーションモデルを新たに提案した。このモデルを用いてシミュレーションを行い、第2章の理論値と比較することにより、モデル妥当性を検証した。これにより、磁場垂直方向にテスト不純物粒子に働く熱力を、運動論的に計算することを初めて可能とした。また、熱力とローレンツ力により不純物粒子が磁場垂直方向に旋回中心ドリフトによって輸送されることを、運動論的数値シミュレーションにより初めて示すとともに、その効果が境界層プラズマ中の不純物輸送過程において無視できないことを示した。二体衝突法を用いた本モデルは、不純物による背景プラズマの自己無撞着な動的変化をも考慮する背景プラズマ不純物統合輸送計算にも容易に応用可能である。 第5章では、第3、4章の二体衝突モデルをもとに、フォッカープランク近似による熱力計算モデルを提案し、その妥当性を第4章の結果と比較・確認した。本近似はいわゆる微量不純物仮定の下で有効で、高精度かつ高速計算を可能にする。 第6章は結論であり、本研究で得られた成果をまとめた。				

SUMMARY OF Ph.D. DISSERTATION

School School of Fundamental Science and Technology	Student Identification Number	SURNAME, First name Yuki HOMMA
Title Numerical modeling of the thermal force for impurity transport in fusion plasmas		
Abstract <p>Correct understanding of impurity transport processes in fusion plasmas is one of the most important research subjects to realize stable energy production by nuclear fusion plasmas. Numerical simulations are widely used to investigate the impurity transport and its effects in fusion plasmas, such as the cooling of core plasma or the mitigation of plasma heat load onto device walls. In order to improve the impurity transport simulation, we have developed a new numerical model to simulate the thermal force acting on kinetic test-impurity particles. The thermal force is caused by Coulomb collisions with plasma ions if the background plasma has temperature gradient. The impurity transport across the magnetic field by thermal force has not been taken into account in the existing kinetic impurity transport simulation codes so far.</p> <p>Chapter 1 summarizes the motivation and the research subject.</p> <p>Chapter 2 describes the kinetic transport model of charged test particles in plasmas. Coulomb collisions are modeled as random walk process in the velocity space, and background plasma ions with temperature gradient are modeled by the distorted Maxwellian velocity distribution. Averaging all collisions between the test impurity particle and the plasma ions, the thermal force is analytically derived.</p> <p>Chapter 3 presents a new numerical model of the thermal force in unmagnetized background plasma, by using the Binary Collision model (BCM) to simulate Coulomb collisions. Efficient algorithm to randomly sample plasma ion velocities from the distorted Maxwellian has been newly developed. This model is equivalent and applicable to the simulation of thermal force along magnetic field line in magnetized plasmas.</p> <p>Chapter 4 extends the model to the case of magnetized background plasmas. By adopting more extended distorted Maxwellian, we have succeeded, for the first time, to kinetically simulate the thermal force due to temperature gradient perpendicular to the magnetic field. Such BCM-based model can be applied to more sophisticated impurity transport simulations including dynamic changes of background plasmas due to interaction with the impurities.</p> <p>On the basis of the study done in Chapter 3 and 4, another new thermal force model based on the Fokker-Planck (FP) collision approximation has been developed in Chapter 5. The FP approximation realizes more rapid calculation as far as the trace impurity limit holds. The validity of the model has been checked by comparison with the results obtained in Chapter 4.</p> <p>Chapter 6 summarizes the conclusion. Our new model has succeeded to simulate the thermal force due to the parallel and perpendicular temperature gradient. Numerical impurity transport simulation in fusion plasmas will be further improved by implementing our model.</p>		

Ph.D. Thesis

March 2014

Numerical modeling of the thermal force for
impurity transport in fusion plasmas

Yuki Homma

Adviser : Akiyoshi Hatayama

March 2014

Keio University
Graduate School of Science and Technology
School of Fundamental Science and Technology

Abstract

Correct understanding of impurity transport processes in fusion plasmas is one of the most important research subjects to realize stable energy production by nuclear fusion plasmas. Numerical simulations are widely used to investigate the impurity transport and its effects in fusion plasmas, such as the cooling of core plasma or the mitigation of plasma heat load onto device walls. In order to improve the impurity transport simulation, we have developed a new numerical model to simulate the thermal force acting on kinetic test-impurity particles. The thermal force is caused by Coulomb collisions with plasma ions if the background plasma has temperature gradient. The impurity transport across the magnetic field by thermal force has not been taken into account in the existing kinetic impurity transport simulation codes so far.

Chapter 1 summarizes the motivation and the research subject.

Chapter 2 describes the kinetic transport model of charged test particles in plasmas. Coulomb collisions are modeled as random walk process in the velocity space, and background plasma ions with temperature gradient are modeled by the distorted Maxwellian velocity distribution. Averaging all collisions between the test impurity particle and the plasma ions, the thermal force is analytically derived.

Chapter 3 presents a new numerical model of the thermal force in unmagnetized background plasma, by using the Binary Collision model (BCM) to simulate Coulomb collisions. Efficient algorithm to randomly sample plasma ion velocities from the distorted Maxwellian has been newly developed. This model is equivalent and applicable to the simulation of thermal force along magnetic field line in magnetized plasmas.

Chapter 4 extends the model to the case of magnetized background plasmas. By adopting more extended distorted Maxwellian, we have succeeded, for the first time, to kinetically simulate the thermal force due to temperature gradient perpendicular to the magnetic field. Such BCM-based model can be applied to more sophisticated impurity transport simulations including dynamic changes of background plasmas due to interaction with the impurities.

On the basis of the study done in Chapter 3 and 4, another new thermal force model based on the Fokker-Planck (FP) collision approximation has been developed in Chapter 5. The FP approximation realizes more rapid calculation as far as the trace impurity limit holds. The validity of the model has been checked by comparison with the results obtained in Chapter 4.

Chapter 6 summarizes the conclusion. Our new model has succeeded to simulate the thermal force due to the parallel and perpendicular temperature gradient. Numerical impurity transport simulation in fusion plasmas will be further improved by implementing our model.

Contents

1	Introduction	2
1.1	Energy resource problems and nuclear fusion	2
1.2	Tokamak device	5
1.3	Impurity particles in tokamak divertor configuration	9
1.3.1	Problems of impurities	9
1.3.2	Divertor configuration	9
1.3.3	Impurity transport in the edge plasma	13
1.3.4	Mechanism of thermal force due to parallel temperature gradient . . .	15
1.3.5	Mechanism of thermal force due to perpendicular temperature gradient	16
1.3.6	Impurity transport simulation and thermal force modeling	18
1.4	Purpose of Study	20
1.5	Thesis outline	20
2	Basic theory	22
2.1	Kinetic transport theory of charged test particle in plasmas	22
2.1.1	Test particle model	22
2.1.2	Force on a fixed test particle by Coulomb collisions with a uniform flux of background ions	23
2.1.3	Force on a moving test particle by Coulomb collisions with background ions	26
2.2	Velocity distribution function of background plasma ions	30
2.2.1	Collision operator $C_{b/b}$	32
2.2.2	Solution for the case of $\nabla T_b = \mathbf{0}$	32
2.2.3	Solution for the case of $\nabla T_b \neq \mathbf{0}$	32
2.3	Thermal force	35
2.3.1	Parallel thermal force $\mathbf{F}_{\parallel}^{\nabla T}$	36
2.3.2	Diamagnetic thermal force $\mathbf{F}_{\wedge}^{\nabla T}$ and perpendicular thermal force $\mathbf{F}_{\perp}^{\nabla T}$	39

3	Numerical model of thermal force based on Monte Carlo Binary Collision model in unmagnetized plasma	41
3.1	Distorted Maxwellian and thermal force in unmagnetized plasma	41
3.2	Numerical model of the thermal force based on BCM	43
3.3	Random velocity sampling from the distorted Maxwellian (Step 2)	45
3.3.1	Preparation: Two coordinate systems for the velocity space	45
3.3.2	Distorted Maxwellian expressed in System II	45
3.3.3	Sampling of random variable w	46
3.3.4	Sampling of random variable θ_{\parallel}	47
3.3.5	Sampling of random variable ϕ_{\parallel}	48
3.3.6	Background ion velocity, v_{\parallel}	48
3.4	Applicable Condition for the Model	48
3.5	Monte Carlo Binary Collision Model (Step 3)	50
3.6	Test simulations	52
3.6.1	Simulation parameters	52
3.6.2	Reference simulation with $\nabla T_b = 0$	53
3.6.3	Test simulations with finite test simulation ∇T_b	54
	Conditions	54
	Results of Case 1	56
	Results of Case 2	57
	Results of Case 3	58
	Results of Case 4	59
	Quantitative discussion on simulation results	59
3.7	Summary of Chapter 3	62
4	Extended numerical model of thermal force based on Monte Carlo Binary Collision model in magnetized plasma	63
4.1	Algorithm of the model	63
4.2	Random velocity sampling from distorted Maxwellian (Step 3)	65
4.2.1	Preparation	65
4.2.2	Distorted Maxwellian in System II	67
4.2.3	Random sampling of background ion velocity	68
4.3	Binary Collision Model (Step 4)	68
4.4	Buneman-Boris method (Step 5)	68
4.5	Applicability limits	69
4.6	Test simulations	71

4.6.1	Numerical parameters for test simulation I and II	71
	Magnetic field strength and number of test particles used in the test simulation I and II	73
4.6.2	Test simulation I – Diamagnetic thermal force –	73
	Results of Case (I-1) and (I-2)	75
	Result of Case (I-3)	75
4.6.3	Test simulation II – Temperature screening effect –	76
	Theoretical value of the temperature screening effect	77
	Example of a test particle trajectory	79
	Result of test simulation II	79
4.7	Summary of Chapter 4	82
5	Numerical kinetic model of thermal force based on Fokker-Planck collision op- erator	83
5.1	Model description	83
	5.1.1 Numerical implementation of the model	85
5.2	Test simulation	85
	5.2.1 Test simulation 1: evaluation of the thermal force	85
	5.2.2 Test simulation 2: effective length of collision time step Δt_{Coll}	85
5.3	Summary of Chapter 5	86
6	Conclusion	90
A	Coulomb logarithm	93
	A.1 Definition of Coulomb logarithm	93
	A.2 Justification for the value of Coulomb logarithm to be regarded as constant	94
B	Sampling of inclination angle θ_{\parallel} from density distribution $g(w', \theta_{\parallel})$	95
C	Examples of numerically sampled distorted Maxwellian distribution	96

Chapter 1

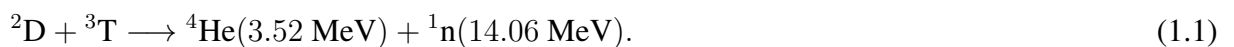
Introduction

1.1 Energy resource problems and nuclear fusion

Energy consumption in the human society is increasing year by year. To satisfy our energy demand, various energy resources are being developed. The nuclear fusion energy is considered as one of the most promising candidates for alternative energy resources of the future.

The *nuclear fusion reaction* (abbreviated *fusion*) is a reaction where lighter atomic nuclei fuse together to make a heavier nucleus. Depending on the reacting nuclei species, the mass defect occurs through the fusion. Such mass defect Δm can bring enormous energy gain ΔE according to the relativistic theory ($\Delta E = c^2 \Delta m$ with the speed of light c). For example, the fusion is the energy source of the stars.

To initiate the fusion process, positively charged nuclei have to come close enough to overcome their repulsive Coulomb barrier before the attractive nuclear forces combine the nuclei. The most feasible candidate for the controlled fusion is a reaction between the hydrogen isotopes, deuterium (D) and tritium (T), called *D-T reaction* (Fig. 1.1),



The energy production by the D-T reaction has the following advantages.

Energy gain: The released energy is about 1 million times larger than the chemical reactions, for example, compared with the H_2 combustion, $\text{H}_2 + (1/2)\text{O}_2 \longrightarrow \text{H}_2\text{O} + 2.96 \text{ eV}$.

Abundance: The deuterium and tritium are in ample supply [1]. The deuterium is obtained by hydrolysis of the sea water, in economically sustainable way. The tritium is produced by neutron bombardment on lithium, which is also available in abundance.

Safety: Unlike the nuclear fission of uranium, the D-T reaction does not have a chain reaction. Therefore, such fusion reactions can be easily stopped by simply cutting off the D-T fuel gas supply. In addition, the products by fusion are limited only to the helium and the neutron.

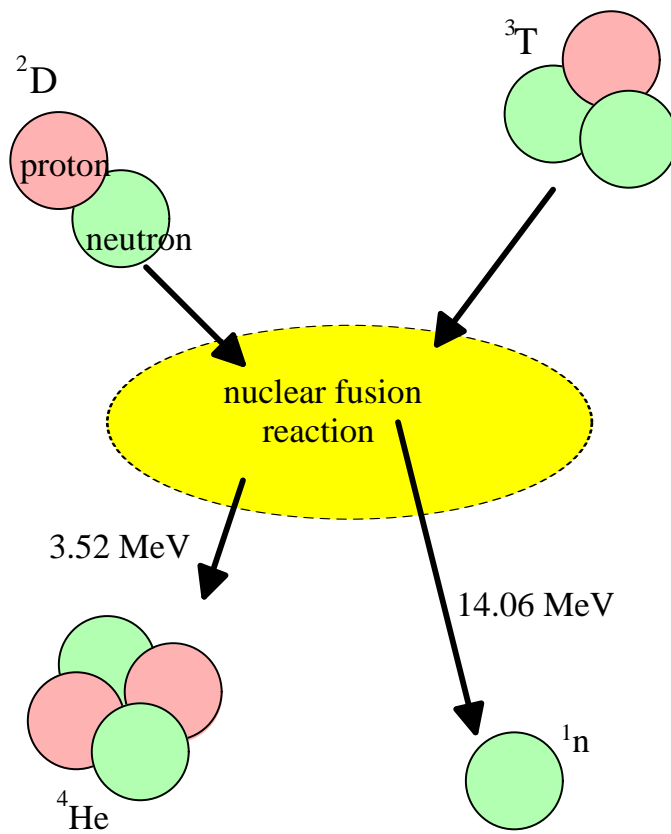


Figure 1.1: D-T fusion reaction.

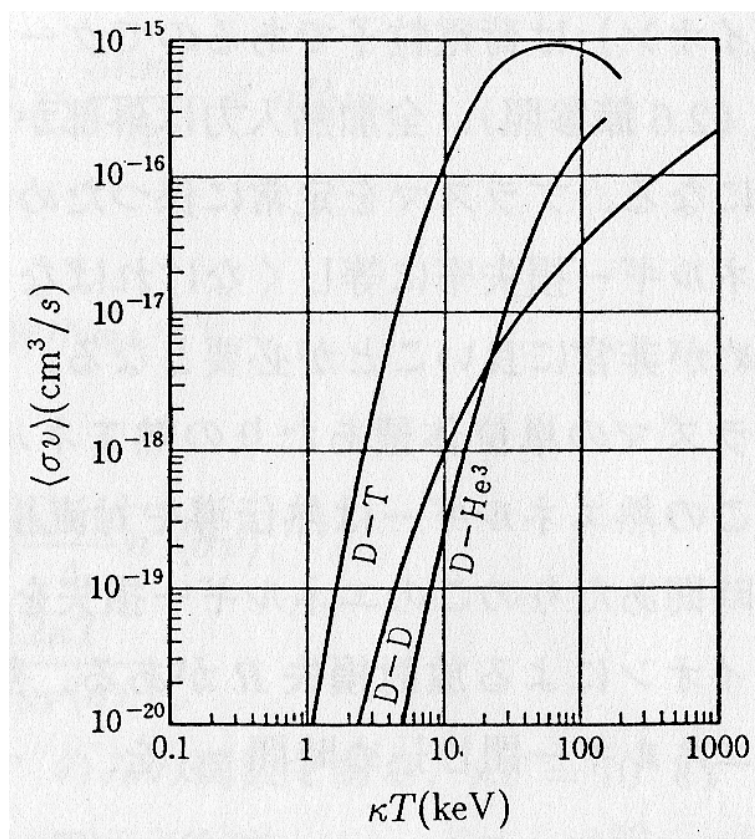


Figure 1.2: Rate coefficients of nuclear fusion reactions. (cited from Ref. [2].)

To start the D-T fusion reaction, a mixture of deuterium and tritium gas is heated up to the temperature of 10 to 20 keV, i.e. more than 100 million K, where the reaction rate of D-T reaction in Eq. (1.1) reaches its maximum (Fig. 1.2)¹. At such high temperature, all atoms are ionized. The heated D-T gas becomes an electrically neutral mixture of ions and electrons, defined as *plasma*. We keep such D-T plasma (otherwise *fuel plasma*) in a stable state, for the fusion reactions to occur continuously. A practical condition called *self-ignition criterion* [1],

$$n\tau_E T > 3.1 \times 10^{21} \text{ m}^{-3}\text{s keV}, \quad (1.2)$$

has to be satisfied in order for the fuel plasma to yield sufficient amount of energy to sustain the plasma itself. The left hand side of the inequality (1.2) is called the *fusion triple product* consisting of the number density² of plasma ions n (m^{-3}), the plasma temperature T (keV), and the energy confinement time of plasma³ τ_E .

¹It is useful in the plasma physics to express the temperature in the unit of Joule (J) or electron volt (eV), instead of Kelvin (K). The absolute temperature T_{abs} (K) is converted into the unit of Joule by $T_{\text{Joule}}(\text{J}) = k_B^{\text{Joule}} T_{\text{abs}}$, with the Boltzmann constants $k_B^{\text{Joule}} = 1.3804 \times 10^{-23} \text{ J/K}$. The temperature in electron volt is calculated from the relation $1 \text{ eV} = 1.6021 \times 10^{-19} \text{ J}$.

²Henceforth, the word *density* always means the number density.

³The energy confinement time τ_E is a characteristic time for a fusion plasma to lose its whole containing energy W

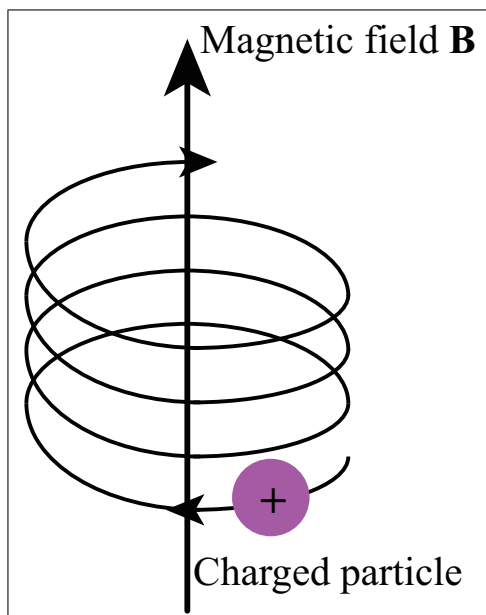


Figure 1.3: Larmor gyro-motion of charged particle around magnetic field line.

1.2 Tokamak device

To continue the fusion reactions, we have to hold the whole body of plasma separated away from the device walls; otherwise so many undesired impurity particles are sputtered out from the walls by plasma-wall interactions that fusion reactions stop immediately. The magnetic field makes it possible to confine the plasma separated from the wall. In the presence of magnetic field \mathbf{B} , charged particles can move freely along the field line, but they are restricted to move across (i.e. *perpendicularly to*) the \mathbf{B} -field. They have to follow a gyration motion (*Larmor gyration*) around the field line (Fig. 1.3), due to the Lorentz force $q(\mathbf{E} + \mathbf{v} \times \mathbf{B})$. If a magnetic field line is closed on itself, without any end edge, the plasma can be kept and confined as shown in Fig. 1.4. However, plasma confinement is not enough for such a simple torus \mathbf{B} -field because of particle drift motion. For better confinement of the fusion plasma, properly arranged magnetic field configurations have been conceived so far. One of the most promising and feasible concept is *tokamak* configuration. Fig. 1.5 presents a schematic structure of tokamak device. A circular sequence of toroidal field coils forms a doughnut-shaped confinement field, within which the fuel plasma is confined. The direction along which the toroidal coils are aligned is defined as *toroidal direction*. And the *poloidal direction* is defined around the toroidal direction. The tokamak device generates a torus-shaped closed magnetic field where the plasma is confined (Fig. 1.6). Such magnetic field \mathbf{B} is composed of the toroidal and poloidal component, $\mathbf{B} := \mathbf{B}_t + \mathbf{B}_p$. The \mathbf{B} -field line follows a helical trace, surrounding the torus surface (Fig. 1.7). The

without any heating. It is estimated by $\tau_E = W/P_{\text{loss}}$, where the rate of energy loss P_{loss} out of plasma is determined by the plasma transport, the interaction with device walls, and the synchrotron radiation etc.

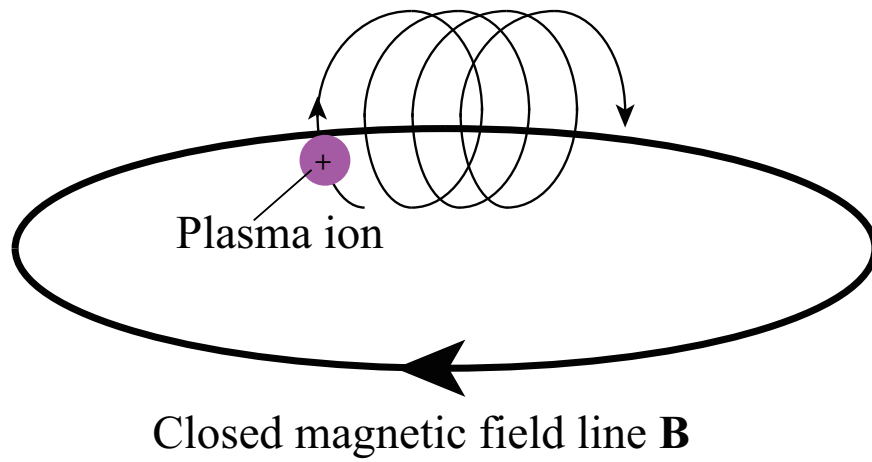


Figure 1.4: Principle of magnetic confinement.

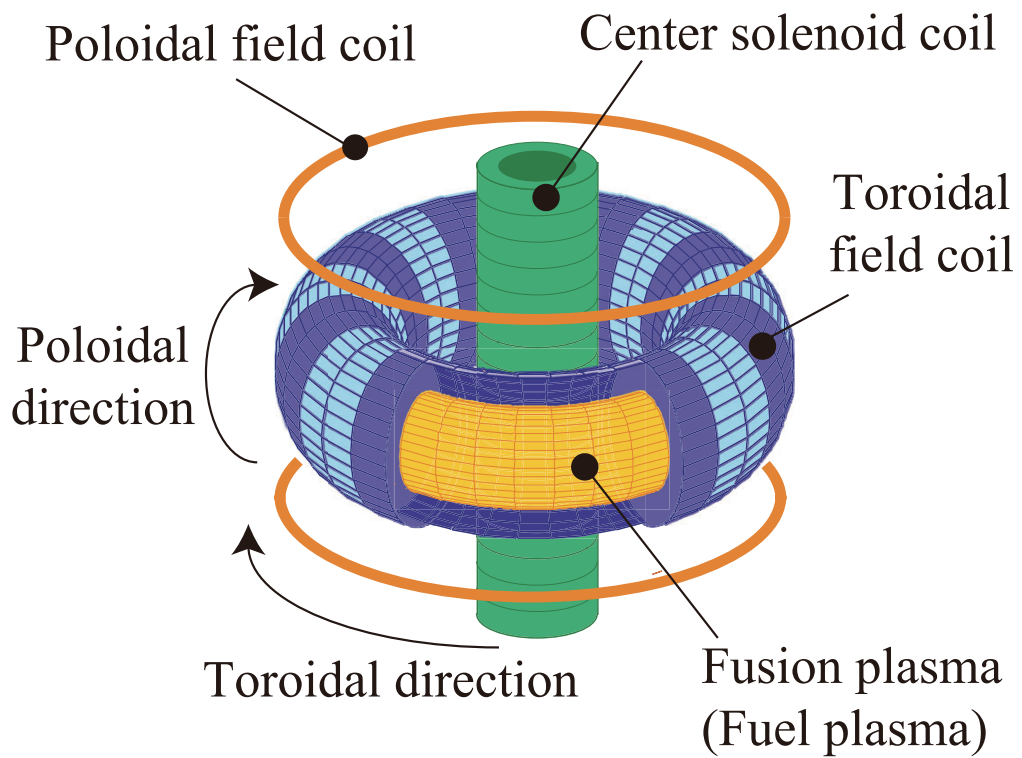


Figure 1.5: Tokamak plasma device.

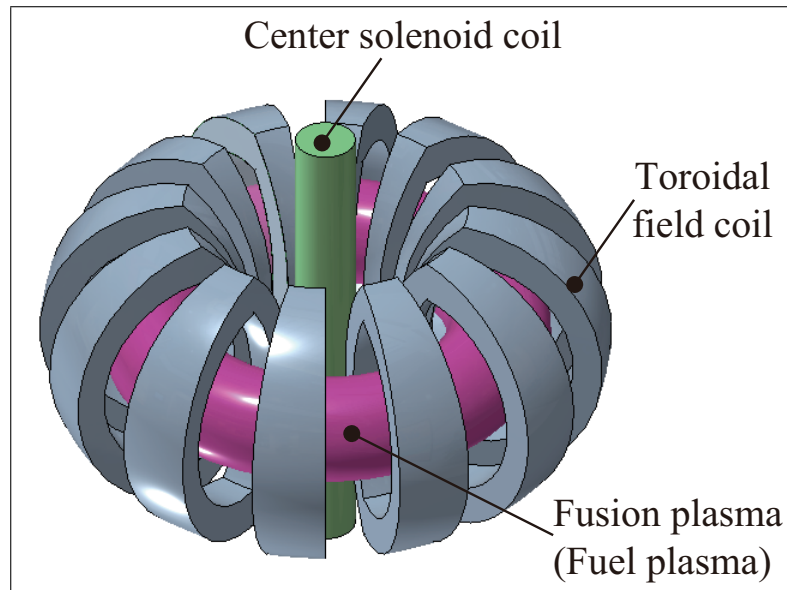


Figure 1.6: 3D shape of tokamak plasma.

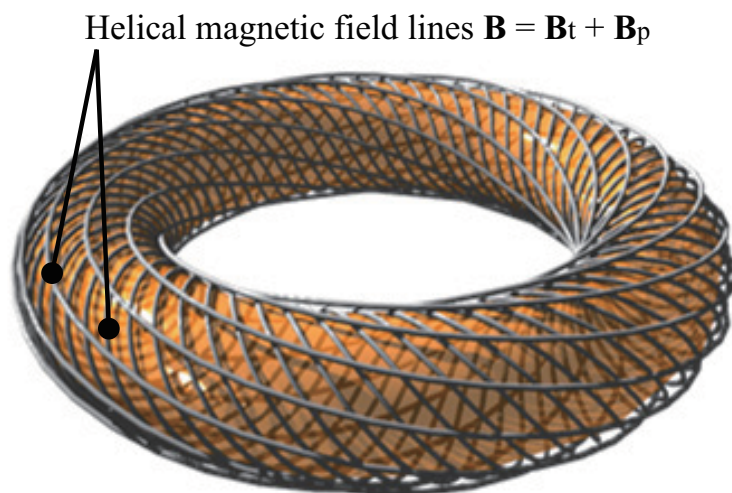


Figure 1.7: Tokamak magnetic field line in helically winding shape. (cited from Ref. [21].)

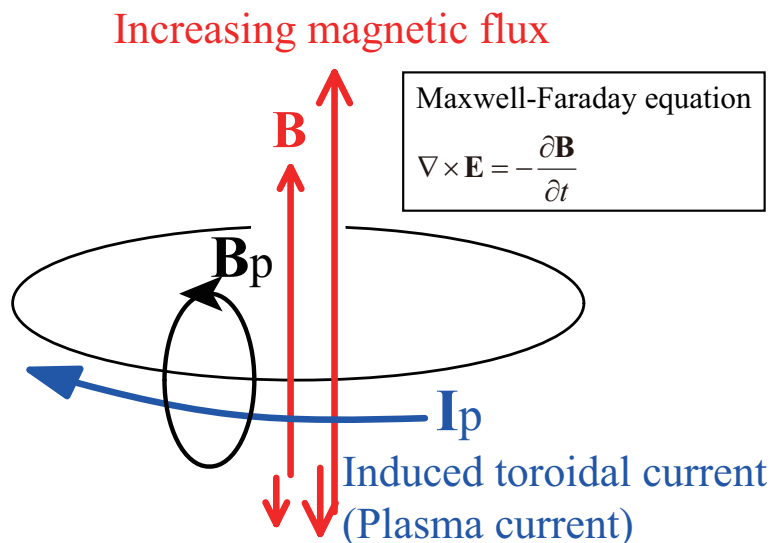


Figure 1.8: Induced plasma current by increasing the central magnetic flux.

toroidal component B_t is generated by the external toroidal coils shown in Fig. 1.5. The poloidal component B_p is generated by a toroidal current (also called *plasma current*). The toroidal current is, in turn, induced by increasing the magnetic flux within the central solenoid coil which is installed in the central part of the *doughnut* (Fig. 1.5). This induced current is simply understood by the Faraday's law of induction in Fig. 1.8. Such B_p -production, called *inductive current drive*, makes the steady-state operation of tokamak challenging. However, to resolve the problem, various methods of non-inductive current drive have been proposed and validated, e.g. RF(Radio Frequency) current drive or NBI(Neutral Beam Injection) current drive. Tokamak is still the closest to real energy production by the fusion.

To realize controlled fusion energy production, many tokamak experimental devices have been developed so far. Actual tokamak devices such as JT-60 U (Japan) [3, 4, 5], ASDEX Upgrade (Germany) [6] and JET (United Kingdom) [7, 8] can operate at a core plasma density $n \approx 10^{20} \text{ m}^{-3}$, a core temperature $T \approx 20 \text{ keV}$, and a confinement time $\tau_E \approx 0.1 - 1 \text{ s}$. Their achievements in energy production are measured with the energy gain factor,

$$Q = \frac{P_{\text{Fusion}}}{P_{\text{Heating}}} = \frac{\text{Fusion energy released by D-T reaction}}{\text{Plasma heating energy required}}. \quad (1.3)$$

The energy gain factor $Q = 1$ has already been achieved by the JT-60 U and JET tokamak. The international thermonuclear experimental reactor ITER [9, 10, 11] was designed and is now being constructed in France by international collaboration. The ITER is expected to operate at $Q \geq 10$ with an industrial-scale fusion power $P_{\text{Fusion}} = 500 \text{ MW}$ in 2019. Based on the physics and engineering achievements of ITER experiments, the first real fusion power plant DEMO [12] will be constructed in the near future, in order to supply electrical energy to our society.

1.3. IMPURITY PARTICLES IN TOKAMAK DIVERTOR CONFIGURATION

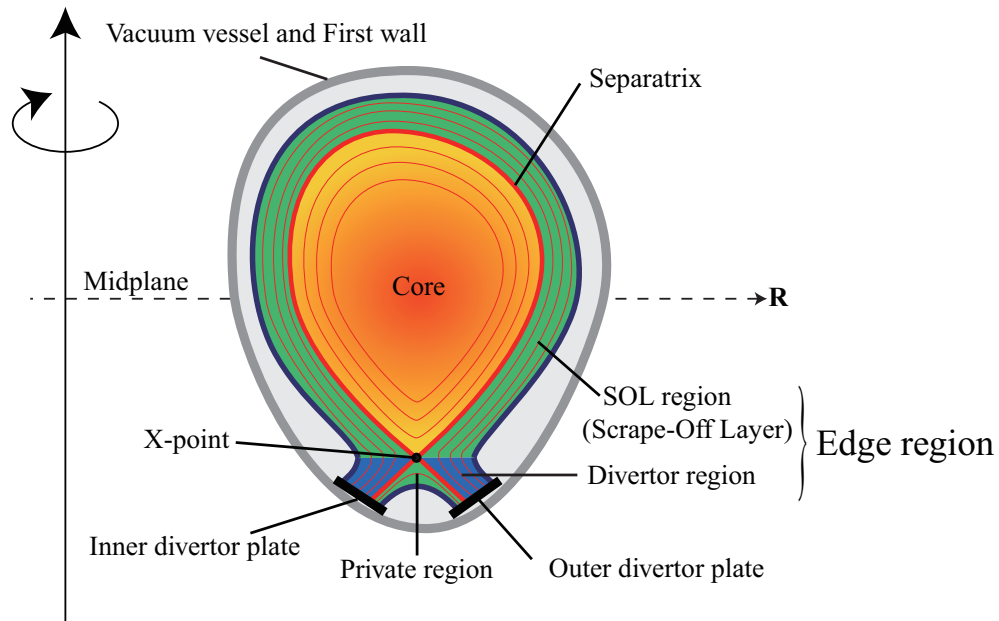


Figure 1.9: Poloidal cross section of the tokamak device.

1.3 Impurity particles in tokamak divertor configuration

1.3.1 Problems of impurities

This study focuses on the impurity transport problem in fusion plasmas, which is one of the most important research subjects to develop a sustainable tokamak device. In fact, tokamak confinement is not perfect. Due to the diffusion process and the plasma instabilities, plasma ions and electrons may gradually leak and escape from the closed magnetic field toward device's material walls. When escaping plasma ions collide to walls, various particles of wall component such as C, Fe, Be, W are sputtered out. If these impurity particles enter the core plasma, they would stop the fusion reactions by cooling the plasma temperature by strong radiation (Fig. 1.12). Controlling the impurities is indispensable for the fusion reactor to operate continuously.

1.3.2 Divertor configuration

It is possible to reduce the impurity yield from walls by weakening the plasma-wall interactions. For this purpose, a divertor magnetic field configuration has been conceived. Figure 1.9 shows the poloidal cross section of *divertor configuration*. It is realized, as shown in Fig. 1.10, by introducing a divertor coil inside which the electric current passes in the same direction as the plasma current. The most peripheral layer of the torus-shaped B -field is modified and no longer closed on itself (called *open field*). Due to the current in divertor coil, a point where the poloidal magnetic field B_P is null appears in the poloidal section (Fig. 1.10). This is called the *X-point*, and the magnetic flux surface

1.3. IMPURITY PARTICLES IN TOKAMAK DIVERTOR CONFIGURATION

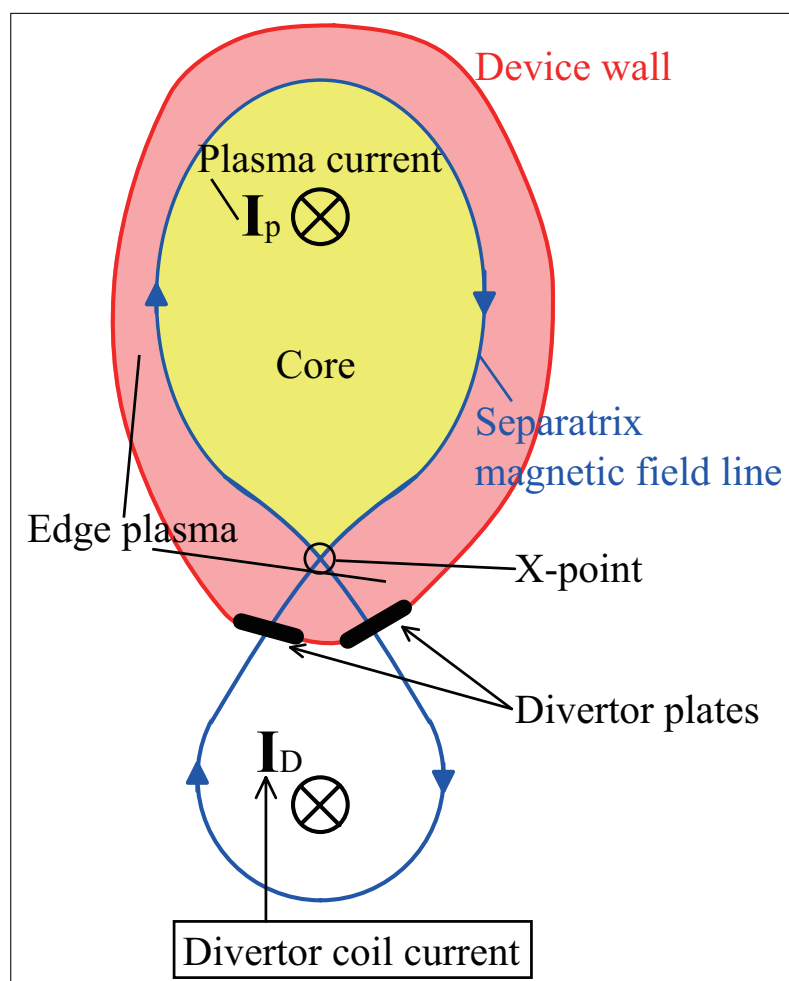


Figure 1.10: Divertor configuration.

1.3. IMPURITY PARTICLES IN TOKAMAK DIVERTOR CONFIGURATION

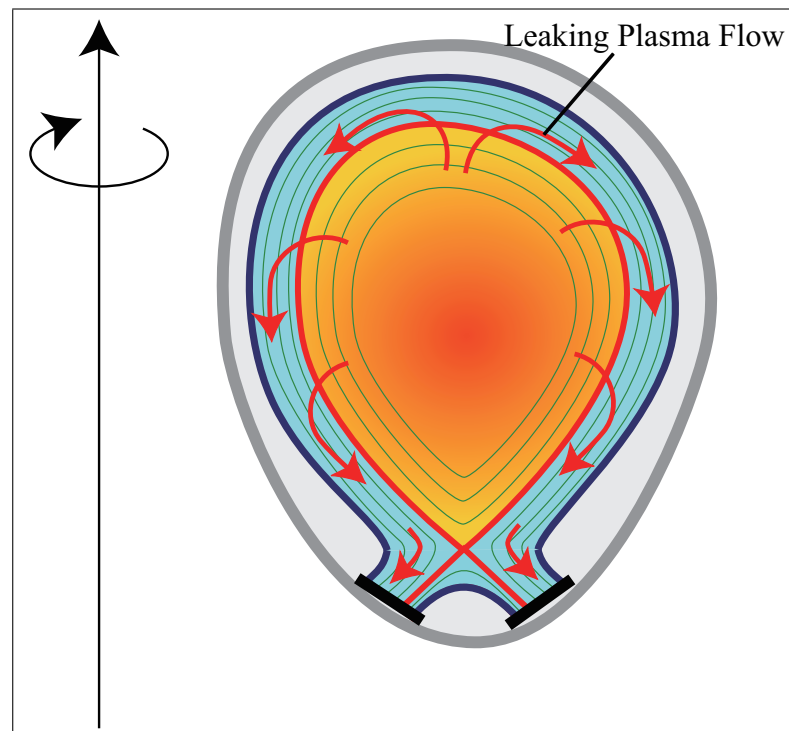


Figure 1.11: Plasma flow leaking from the core.

passing over the X-point is defined as *separatrix flux surface*. The volume inside the separatrix is the *core region* where the fusion plasma is retained steadily to promote the fusion. The peripheral region outside the separatrix is called *Scrape-Off Layer (SOL)*, where the magnetic field is open. At the end edges of the SOL, heat-resistant plates called *divertor plates* are installed. The SOL region below the X-point, just before the divertor plates, is especially called *divertor region*. The combined area of SOL and divertor region is called the *edge region*. Plasma ions and electrons leaking from the core are transported along the open **B**-field in the SOL, to run into the divertor plates, as shown in Fig. 1.11.

The divertor configuration has the following advantages:

- The plasma-wall contact area, from where impurities are generated, is limited to small divertor plates.
- The leaking plasma has some time to lose its energy by radiation and collisions with other particles during their passage through the SOL. The plasma arriving at the divertor region can be largely cooled down ($T \approx 10 \text{ keV} = 10000 \text{ eV}$ at the core, to $T \approx 10 \text{ eV}$ before divertor). Low plasma temperature weakens the plasma-wall interaction, and impurity generation is reduced.

Owing to such advantages, the divertor configuration has succeeded to reduce the impurity amount penetrating the core. The fusion performance has been largely improved.

On the other hand, from the divertor's point of view, treating and receiving such concentrated

1.3. IMPURITY PARTICLES IN TOKAMAK DIVERTOR CONFIGURATION

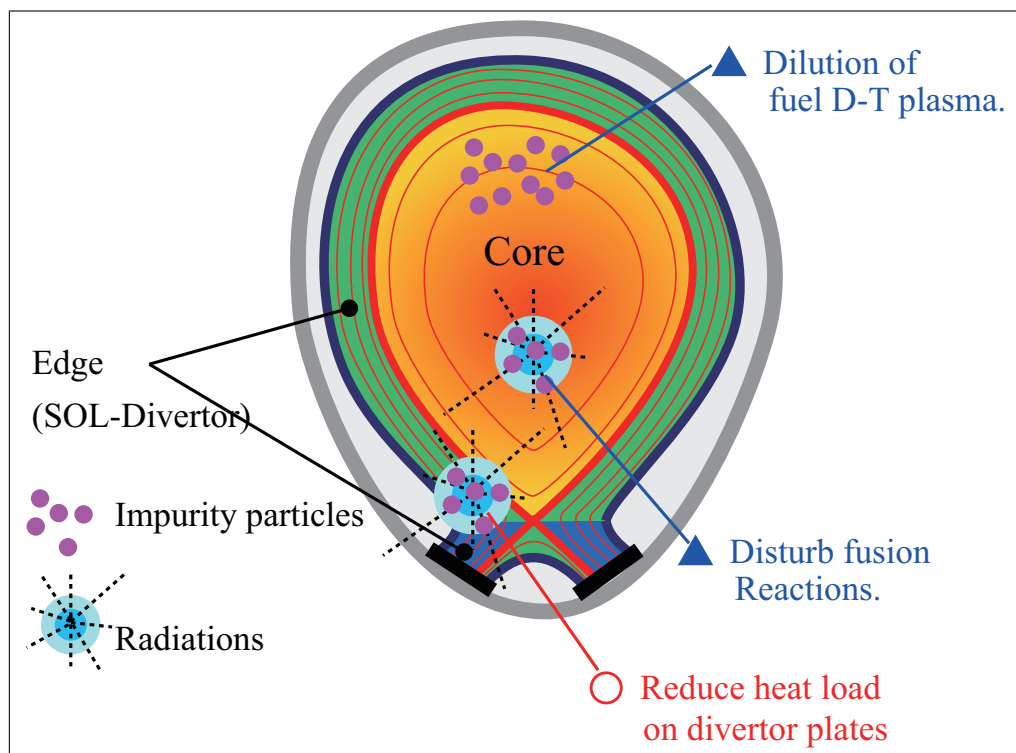


Figure 1.12: Effects of impurities on fusion plasma.

leaking plasma on the divertor plates is a challenging problem. The actual most advanced divertor materials (carbon, tungsten, etc...) can resist the incoming heat flux of up to 10 MW/m^2 . For ITER experiment, the heat load onto the divertor plates is expected to become much larger than 10 MW/m^2 unless we take any preventive measure.

An effective solution to reduce the divertor heat load is to reduce the energy of incoming plasma, i.e. its temperature and flow. Differently from the core case, the impurities here make useful and important contribution. They can dissipate the energy of leaking plasma during its passage through the edge region to divertor (Fig. 1.12). In preceding experiments, it has been succeeded to reduce the divertor heat load to a sustainable level, by artificially injecting some amount of impurities in the SOL region. Such plasma cooling by impurities is necessary for the divertor plates to endure throughout the plasma operation. Of course, increased amount of impurities for plasma cooling in the edge has a risk to degrade the core plasma performance. An appropriate balance between them has to be found.

The arguments above are the reasons why the impurity transport research is very important to develop fusion devices. In fusion plasmas, it is required to control the impurities, especially in the edge region, in order for them not to enter the core, but at the same time, do remain in the edge.

Effective technique to establish these conflicting requirements remains still to be developed. A lot of experimental and simulation research activities are being devoted for this purpose. The present thesis is one of such contributions.

1.3. IMPURITY PARTICLES IN TOKAMAK DIVERTOR CONFIGURATION

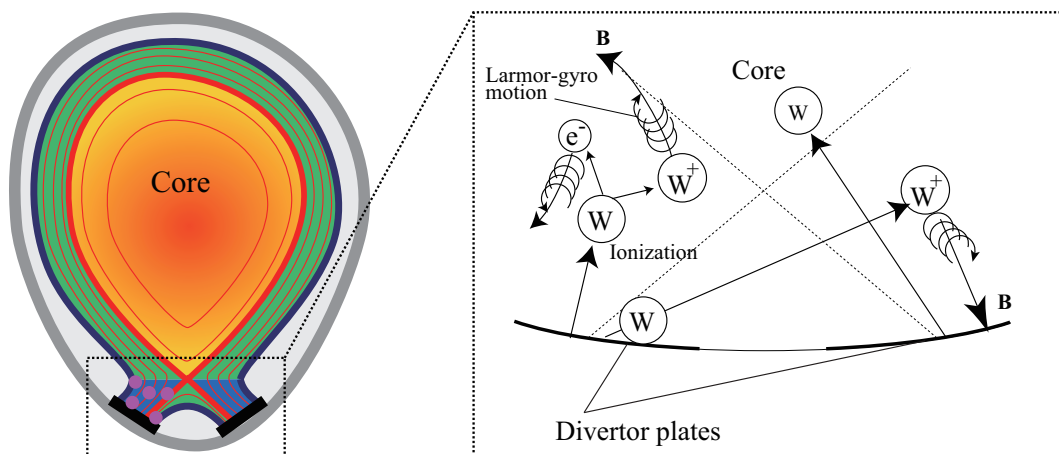


Figure 1.13: Picture of motion of the impurity particles just sputtered out of walls.

1.3.3 Impurity transport in the edge plasma

In order to control impurity behavior, we have to correctly understand the impurity transport processes in fusion plasmas, especially in the edge. When we focus on the impurity transport, the main fuel plasma is often referred to as *background plasma*.

The impurity particles (mass m , electric charge q) sputtered from the walls move in straight lines while they are neutral particles. Usually they are quickly ionized by hot background plasma (Fig. 1.13), to follow the magnetic field line \mathbf{B} with the Larmor gyro-motion. The motion of impurity is also influenced by the external electric field \mathbf{E} and the Coulomb collisions with background plasma ions and electrons (Fig. 1.14). These three factors, \mathbf{B} , \mathbf{E} , and Coulomb collisions, mainly determine the impurity transport.

The Lorentz force of electro-magnetic field $\mathbf{F}^{\text{Lorentz}} := q(\mathbf{E} + \mathbf{v} \times \mathbf{B})$ has two effects: the magnetic term makes the ions to follow the Larmor gyration around the \mathbf{B} -field line (Fig. 1.3), and the electric term drives the $\mathbf{E} \times \mathbf{B}$ drift of guiding center of impurity ions across the \mathbf{B} -field as shown in Fig. 1.15. These external forces are deterministic, therefore, easy to simulate.

The impurity ions receive the forces by Coulomb collisions with background plasma ions. Such *Coulomb collisional forces* consist mainly of the three kinds of force: (i) the *frictional force* [13], (ii) the *thermal force* [14] (or *temperature gradient force* [15]) and (iii) the *force due to the viscosity* [14].

The frictional force acts on impurity ions regardless of background temperature gradient. Its direction and magnitude are proportional to the relative velocity between the impurity ion velocity and the background plasma flow velocity. As shown in Fig. 1.11, since the background plasma flows from the core to the divertor plates, the frictional force usually transports the impurities toward the divertor region.

In the present study, the force due to the viscosity is assumed to be negligible, for simplicity. Effects by such plasma viscosity should be addressed in the future.

1.3. IMPURITY PARTICLES IN TOKAMAK DIVERTOR CONFIGURATION

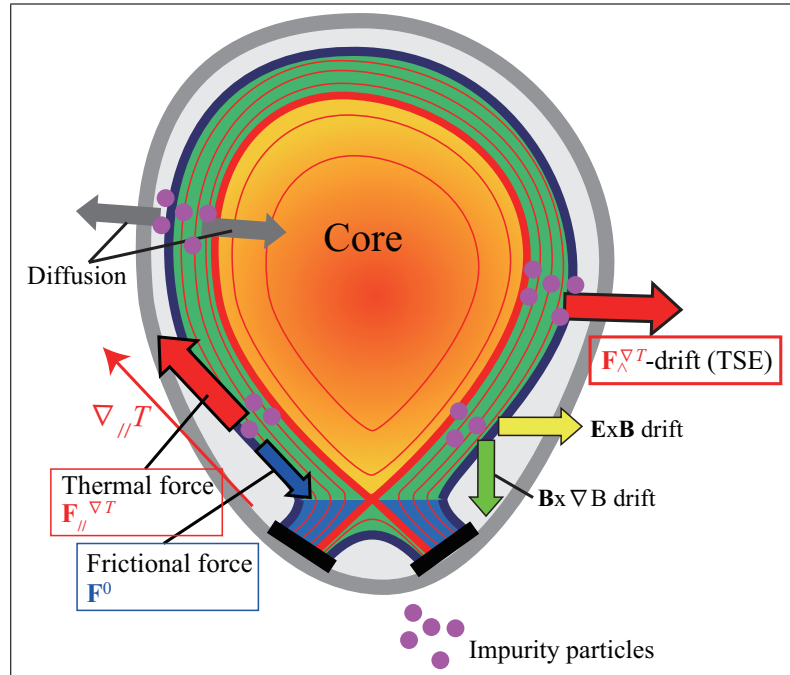


Figure 1.14: The impurity transport in plasmas is schematically presented. The balance between the frictional force F^0 and the parallel thermal force $F_{\parallel}^{\nabla T}$ determines the transport along magnetic field B . Across the magnetic field, impurities are transported by the diffusion, $E \times B$ -drift, $B \times \nabla B$ -drift, and the temperature screening effect (TSE) which is a drift by the diamagnetic thermal force $F_{\perp}^{\nabla T}$. These transport effects occur on the impurities simultaneously.

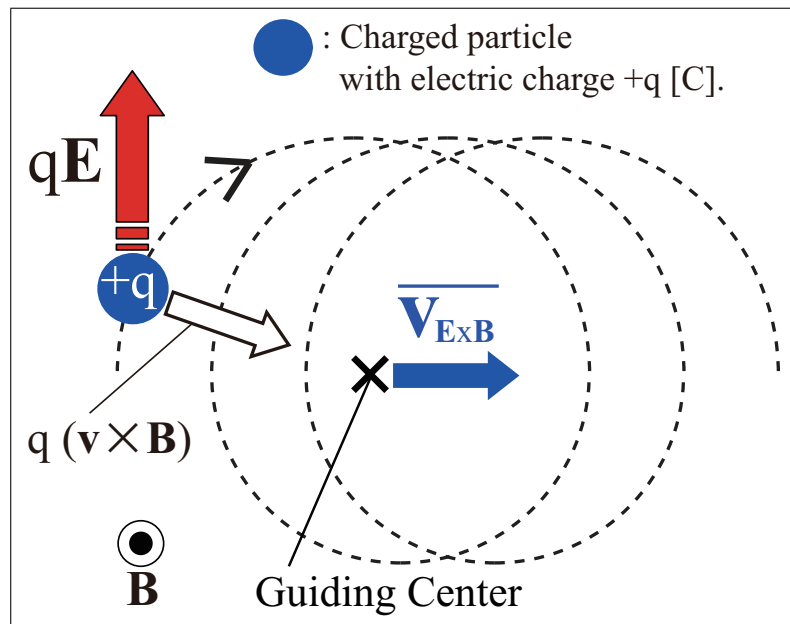


Figure 1.15: The $E \times B$ drift of guiding center of a charged particle across the magnetic field B .

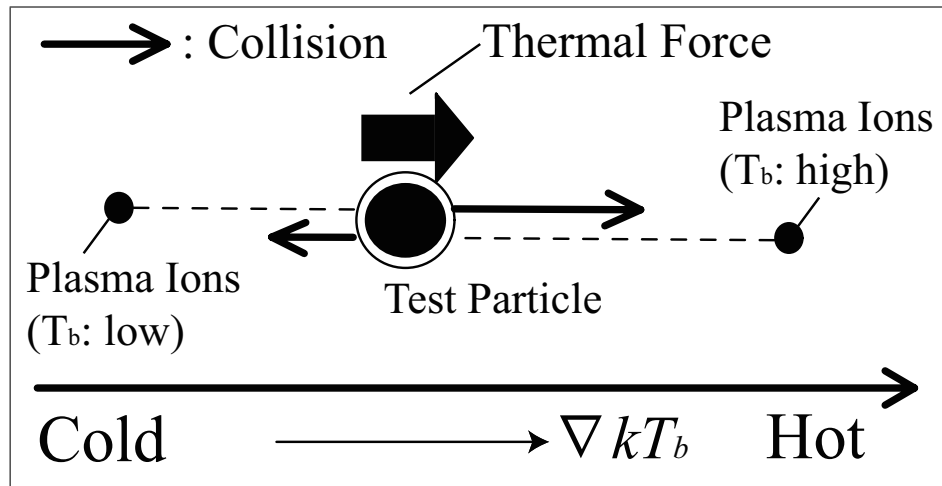


Figure 1.16: Mechanism of thermal force due to parallel temperature gradient. (cited from Ref. [50].)

The thermal force, which is the main subject of this study, is caused by the *background temperature gradient* ∇T_b [14], and has important effects on the impurity transport in plasmas.

1.3.4 Mechanism of thermal force due to parallel temperature gradient

The thermal force is caused by the fact that the Coulomb collision frequency ν_b is dependent on the background temperature T_b [14]. Suppose a test impurity particle is moving sufficiently slowly in a steady background plasma⁴. Background plasma ions are moving freely (along magnetic field if the plasma is magnetized) by thermal agitation. They come to the test particle by flying a distance of *mean free path* λ_{MFP} ⁵. When there exists a temperature gradient, the coming background ions have different energy, i.e. different temperatures, as shown in Fig. 1.16. The amount of momentum which is transferred to the test impurity by collisions, is roughly estimated by $m_b v_{th,b} \nu_b$. The Coulomb collision frequency ν_b is inversely proportional to the cubed relative velocity between the colliding two particles u (i.e. between the test impurity and a background plasma ion) as $\nu_b \propto u^{-3}$. The relative velocity u is approximated by the thermal speed of background plasma ion $v_{th,b} := \sqrt{T_b/m_b}$, with the mass of background ion m_b . Then, it is deduced that the momentum transfer to the test particle is inversely proportional to the background temperature at the location of the plasma ions,

$$m_b v_{th,b} \nu_b \propto v_{th,b}^{-2} \propto T_b^{-1}. \quad (1.5)$$

⁴When a test particle moves faster than the thermal speed of background plasma, the mechanism of thermal force is differently explained as in Sec. 2.3.1.

⁵The mean free path is an average distance traveled by a background ion during its two successive Coulomb collisions, estimated by

$$\lambda_{\text{MFP}} = \frac{v_{th,b}}{\nu_b}. \quad (1.4)$$

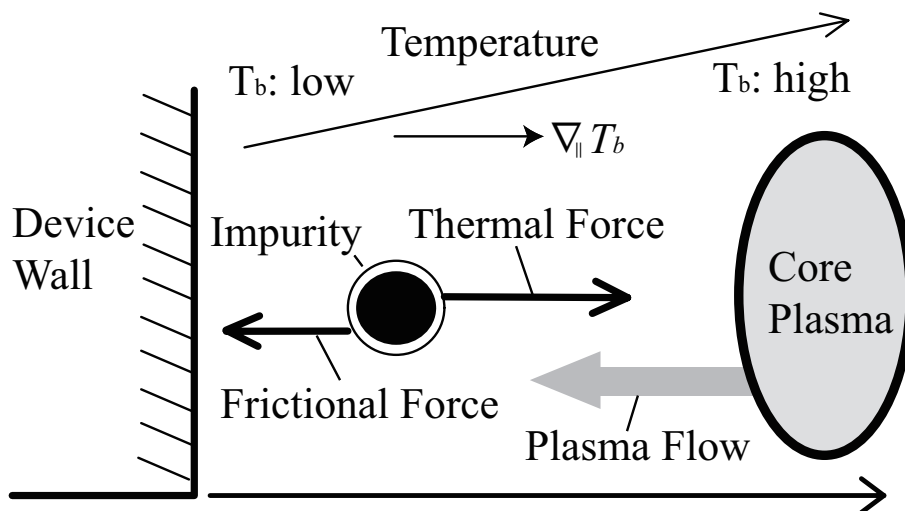


Figure 1.17: Temperature profile and force balance for an impurity in a fusion device. (cited from Ref. [50].)

From Fig. 1.16 and Eq. (1.5), the plasma ions coming from a lower T_b region exert stronger force on the test particle than the ions coming from a higher T_b region. Consequently, a net force acts on the test particle in the direction of temperature gradient, that is, toward the hotter region. This is the *parallel thermal force* due to *parallel* temperature gradient if the plasma is magnetized.

In the direction along the magnetic field, the particle transport (i.e. whether impurity ions go back to the divertor, or climb up the SOL and are getting closer to the core) is basically determined by the balance between the *parallel* thermal force and the frictional force [16, 17]. The parallel thermal force is due to the *parallel temperature gradient* $\nabla_{||} T_b$ along the \mathbf{B} -field line. Figure 1.17 shows a schematic of parallel transport, with a temperature profile typical in nuclear fusion devices. The frictional force due to background plasma flow from the core drives impurities toward the wall. On the contrary, the thermal force occurs along the temperature gradient, i.e. from the colder divertor region to the hotter core, pushing impurities up to the core. With steep temperature gradients in fusion plasmas, the magnitude of thermal force can be greater than that of the frictional force [16]. Then, impurities are driven toward the hot core by the thermal force. Such negative effect of thermal force has to be correctly estimated.

1.3.5 Mechanism of thermal force due to perpendicular temperature gradient

We summarize the mechanism of the thermal force on a test particle placed under perpendicular temperature gradient as shown in Fig. 1.18. The background plasma is magnetized by magnetic field \mathbf{B} along the Z -axis. The perpendicular temperature gradient $\nabla_{\perp} T_b$ is established along the X -

1.3. IMPURITY PARTICLES IN TOKAMAK DIVERTOR CONFIGURATION

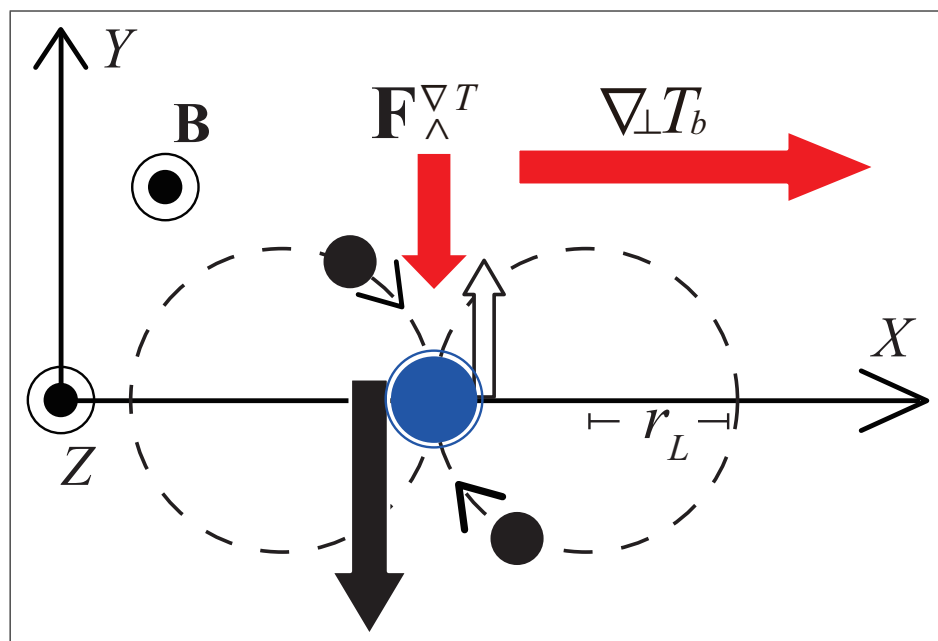


Figure 1.18: Thermal force perpendicular to the magnetic field \mathbf{B} . (cited from Ref. [30].)

axis. Background ions, gyrating in circles with Larmor radius r_L , come to the test particle from different T_b regions. They collide with the test particle from different directions. The average speed of the background ions is estimated by the thermal speed $v_{th,b}$ with the temperature at their center of gyration. For simplicity, the ion thermal speed $v_{th,b}$ is supposed to be faster than the speed of test particle. Since the amount of momentum transfer by collisions from a background ion to the test particle is estimated as $m_b v_{th,b} \nu_{Coll} \propto v_{th,b}^{-2} \propto T_b^{-1}$, the slower ions coming from the left side (colder side) in Fig. 1.18 push the test particle down more strongly than the faster ions from the right side push it up. Such unbalanced collisional momentum transfer leads to a net force on the test particle toward the $(-Y)$ -direction. This is the thermal force due to perpendicular temperature gradient. As it acts perpendicularly to both the magnetic field and the temperature gradient, we call it the *diamagnetic thermal force* in this study.

In the *perpendicular direction* to the \mathbf{B} -field (also referred to as *radial direction*), a steep temperature gradient is established within the SOL. It is because that the background plasma leaked from the core into the SOL escape very fast along the open \mathbf{B} -field, much more quickly than the time scale for the plasma to move across the \mathbf{B} -field by diffusion. The *perpendicular temperature gradient* $\nabla_{\perp} T_b$ is much steeper than the parallel gradient (e.g. Their typical values in the SOL are $\nabla_{\perp} T_b \approx 100 - 1000$ eV/m while $\nabla_{\parallel} T_b \approx 1 - 10$ eV/m). Perpendicular motion of impurities across the \mathbf{B} -field is brought about by the diffusion due to Coulomb collisions and by the guiding center drift. In addition to the well-known $\mathbf{E} \times \mathbf{B}$ drift [18] and curvature $\mathbf{B} \times \nabla B$ drift [18], the diamagnetic thermal force drives another drift which transports the impurity ions across the \mathbf{B} -field toward $(-\nabla_{\perp} T_b)$ -direction, i.e. perpendicularly from hot to cold plasma region. It is a macroscopic transport effect of thermal force

called *temperature screening effect (TSE)* [19]. Since the TSE is expected to eject impurities from the hot core and prevent them to penetrate the core, the diamagnetic thermal force has to be correctly estimated. However it has not been taken into account in any previous impurity transport simulations.

1.3.6 Impurity transport simulation and thermal force modeling

Numerical simulation is a very useful tool for impurity transport study. In the experiments one can observe the final density profile of impurities after plasma operations, but their transient trajectories followed, their generation from wall sputtering, and their complicated chemical/atomic reaction processes during operations, are very difficult to be observed directly. The numerical simulation is able to see such processes. The accuracy of simulation is determined by the correct modeling of intervening physics phenomena. This thesis is about to develop more reliable modeling of the thermal force on impurity.

In the preceding works, two types of impurity transport models have been developed: *fluid model* and *test particle model* (also called *kinetic model*). The fluid model treats the impurities as a fluid element, while the test particle model solves the motion of individual impurity test particles. The test particle model has the following advantages [16, 17, 20] compared with the fluid model:

1. The model directly follows the trajectories of each impurity test particles.
2. Various collisional effects on impurities, such as the ionization / recombination process and Coulomb collisions with background particles can be precisely simulated.
3. The interaction between impurities and wall materials (such as the self-sputtering) can be correctly simulated.
4. The model can be applied for background plasmas of any collisionality, while the fluid model is applicable only under high collisionality.

These days, the test particle modeling has been more and more adopted for impurity transport simulation in fusion plasma because of its superior accuracy brought by the above advantages. In addition, improvements in numerical efficiency by more sophisticated algorithms and by more powerful computer resources are promoting the use of test particle modeling.

In the test particle modeling of impurity transport processes, the following physics have already been included:

- Lorentz force (Larmor gyro-motion)
- Coulomb collisions for stochastic diffusion
- $\mathbf{E} \times \mathbf{B}$ drift and $\mathbf{B} \times \nabla B$ drift
- Anomalous diffusion, which is due to perturbation of \mathbf{B} and \mathbf{E} -field in background plasma.

1.3. IMPURITY PARTICLES IN TOKAMAK DIVERTOR CONFIGURATION

- Chemical and atomic reactions such as the ionization, the recombination, the charge exchange and so on.

A lot of numerical codes based on the test particle model have been extensively developed in world wide so far, e.g. DIVIMP [22], IMPMC [23], BBQ [24], MCI [25], DORIS [17]. In addition to these codes, the IMPGYRO code [26, 27] has recently been developed for the transport analysis of high- Z impurities such as tungsten.

However, the modelings above are not complete yet. The thermal force has not been included or correctly modeled, although it can have important effects on impurity transport [29, 30, 19, 17].

In the existing test-impurity transport codes listed above, the thermal force is simulated by the following two modelings. One is the fluid-type model [14, 28, 15, 16] and the other is the kinetic-type model [17, 29].

In the fluid-type model [28], the thermal forces due to parallel temperature gradient of background electrons $\nabla_{\parallel} T_e$ and ions $\nabla_{\parallel} T_b$ are given by

$$\mathbf{F}_{\parallel}^{\nabla T} = \alpha_Z \nabla_{\parallel} T_e + \beta_Z \nabla_{\parallel} T_b, \quad (1.6)$$

$$\alpha_Z := 0.71 Z^2, \quad (1.7)$$

$$\beta_Z := -3 \times \frac{1 - \mu - 5\sqrt{2} Z^2 (1.1\mu^{5/2} - 0.35\mu^{3/2})}{2.6 - 2\mu + 5.4\mu^2}, \quad (1.8)$$

$$\mu := \frac{m_Z}{m + m_Z}, \quad (1.9)$$

with the electron temperature T_e , the background ion temperature T_b and its mass m_b , and the impurity particle mass m_Z and its charge state Z . For each collision event between an impurity test particle and a background plasma ion, the above value of thermal force is added on each impurity particle. As seen from Eq. (1.6), the information about the velocities of colliding impurity and background ion are discarded. In addition, only the parallel temperature gradient is considered in the actual simulation codes.

In the kinetic-type model, the formula of *kinetic* thermal force in Eq. (2.59) is made use of. The kinetic thermal force can take into account both the velocities of colliding impurity and background ion. The kinetic-type model is more correct than the fluid-type model. As discussed in Sec. 2.3.1, the reversed thermal force can be simulated only by the kinetic-type model.

The fluid model is useful and valid if the background thermal speed is much faster than the test impurity ion speed. This assumption is fulfilled for the case between the test impurity ions and the background plasma electrons because of their large mass difference. The thermal force due to the electrons gradient ∇T_e can be simulated by the fluid-type modeling.

However, as pointed out in Ref. [17], the fluid-type model gives incorrect results between impurity ions and background ions because they have the same order of mass. Impurities can move as fast as

1.4. PURPOSE OF STUDY

or even faster than background ions. More careful *kinetic* modeling is required for the thermal force by the background ions gradient ∇T_i .

Some numerical modelings of the kinetic thermal force have been developed so far. For example, the DORIS code [17] and the IMPMC code [29] are equipped with the most advanced kinetic model of thermal force. They can simulate the kinetic thermal force along the magnetic field line by using the Fokker-Planck collision method, taking into account the parameters such as individual test particle velocity, the parallel temperature gradient $\nabla_{\parallel} T_b$, and the background plasma density and its flow velocity.

However, in all existing kinetic impurity transport simulation codes, steep perpendicular temperature gradient $\nabla_{\perp} T_b$ in the edge and its thermal force have still been neglected, even though they may have non-negligible effects on impurity transport [30].

1.4 Purpose of Study

The purpose of this thesis study is to develop a numerical model of the thermal force for the kinetic test particle transport simulation in fusion plasmas. Our model aims to correctly simulate the thermal force on individual test particle, caused by parallel ($\nabla_{\parallel} T$) and perpendicular background temperature gradient ($\nabla_{\perp} T$). Since the thermal force is a part of Coulomb collisional force, correct modeling of velocity distribution of background plasma ions and correct simulation of Coulomb collisions play key roles in our model.

To model background plasma ions with temperature gradient, we try to use a *distorted Maxwellian distribution function*. And two types of Monte Carlo methods are exploited for Coulomb collision, i.e. the *Binary Collision Model (BCM)* and the *Fokker-Planck (FP) collision method*. All the actual kinetic impurity transport simulation codes use one of these two methods. Since both the BCM and FP method are made available, our new numerical model of thermal force can be very widely applied, to realize more reliable impurity transport simulations which will surely contribute to the development of fusion energy.

1.5 Thesis outline

The thesis is organized as follows.

In Chapter 1, brief introduction to the development of nuclear fusion energy, the background and the purpose of study are presented. For stable energy production by the fusion, there are still many challenging tasks to overcome. This study aims to solve one of them: modeling of thermal force for reliable impurity transport simulation in fusion plasmas.

1.5. THESIS OUTLINE

In Chapter 2, the basic theories are explained. Combining the kinetic transport theory of charged test particle, with the background plasma ions in distorted Maxwellian velocity distribution, leads to the analytical formula of thermal force.

In Chapter 3, as a first step toward our goal, a numerical model of thermal force in an unmagnetized plasma is presented. It is in fact equivalent to the simulation of parallel thermal force in magnetized plasma. Coulomb collisions between test particles and background plasma ions are simulated by the Binary Collision Model (BCM).

In Chapter 4, we extend the model to the case of magnetized background plasma. A perpendicular temperature gradient is introduced. The diamagnetic thermal force caused by perpendicular temperature gradient is intensively investigated. Coulomb collisions are also simulated by the BCM as in Chapter 3.

In Chapter 5, another thermal force model in magnetized plasma based on the Fokker-Planck (FP) collision approximation is presented.

Chapter 6 summarizes the thesis.

Chapter 2

Basic theory

The basic theories of this study are explained in this chapter. At first, a kinetic transport theory, called Test Particle model, gives a general expression to estimate the Coulomb collisional force acting on a test charged particle in plasma. Next, we will show that the behavior of background plasma ions under the existence of temperature gradients is characterized by the distorted Maxwellian velocity distribution. Combining these theoretical considerations, we will find the analytical formula of the thermal force on test impurity particles.

2.1 Kinetic transport theory of charged test particle in plasmas

The motion of impurity ions in fusion plasmas is determined by the externally applied electromagnetic field (\mathbf{E} and \mathbf{B}) and by Coulomb interaction with background plasma ions (*Coulomb collision*). The simulation and estimation of Coulomb collisional force should be handled more carefully than the external electro-magnetic forces, because the Coulomb collision scatters randomly the velocity of impurities. The theoretical estimation of Coulomb collisional force is presented in this section, by following the considerations given by Trubnikov [13].

2.1.1 Test particle model

To model an impurity ion in background fusion plasmas, we consider a test charged particle. We will estimate the force on such a test particle due to Coulomb collisions with background plasma ions. We start at a simple case where the test particle is fixed in the space. Then, the realistic condition with freely moving test particle and with arbitrary velocity distribution of background ions will be considered, to find a general expression of the collisional force on test particles.

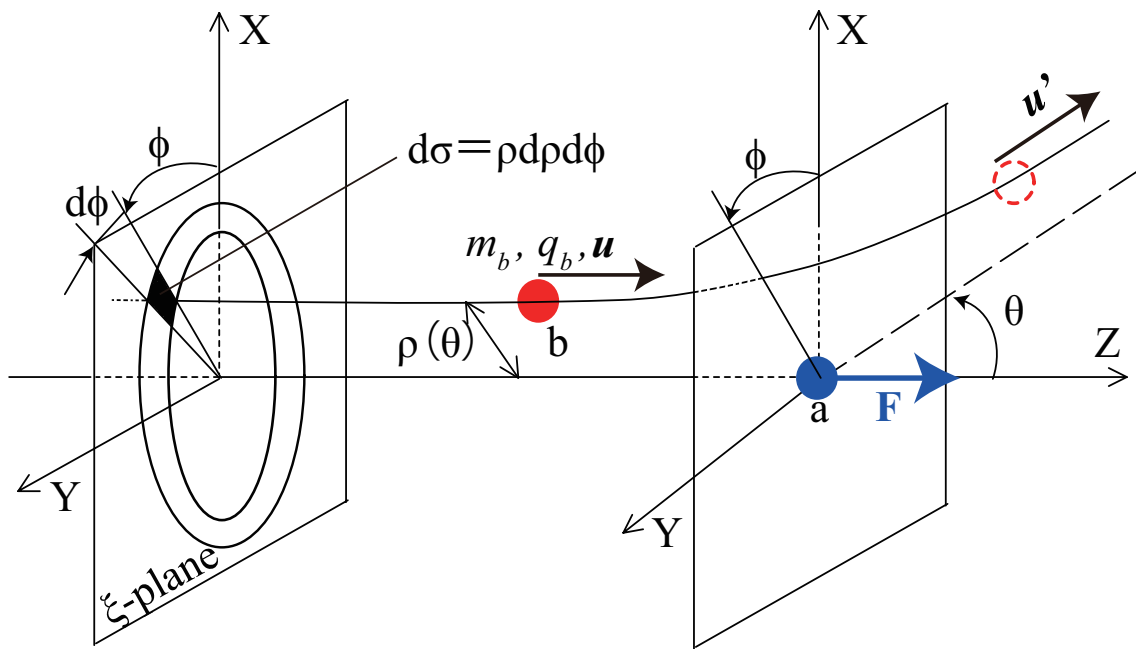


Figure 2.1: Test Particle Model.

2.1.2 Force on a fixed test particle by Coulomb collisions with a uniform flux of background ions

Figure 2.1 shows an event of Coulomb collision schematically. As a first step, we consider a test charged particle (species: a , mass: m_a , electric charge: q_a) fixed at a point in the space (it is equivalent to take the limit of $m_a \rightarrow \infty$). The uniform incident flux of background plasma ions (species: b , mass: m_b , electric charge: q_b , number density: n_b) are supposed to come from the infinity, to collide with the test particle of species a . The incident flux of ions of species b is distributed uniformly in the space with the number density n_b , and all ions of species b have the identical initial velocity \mathbf{u} . Through many Coulomb collisions with such background ions of species b , the test particle of species a experiences the collisional force $\mathbf{F}^{a,\text{fixed}}$.

We will introduce the following definitions as shown in Fig. 2.1. The direction of the incident flux velocity \mathbf{u} is defined as the Z -axis. The X - and Y -axis are taken perpendicular to the Z -axis, and the X - Y plane is named as ξ -plane. The rotation angle ϕ around the Z -axis is measured from the X -axis. The distance of the incident particle of species b from the Z -axis is named the *impact parameter* ρ .

Let one Coulomb collision occur between the fixed test particle of species a and one incident background ion of species b with the impact parameter ρ . The collision is supposed to be elastic. As a result of collision, the velocity \mathbf{u} of the ion of species b is scattered to \mathbf{u}' . The collision is characterized by the scattering angle θ , which is defined as the angle between the vectors \mathbf{u} and \mathbf{u}' . The rotation angle ϕ does not change throughout the collision.

To determine the force $\mathbf{F}_a^{a,\text{fixed}}$ exerted on the fixed test particle, we start at estimating the momen-

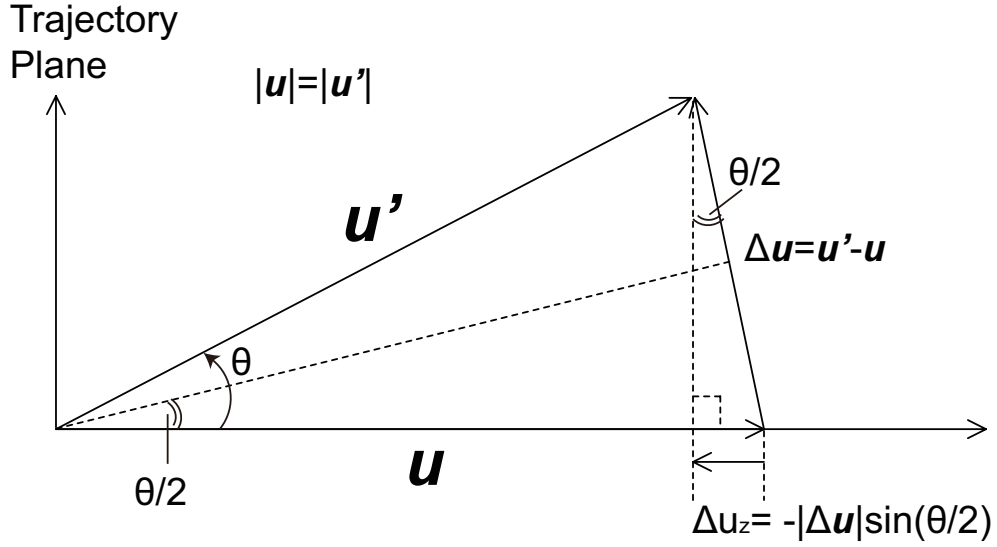


Figure 2.2: Velocity change of incident particle by Coulomb collision with a fixed particle.

tum change in one collision $\Delta \mathbf{p}_b^{\text{one coll.}}$ felt by a single incident ion of species b . Let's find the velocity change in one collision $\Delta \mathbf{u}^{\text{one coll.}}$ of the colliding ion of species b . The motion of the ion of species b follows the equation

$$\dot{\mathbf{p}}_b (= m_b \dot{\mathbf{u}}) := \frac{d\mathbf{p}_b}{dt} = \frac{q_b q_a}{4\pi\epsilon_0} \cdot \frac{(\mathbf{r}_b - \mathbf{r}_a)}{|\mathbf{r}_b - \mathbf{r}_a|^3}, \quad (2.1)$$

where the positions of the fixed particle of species a and the incident ion of species b are indicated, respectively, by \mathbf{r}_a and \mathbf{r}_b . The overdot denotes a time derivative. To focus on the Coulomb collision process, only the term of Coulomb interaction is retained in the right hand side of Eq. (2.1), i.e., the Lorentz force $q_b(\mathbf{E} + \mathbf{u} \times \mathbf{B})$ has been omitted. In this study, all the physical quantities are measured in the international system of units (SI). The velocity change $\Delta \mathbf{u}^{\text{one coll.}}$ can be obtained by integrating Eq. (2.1) during the Coulomb interaction time $\Delta t^{\text{one coll.}}$. By taking the limit of infinite mass ($m_a \rightarrow \infty$) and the assumption that the Coulomb collision be elastic, only the direction of \mathbf{u} is changed by the collision. As shown in Fig. 2.2, the relation between the incident velocity \mathbf{u} and the scattered velocity \mathbf{u}' can be simply deduced. The velocity change of the ion of species b projected on the Z -direction is

$$\Delta u_z^{\text{one coll.}} = -2u \sin^2 \frac{\theta}{2}. \quad (2.2)$$

The expression Eq. (2.2) is valid for any kind of elastic collision. To consider the case of Coulomb collision, we need to exploit the relation between the impact parameter ρ and the scattering angle θ , which is particular to Coulomb collision, such as [13]

$$\tan \frac{\theta}{2} = \frac{q_a q_b}{4\pi\epsilon_0 m_b u^2 \rho} = \frac{\rho_{\perp}}{\rho}, \quad \text{with} \quad (2.3)$$

$$\rho_{\perp} := \frac{q_a q_b}{4\pi\epsilon_0 m_b u^2}, \quad (2.4)$$

2.1. KINETIC TRANSPORT THEORY OF CHARGED TEST PARTICLE IN PLASMAS

where ϵ_0 is the vacuum permittivity. It is obtained by integrating the Coulomb interaction¹ between the particles, during the collision. Now, the velocity change $\Delta u_Z^{\text{one coll.}}$ of an incident ion of species b is related to its initial velocity and the impact parameter

$$\Delta u_Z^{\text{one coll.}} = -2u \sin^2 \frac{\theta}{2} = -2u \frac{\rho_\perp^2}{\rho_\perp^2 + \rho^2}. \quad (2.5)$$

We integrate Eq. (2.5) to find out the total momentum change $\Delta \mathbf{p}_b^{\text{TOTAL}}$ experienced by the flux of ions of species b per unit time. The number of ions of species b passing through an elementary area $d\sigma = \rho d\rho d\phi$ in the ξ -plane (in Fig. 2.1) per unit time is $n_b u d\sigma$. Every one of the ions of species b passing through a specific area $d\sigma$ is scattered by the same angle θ , and undergoes the momentum change $\Delta \mathbf{p}_b^{\text{one coll.}} = m_b \Delta \mathbf{u}^{\text{one coll.}}$. Their rotation angle ϕ is not affected. By using Eq. (2.5), the time rate of change of the total momentum $\Delta \mathbf{p}_b^{\text{TOTAL}}$ felt by the ions of species b is obtained by integrating $\Delta \mathbf{p}_b^{\text{one coll.}}$ over the entire ξ -plane,

$$\frac{\Delta \mathbf{p}_b^{\text{TOTAL}}}{1\text{s}} = \sum_b \frac{\Delta \mathbf{p}_b^{\text{one coll.}}}{1\text{s}} = \frac{\int_{\xi\text{-plane}} m_b \Delta \mathbf{u}^{\text{one coll.}} (n_b u d\sigma)}{1\text{s}}. \quad (2.6)$$

Since the uniform flux of ions of species b is scattered symmetrically around the Z -axis, only the Z -component of momentum change remains after the integration:

$$\begin{aligned} \int_{\xi\text{-plane}} m_b \Delta \mathbf{u}^{\text{one coll.}} n_b u d\sigma &= \int_{\xi\text{-plane}} m_b \Delta u_Z^{\text{one coll.}} n_b u d\sigma \left(\frac{\mathbf{u}}{u} \right) \\ &= - (4\pi m_b n_b u^2 \rho_\perp^2) \int_0^\infty \frac{\rho}{\rho^2 + \rho_\perp^2} d\rho \left(\frac{\mathbf{u}}{u} \right). \end{aligned} \quad (2.7)$$

According to the equation of motion, the total interacted force \mathbf{F}^b on all ions of species b in the incident flux is given by Eqs. (2.6) and (2.7) as the time rate of change of their total momentum,

$$\mathbf{F}^b = \dot{\mathbf{p}} = \frac{\Delta \mathbf{p}_b^{\text{TOTAL}}}{1\text{s}}. \quad (2.8)$$

The resultant force $\mathbf{F}^{a,\text{fixed}}$ exerted on the fixed test particle of species a is then deduced from the law of action and reaction,

$$\mathbf{F}^{a,\text{fixed}} = -\mathbf{F}^b = -\frac{\Delta \mathbf{p}_b^{\text{TOTAL}}}{1\text{s}} \quad (2.9)$$

$$= (4\pi m_b n_b u^2 \rho_\perp^2) \int_0^\infty \frac{\rho}{\rho^2 + \rho_\perp^2} d\rho \left(\frac{\mathbf{u}}{u} \right). \quad (2.10)$$

¹The following assumptions have been adopted,

- Binary Collision Approximation, i.e. the charged particle of species a interacts with only a single ion of species b in the flux, at any given instant of time.
- The Coulomb potential field is described by the classical approximation. The charged particles are considered as sufficiently small spheres, i.e. their internal distribution of the electrons and protons is neglected.
- No effect of quantum mechanics.

2.1. KINETIC TRANSPORT THEORY OF CHARGED TEST PARTICLE IN PLASMAS

The integral in Eq. (2.10) converges with a finite value called *Coulomb logarithm* (See Appendix A). Hereafter it is written as

$$\ln \Lambda := \int \frac{\rho}{\rho^2 + \rho_{\perp}^2} d\rho. \quad (2.11)$$

For typical tokamak plasmas, the value of Coulomb logarithm is about $\ln \Lambda = 10 \sim 17$ [18].

Finally, the force $\mathbf{F}^{a,\text{fixed}}$ exerted on the infinitely heavy test particle of species a by the spatially uniform flux of the ions of species b is

$$\begin{aligned} \mathbf{F}^{a,\text{fixed}} &= (4\pi m_b n_b u^2 \rho_{\perp}^2) (\ln \Lambda) \cdot \left(\frac{\mathbf{u}}{u} \right) \\ &= \frac{q_a^2 q_b^2 n_b}{4\pi \epsilon_0^2 m_b} (\ln \Lambda) \cdot \left(\frac{\mathbf{u}}{u^3} \right). \end{aligned} \quad (2.12)$$

In the next section, the formula of Coulomb collisional force will be further extended to more realistic situation.

2.1.3 Force on a moving test particle by Coulomb collisions with background ions

The formula Eq. (2.12) is extended to more realistic situation. Now we suppose that the test particle of species a with a finite mass m_a is moving with a velocity \mathbf{v} through a background plasma consisting of ions of species b whose velocity distribution is an arbitrary function $f_b(\mathbf{v}_b)$. Figure 2.3 is a schematic of Coulomb collision event between these particles of species a and b . The objective is to find the force \mathbf{F}^a acting on the test particle of species a exerted by Coulomb collisions with the background ions of species b .

The velocity distribution function $f_b(\mathbf{v}_b)$ is normalized to the number density of plasma ions n_b ,

$$\iiint f_b(\mathbf{v}_b) d\mathbf{v}_b = n_b. \quad (2.13)$$

The number density of the ions of species b moving with a specific velocity \mathbf{v}'_b is given by

$$dn_b(\mathbf{v}'_b) = f_b(\mathbf{v}'_b) d\mathbf{v}_b. \quad (2.14)$$

The binary collision approximation is assumed, only two-particle interaction is considered.

We apply the results obtained in the previous section 2.1.2 to the present problem. We make use of an interpretation that the background plasma ions is made up of elementary uniform fluxes of the ions of species b with a specific velocity \mathbf{v}'_b and a number density $dn_b(\mathbf{v}'_b)$. The total force \mathbf{F}^a on the test particle of species a is then, obtained by summing up all contribution from each elementary flux of the ions of species b . According to Coulomb's law, the equations of motion of the interacting two

2.1. KINETIC TRANSPORT THEORY OF CHARGED TEST PARTICLE
IN PLASMAS

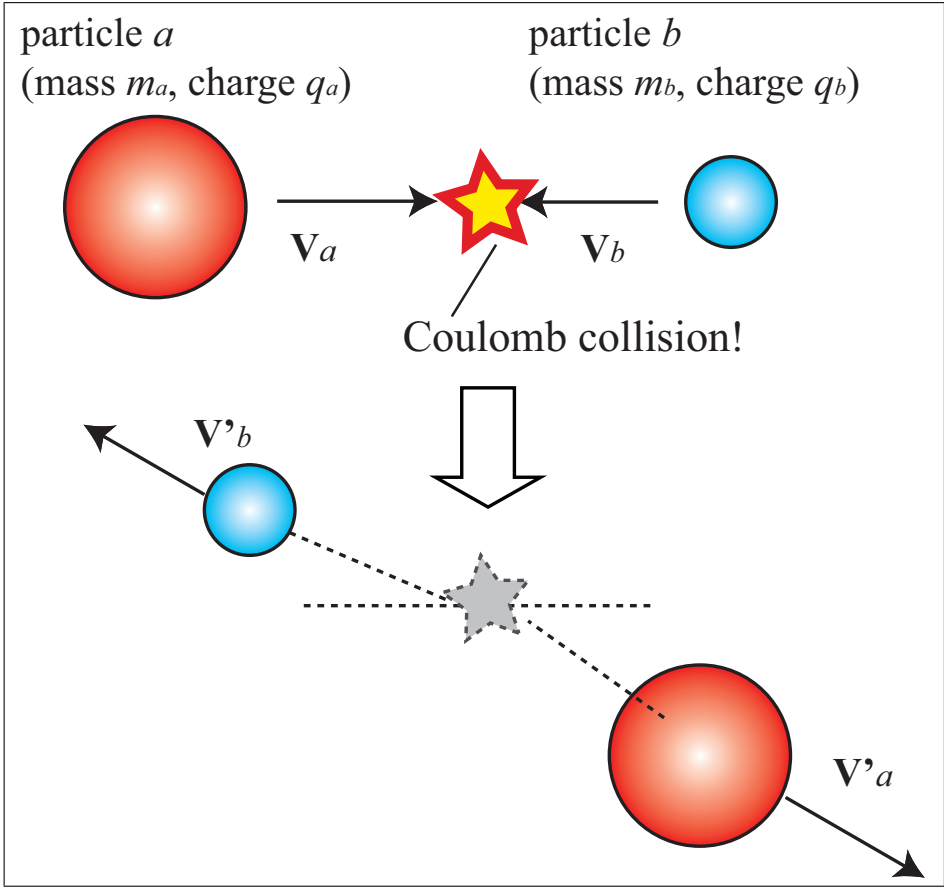


Figure 2.3: Schematic drawing of Coulomb collision event.

2.1. KINETIC TRANSPORT THEORY OF CHARGED TEST PARTICLE IN PLASMAS

particles of species a (mass: m_a , charge: q_a , position: \mathbf{r}_a) and b (mass: m_b , charge: q_b , position: \mathbf{r}_b) are described as,

$$\begin{aligned} \text{Test particle (species } a\text{): } \quad m_a \ddot{\mathbf{r}}_a &= \frac{q_a q_b}{4\pi\epsilon_0} \cdot \frac{(\mathbf{r}_a - \mathbf{r}_b)}{|\mathbf{r}_a - \mathbf{r}_b|^3}, \\ \text{Background ion (species } b\text{): } \quad m_b \ddot{\mathbf{r}}_b &= \frac{q_b q_a}{4\pi\epsilon_0} \cdot \frac{(\mathbf{r}_b - \mathbf{r}_a)}{|\mathbf{r}_b - \mathbf{r}_a|^3}. \end{aligned} \quad (2.15)$$

These motions are described more clearly in the frame of center-of-mass coordinates. The position of the center-of-mass \mathbf{R} and the relative distance \mathbf{r} between the two particles are introduced,

$$\mathbf{R} := \frac{m_a \mathbf{r}_a + m_b \mathbf{r}_b}{m_a + m_b}, \quad (2.16)$$

$$\mathbf{r} := \mathbf{r}_a - \mathbf{r}_b. \quad (2.17)$$

These center-of-mass coordinates are related to the original coordinates by,

$$\begin{aligned} \mathbf{r}_a &= \mathbf{R} + \frac{m_b}{m_a + m_b} \mathbf{r}, \\ \mathbf{r}_b &= \mathbf{R} - \frac{m_a}{m_a + m_b} \mathbf{r}. \end{aligned} \quad (2.18)$$

Substituting Eq. (2.18) in Eq.(2.15), we obtain the equation of motion for the center-of-mass coordinate system,

$$\ddot{\mathbf{R}} = \mathbf{0} \quad (\because \dot{\mathbf{R}} = \mathbf{V}: \text{constant.}) \quad (2.19)$$

$$\mu_{ab} \ddot{\mathbf{r}} = \frac{q_a q_b}{4\pi\epsilon_0} \cdot \frac{\mathbf{r}}{r^3}, \quad (2.20)$$

where $\mu_{ab} = m_a m_b / (m_a + m_b)$ is the reduced mass.

From analogy to Eq. (2.1), Eq. (2.20) represents the equation of motion of a virtual particle (mass: μ_{ab} , electric charge: q_b , position: \mathbf{r}) which is in interaction with an imaginary fixed particle (mass: ∞ , electric charge: q_a , the position is at the coordinate origin $\mathbf{0}$). We suppose that a spatially uniform flux of such virtual particles with the mass μ_{ab} is coming with the velocity $\dot{\mathbf{r}} (\equiv \mathbf{v} - \mathbf{v}'_b)$, to be scattered by the imaginary fixed particle. Since Eq.(2.20) is identical with Eq. (2.1), the same argument as in the section 2.1.2 can be applied, after the following substitutions are made,

$$m \longrightarrow \mu_{ab}, \quad (2.21)$$

$$n_b \longrightarrow dn_b(\mathbf{v}_b), \quad (2.22)$$

$$\mathbf{u} \longrightarrow \dot{\mathbf{r}} = \mathbf{v} - \mathbf{v}'_b, \quad (2.23)$$

$$\mathbf{r}_b = \mathbf{0}. \quad (2.24)$$

Therefore, by making use of Eqs. (2.9) and (2.12) focusing on \mathbf{F}^b , the collisional force exerted on the elementary flux of virtual particles of the mass μ_{ab} is

$$d\mathbf{F} = -\frac{q_a^2 q_b^2}{4\pi\epsilon_0^2 \mu_{ab}} (\ln \Lambda) \cdot \frac{\mathbf{v} - \mathbf{v}'_b}{|\mathbf{v} - \mathbf{v}'_b|^3} f_b(\mathbf{v}'_b) d\mathbf{v}'_b. \quad (2.25)$$

2.1. KINETIC TRANSPORT THEORY OF CHARGED TEST PARTICLE IN PLASMAS

We multiply the first equation in Eq.(2.18) by m_a , and then differentiate it twice with respect to the time. Using the Eq.(2.19), we arrive at the following equation,

$$m_a \ddot{\mathbf{r}}_a = m_a \ddot{\mathbf{R}} + \mu_{ab} \ddot{\mathbf{r}} = \mu_{ab} \ddot{\mathbf{r}}. \quad (2.26)$$

That is to say, the force acting on the test particle of species a in the given interaction is equal to the force exerted on the virtual particle with the mass μ_{ab} . Integrating over all contributions of ion fluxes of species b with velocity \mathbf{v}'_b , we obtain the collisional force acting on the test particle of species a moving with the velocity \mathbf{v} through the plasma composed of ions of species b ,

$$\begin{aligned} \mathbf{F}^a(\mathbf{v}) &= \int d\mathbf{F} \\ &= -\frac{q_a^2 q_b^2}{4\pi\epsilon_0^2 \mu_{ab}} (\ln \Lambda) \cdot \iiint \frac{\mathbf{v} - \mathbf{v}'_b}{|\mathbf{v} - \mathbf{v}'_b|^3} f_b(\mathbf{v}'_b) d\mathbf{v}'_b. \end{aligned} \quad (2.27)$$

The Coulomb logarithm $\ln \Lambda$ has been treated as constant in the integration over the velocities \mathbf{v}_b of background ions of species b (See Appendix A.2).

The velocity space integral in Eq.(2.27) is difficult to calculate straightforwardly, because the integrand function has a singularity point at $\mathbf{v}'_b = \mathbf{v}$. For its calculation, we introduce the *Rosenbluth potential function* [31] $\Psi(\mathbf{v}_a)$ defined as

$$\Psi_b(\mathbf{v}) = -\frac{1}{8\pi} \iiint |\mathbf{v} - \mathbf{v}_b| f_b(\mathbf{v}_b) d\mathbf{v}_b. \quad (2.28)$$

The background velocity distribution $f_b(\mathbf{v}_b)$ is taken into consideration through the potential Ψ_b .

The following relations are useful for the subsequent analysis.

$$\Delta_{\mathbf{v}} |\mathbf{v} - \mathbf{v}_b| \equiv \left(\frac{\partial^2}{\partial v_x^2} + \frac{\partial^2}{\partial v_y^2} + \frac{\partial^2}{\partial v_z^2} \right) |\mathbf{v} - \mathbf{v}_b| = \frac{2}{|\mathbf{v} - \mathbf{v}_b|}, \quad (2.29)$$

$$\nabla_{\mathbf{v}} \frac{1}{|\mathbf{v} - \mathbf{v}_b|} \equiv \left(\frac{\partial}{\partial v_x} \mathbf{e}_x + \frac{\partial}{\partial v_y} \mathbf{e}_y + \frac{\partial}{\partial v_z} \mathbf{e}_z \right) \frac{1}{|\mathbf{v} - \mathbf{v}_b|} = -\frac{\mathbf{v} - \mathbf{v}_b}{|\mathbf{v} - \mathbf{v}_b|^3}, \quad (2.30)$$

where $\Delta_{\mathbf{v}}$ and $\nabla_{\mathbf{v}}$ are the Laplacian and the gradient operator in the velocity space.

The integral in Eq.(2.27) is related to the potential Ψ_b as follows

$$\Delta_{\mathbf{v}} \Psi_b(\mathbf{v}) = -\frac{1}{4\pi} \iiint \frac{f_b(\mathbf{v}_b)}{|\mathbf{v} - \mathbf{v}_b|} d\mathbf{v}_b, \quad (2.31)$$

$$\iiint \frac{\mathbf{v} - \mathbf{v}_b}{|\mathbf{v} - \mathbf{v}_b|^3} f_b(\mathbf{v}_b) d\mathbf{v}_b = 4\pi \nabla_{\mathbf{v}} (\Delta_{\mathbf{v}} \Psi_b(\mathbf{v})) \quad (2.32)$$

Notice that the derivative operators $\Delta_{\mathbf{v}}$ and $\nabla_{\mathbf{v}}$ are in terms of the test particle velocity \mathbf{v} , while the volume integral is performed with respect to the background ion velocity \mathbf{v}_b . The order of integral and derivatives have been exchanged.

2.2. VELOCITY DISTRIBUTION FUNCTION OF BACKGROUND PLASMA IONS

Finally, by using Eqs. (2.27) and (2.32), the Coulomb collisional force \mathbf{F}_a on test particle of species a is analytically obtained as

$$\mathbf{F}^a(\mathbf{v}) = -\frac{q_a^2 q_b^2}{\epsilon_0^2 \mu_{ab}} (\ln \Lambda) \cdot \nabla_{\mathbf{v}} (\Delta_{\mathbf{v}} \Psi_b(\mathbf{v})). \quad (2.33)$$

It is determined by the velocity \mathbf{v} of the test particle of species a and the velocity distribution $f_b(\mathbf{v}_b)$ of the background plasma ions of species b . In the next section, we try to specify the velocity distribution function f_b of magnetized background plasma ions with a temperature gradient.

2.2 Velocity distribution function of background plasma ions

When a temperature gradient exists in the background plasma, its velocity distribution function f_b changes from well-known equilibrium Maxwellian. From Eqs. (2.28) and (2.33), the Coulomb collisional force on a test particle changes accordingly. Such difference in force due to temperature gradient is defined as *thermal force*. Here we try to find the background distribution function f_b in a magnetized plasma with temperature gradient. The following arguments are mainly based on the reference [44].

The behavior of background plasma ions and electrons are described by a *distribution function* $f_b(\mathbf{r}, \mathbf{v}, t)$. The function f_b of particle species b (mass m_b , electric charge q_b) is defined as the number of particles of that species per volume element in the six-dimensional phase space $d\mathbf{r}d\mathbf{v}$ (3D-real space + 3D-velocity space), near a given point (\mathbf{r}, \mathbf{v}) at the time t . The number of ions of species b moving with a velocity \mathbf{v}' at a position \mathbf{r}' at a time t' is given by $f_b(\mathbf{r}', \mathbf{v}', t') d\mathbf{r}d\mathbf{v}$.

All plasma parameters, such as the number density of particles in real space $n_b(\mathbf{r}, t)$, their flow velocity $\bar{\mathbf{v}}_b(\mathbf{r}, t)$, their temperature $T_b(\mathbf{r}, t)$, and their conductive heat flux density $\mathbf{q}_b(\mathbf{r}, t)$, are obtained by taking the moments of f_b as follows,

$$n_b(\mathbf{r}, t) := \int f_b(\mathbf{r}, \mathbf{v}, t) d\mathbf{v} \quad [\text{m}^{-3}], \quad (2.34)$$

$$\bar{\mathbf{v}}_b(\mathbf{r}, t) := \frac{1}{n_b} \int \mathbf{v} f_b(\mathbf{r}, \mathbf{v}, t) d\mathbf{v} \quad [\text{ms}^{-1}], \quad (2.35)$$

$$\frac{3}{2} T_b(\mathbf{r}, t) := \frac{1}{n_b} \int \left(\frac{m_b \mathbf{w}^2}{2} \right) f_b(\mathbf{r}, \mathbf{v}, t) d\mathbf{v} \quad [\text{J}], \quad (2.36)$$

$$\mathbf{q}_b(\mathbf{r}, t) := \int \left(\frac{m_b \mathbf{w}^2}{2} \mathbf{w} \right) f_b(\mathbf{r}, \mathbf{v}, t) d\mathbf{v} \quad [\text{Jm}^{-2}\text{s}^{-1}], \quad (2.37)$$

where the random velocity $\mathbf{w} := \mathbf{v} - \bar{\mathbf{v}}_b$ has been introduced. In contrast to the average flow velocity $\bar{\mathbf{v}}_b$, the random velocity \mathbf{w} represents the thermal agitation of ions. The temperature T_b is defined in joules in such a manner that $3T_b/2$ represents the average kinetic energy associated with the random

2.2. VELOCITY DISTRIBUTION FUNCTION OF BACKGROUND PLASMA IONS

velocity of particles. The conductive heat flux density \mathbf{q}_b is defined as the time rate of heat energy transfer per unit area by random motion of particles. The heat flux \mathbf{q}_b occurs by the presence of spatial temperature gradient ∇T_b .

Such velocity distribution function f_b obeys the *kinetic equation* (or the *Boltzmann equation*) [19],

$$\frac{\partial f_b}{\partial t} + \mathbf{v} \cdot \nabla f_b + \frac{q_b}{m_b} (\mathbf{E} + \mathbf{v} \times \mathbf{B}) \cdot \nabla_{\mathbf{v}} f_b = C_b(f_b), \quad (2.38)$$

which is deduced from the particle conservation law in the phase space $(\mathbf{r}, \mathbf{v}, t)$. The operators ∇ and $\nabla_{\mathbf{v}}$ are the gradient, respectively, with respect to the real space coordinates \mathbf{r} and the velocity space \mathbf{v} . The applied electro-magnetic field are expressed by \mathbf{E} and \mathbf{B} . The term $C_b(f_b)$ in the right hand side of the equation is the *collision operator*, representing the time rate of change in the distribution function f_b caused by velocity scattering of Coulomb collisions². The collision operator is a sum of contributions from all interacting particle species (including the like-particle collisions),

$$C_b(f_b) := \sum_{\gamma} C_{b/\gamma}, \quad (2.39)$$

where $C_{b/\gamma}$ is the contribution by collisions with γ -particles, and γ includes the species b itself.

In the scope of impurity transport simulation, it is sufficient to look for the stationary solution of plasma *ion distribution* f_b . It is because that the Coulomb interaction between impurities and background plasma ions is dominantly stronger than that between impurities and electrons, due to the much lighter mass of electrons ($m_a \geq m_b \gg m_e$) [13, 19]. The state of electrons f_e can be neglected as far as the impurity transport is considered. Therefore, we impose the following restrictions to solve Eq. (2.38),

1. The time dependent term is ignored ($\partial f_b / \partial t = 0$).
2. The *trace-impurity limit* is adopted, i.e. the amount of impurities are too small to affect the state of background ions ($C_{b/Z} = 0$).
3. As far as we consider the deuterium for background plasma ion species ($m_b = m_{D^+}$), collision with electrons can be neglected because of the large mass difference ($m_b \gg m_e$) [13, 19]. Together with the trace-impurity limit, the collision operator C_b for background ions is determined by the like-particle collisions, $C_b = C_{b/b} + C_{b/e} + C_{b/Z} \approx C_{b/b}$.

Consequently, the Eq. (2.38) becomes

$$\mathbf{v} \cdot \nabla f_b + \frac{q_b}{m_b} (\mathbf{E} + \mathbf{v} \times \mathbf{B}) \cdot \nabla_{\mathbf{v}} f_b = C_{b/b}(f_b). \quad (2.40)$$

Our aim in this section is to deduce a steady-state solution f_b for background ions satisfying Eq. (2.40).

²In Eq. (2.38), the source/sink terms other than Coulomb collision, such as contributions of the ionization and recombination reactions, are not considered.

2.2. VELOCITY DISTRIBUTION FUNCTION OF BACKGROUND PLASMA IONS

2.2.1 Collision operator $C_{b/b}$

The operator $C_{b/b}(f_b)$ for background ion-ion (i.e. like-particle) collisions in Eq. (2.40) is given in the form [44]

$$C_{b/b}(\mathbf{v}, f_b(\mathbf{v})) := \iint u \sigma_{b/b}(u, \theta) \times \{f_b(\mathbf{v}')f_b(\mathbf{v}'_{\text{in}}) - f_b(\mathbf{v})f_b(\mathbf{v}_{\text{in}})\} d\mathbf{v}_{\text{in}} d\Omega. \quad (2.41)$$

To describe the like-particle collision, let \mathbf{v} be the velocity of the criterial background plasma ion, and \mathbf{v}_{in} be the velocity of other background ions coming to collide. The integral is taken over such incoming background ions ($d\mathbf{v}_{\text{in}}$). The relative velocity of the two colliding ions before and after the collision are expressed, respectively, as $\mathbf{u} := \mathbf{v} - \mathbf{v}_{\text{in}}$ and $\mathbf{u}' := \mathbf{v}' - \mathbf{v}'_{\text{in}}$. The magnitude of relative velocity does not change by collision $|\mathbf{u}'| = |\mathbf{u}| =: u$, because we consider the Coulomb collisions to be elastic. The symbol $d\Omega$ is the element of solid angle in the direction of post-collision velocity \mathbf{v}' of the criterial particle. The Rutherford scattering cross section [33] for Coulomb collision between particle species a and b is defined, in the SI unit system, by

$$\sigma_{a/b}(u, \theta) := \left(\frac{q_a q_b}{8\pi \epsilon_0 \mu_{ab} u^2} \right)^2 \frac{1}{\sin^4 \frac{\theta}{2}}, \quad (2.42)$$

with the vacuum permittivity ϵ_0 and the reduced mass $\mu_{ab} := m_a m_b / (m_a + m_b)$.

2.2.2 Solution for the case of $\nabla T_b = 0$

When there is no background temperature gradient $\nabla T_b = 0$, the stationary solution f_b of Eq. (2.40) is given by a local Maxwellian velocity distribution [19]

$$f_{\text{Max}}(\mathbf{r}, \mathbf{v}, t) := n_b(\mathbf{r}, t) \left(\frac{m_b}{2\pi T_b(\mathbf{r}, t)} \right)^{3/2} \exp \left[\frac{m_b \{\mathbf{v} - \overline{\mathbf{v}}_b(\mathbf{r}, t)\}^2}{2T_b(\mathbf{r}, t)} \right]. \quad (2.43)$$

The magnetic term $(\mathbf{v} \times \mathbf{B}) \cdot \nabla_{\mathbf{v}} f_b$ and the collision operator $C_{b/b}(f_b)$ vanish separately with the Maxwellian distribution f_{Max} . The remaining terms $\mathbf{v} \cdot \nabla f_b$ and $\mathbf{E} \cdot \nabla_{\mathbf{v}} f_b$ are estimated as negligibly small [19].

2.2.3 Solution for the case of $\nabla T_b \neq 0$

The background plasma ions are supposed to have a temperature gradient $\nabla T_b = \nabla_{\parallel} T_b + \nabla_{\perp} T_b$, which is composed of *parallel* ($\nabla_{\parallel} T_b \parallel \mathbf{B}$) and *perpendicular* component ($\nabla_{\perp} T_b \perp \mathbf{B}$). We solve Eq. (2.40) by the perturbation method.

For fusion plasma conditions, the following orderings are usually satisfied,

$$\lambda_{\text{MFP}}/L_{\parallel} \ll 1 \text{ and } \rho_b/L_{\perp} \ll 1, \quad \textit{High collisionality limit} \quad (2.44)$$

$$\nu_{bb}/\Omega_b \ll 1. \quad \textit{Strongly magnetized limit} \quad (2.45)$$

2.2. VELOCITY DISTRIBUTION FUNCTION OF BACKGROUND PLASMA IONS

The mean-free path λ_{MFP} is defined as $\lambda_{\text{MFP}} := v_{T_b}/\nu_{bb}$, with the thermal speed of background ion $v_{T_b} := \sqrt{2T_b/m_b}$ and the Coulomb collision frequency $\nu_{bb} := \sqrt{2}n_bq_b^4(\ln \Lambda)/(12\pi^{3/2}\epsilon_0^2T_b^{3/2}\sqrt{m_b})$. The Larmor gyro-frequency Ω_b is defined by $\Omega_b := q_b|\mathbf{B}|/m_b$, and the Larmor gyro-radius ρ_b is $\rho_b := v_{T_b}/|\Omega_b|$. The scale length $L_{\parallel} := (\nabla_{\parallel}^{-1})$ and $L_{\perp} := (\nabla_{\perp}^{-1})$ have been introduced. They are characteristic length of spatial gradient of macroscopic plasma parameters, i.e. a distance needed for n_b , T_b , and \mathbf{B} to vary substantially. The reason to have such anisotropic scale length is that, in a magnetized plasma, the gradients are often very different along(\parallel) / across(\perp) the magnetic field \mathbf{B} . In order to move the discussion forward, we assume that the small parameters in Eqs. (2.44) and (2.45) are approximately in the same order of magnitude,

$$\begin{aligned}\frac{\lambda_{\text{MFP}}}{L_{\parallel}} &\sim \delta \ll 1, \\ \frac{\rho_b}{L_{\perp}} &\sim \delta \ll 1, \\ \frac{\nu_{bb}}{\Omega_b} &\sim \delta \ll 1.\end{aligned}\tag{2.46}$$

We expand the distribution function f_b accordingly,

$$\begin{aligned}f_b &= f_0 + f_1 + \dots, \\ \frac{f_1}{f_0} &\sim \delta.\end{aligned}\tag{2.47}$$

We substitute such f_b in the kinetic equation Eq. (2.40), to obtain a series of equations classified by the order of small parameter δ ,

Lowest order (δ^{-1})

$$C_{b/b}(f_0) - \frac{q_b}{m_b}(\mathbf{v} \times \mathbf{B}) \cdot \nabla_{\mathbf{v}} f_0 = 0,\tag{2.48}$$

Next order (δ^0)

$$C_{b/b}(f_1) - \frac{q_b}{m_b}(\mathbf{v} \times \mathbf{B}) \cdot \nabla_{\mathbf{v}} f_1 = \left[\left(\frac{\nabla n_b}{n_b} - \frac{q_b \mathbf{E}}{T_b} \right) + \left(\frac{m_b |\mathbf{v}|^2}{2T_b} - \frac{3}{2} \right) \frac{\nabla T_b}{T_b} \right] f_0 \cdot \mathbf{v}.\tag{2.49}$$

The solution of lowest order equation Eq. (2.48) is a local Maxwellian f_{Max} (Eq. (2.43)) because of $C_{b/b}(f_{\text{Max}}) = 0$ and $(\mathbf{v} \times \mathbf{B}) \cdot \nabla_{\mathbf{v}} f_{\text{Max}} = 0$. In the next order equation Eq. (2.49), notice that the collision operator and the gradient in velocity space in the left hand side are acting on the small perturbation function f_1 . Since the right hand side is already known, Eq. (2.49) can be solved according to the solutions presented in Refs. [44, 14, 19] (The detail is omitted here).

From Eqs. (2.48) and (2.49), the background ion distribution f_b is finally specified as,

$$\begin{aligned}f_b(\mathbf{v}_b) &= f_0 + f_1 \\ &= n_b \left(\frac{m_b}{2\pi T_b} \right)^{\frac{3}{2}} \exp \left(-\frac{m_b w^2}{2T_b} \right) \times \left[1 - \frac{m_b}{n_b} \frac{1}{T_b^2} \left(1 - \frac{w^2}{5v_{th,b}^2} \right) (\mathbf{q}_b \cdot \mathbf{w}) \right],\end{aligned}\tag{2.50}$$

2.2. VELOCITY DISTRIBUTION FUNCTION OF BACKGROUND PLASMA IONS

where the random velocity of background ion is defined as $\mathbf{w} := \mathbf{v} - \overline{\mathbf{v}}_b$, together with the background flow velocity $\overline{\mathbf{v}}_b$ given in Eq. (2.35). The thermal speed of background ion is defined as $v_{th,b} := \sqrt{T_b/m_b}$. The equation (2.50) is called the *distorted Maxwellian* distribution representing the velocity distribution of magnetized plasma ions with temperature gradient ∇T_b . The conductive heat flux density vector \mathbf{q}_b is formulated in the classical limit [14, 19]. The following assumptions are supposed for \mathbf{q}_b :

- The background plasma is sufficiently collisional. The neo-classical transport and the anomalous transport processes are not considered.
- Background plasma is composed of single ion species and electrons.
- The plasma parameters of the background *ions* are determined by the ion-ion collisions. Collisions with the electrons are neglected.
- Background plasma is not affected by the presence of test particles (Trace impurity limit).
- The spatial gradient of background flow velocity, i.e. the viscous stress tensor, is negligible. Therefore, the force due to the viscosity can be neglected.
- Background plasma is strongly magnetized, $\Omega_b \tau_b \gg 1$.
- Background pressure gradient ∇p and electric field \mathbf{E} are not taken into account.

Under these assumptions, the heat flux density \mathbf{q}_b is

$$\mathbf{q}_b = -\kappa_{\parallel} \nabla_{\parallel} T_b + \kappa_{\wedge} (\mathbf{e}_{\parallel} \times \nabla_{\perp} T_b) - \kappa_{\perp} \nabla_{\perp} T_b. \quad (2.51)$$

The background temperature gradient ∇T_b is incorporated in our model at this stage. In Eq. (2.51), the heat conductivities κ_{\parallel} , κ_{\wedge} , and κ_{\perp} are given as [19]

$$\kappa_{\parallel} := 3.9 \frac{n_b T_b \tau_b}{m_b}, \quad (2.52)$$

$$\kappa_{\wedge} := \frac{5 n_b T_b}{2 m_b \Omega_b}, \quad (2.53)$$

$$\kappa_{\perp} := 2 \frac{n_b T_b}{m_b \Omega_b^2 \tau_b}, \quad (2.54)$$

where the characteristic collision time τ_b of background ion is defined by

$$\tau_b := 12 \pi^{\frac{3}{2}} \frac{\epsilon_0^2 \sqrt{m_b} T_b^{3/2}}{n_b q_b^4 (\ln \Lambda)}. \quad (2.55)$$

The collision time τ_b is identical with $\sqrt{2} \tau_{ii}^B$, where the background ion-ion collision time τ_{ii}^B is given by the formula (1.5) in Ref. [19] (as Braginskii's definition). Hereafter, the index \parallel , \perp , \wedge are used

2.3. THERMAL FORCE

to distinguish the *parallel* direction $\mathbf{e}_{\parallel} := \mathbf{B}/B$, the *perpendicular* direction $\mathbf{e}_{\perp} := \nabla_{\perp} T_b / |\nabla_{\perp} T_b|$, and the direction $\mathbf{e}_{\wedge} := \mathbf{e}_{\parallel} \times \mathbf{e}_{\perp}$ perpendicular to both \mathbf{B} and $\nabla_{\perp} T_b$, which is called the *diamagnetic* direction .

Absolute values of each component of \mathbf{q}_b are different by the factor of $\Omega_b \tau_b$,

$$q_{b,\parallel} : q_{b,\wedge} : q_{b,\perp} = |\nabla_{\parallel} T_b| : \frac{1}{\Omega_b \tau_b} |\nabla_{\perp} T_b| : \left(\frac{1}{\Omega_b \tau_b} \right)^2 |\nabla_{\perp} T_b|. \quad (2.56)$$

The factor $\Omega_b \tau_b$ represents a degree of magnetization of the background plasma.

It should be noted that, once we know a suitable formula of the heat flux density \mathbf{q}_b , the same formula as Eq. (2.50) can be employed to calculate the thermal force (See Eq. (2.59)). For example, we may be able to model more realistic background plasmas by substituting another formula of \mathbf{q}_b given in Ref. [42] which includes the heat flux limiter.

2.3 Thermal force

The thermal force and its characteristic features, including the temperature screening effect, are presented in detail.

We are considering a test particle (species: a) moving in a background plasma with velocity \mathbf{v}_a . The test particle of species a experiences Coulomb collisions with background plasma ions (species: b). The background ions have temperature gradient ∇T_b , and their velocity distribution is modeled by a distorted Maxwellian f_b in Eq. (2.50).

By substituting such f_b in the formulas Eqs. (2.28) and (2.33), the kinetic force \mathbf{F} on the test particle by Coulomb collisions with magnetized background plasma ions is analytically obtained as

$$\mathbf{F} = \mathbf{F}^0 + \mathbf{F}^{\nabla T}, \quad (2.57)$$

where,

$$\mathbf{F}^0 = -\frac{C}{4\pi} \frac{n_b}{2T_b} \frac{\Phi(\tilde{v}_a) - \tilde{v}_a \Phi'(\tilde{v}_a)}{\tilde{v}_a^3} \cdot \tilde{\mathbf{v}}_a, \quad (2.58)$$

$$\mathbf{F}^{\nabla T} = -\frac{C}{10\pi\sqrt{\pi}} \sqrt{\frac{m_b}{2T_b}} \frac{1}{T_b^2} \exp(-\tilde{v}_a^2) \cdot [\mathbf{q}_b - 2(\mathbf{q}_b \cdot \tilde{\mathbf{v}}_a) \tilde{\mathbf{v}}_a]. \quad (2.59)$$

Here, we have introduced the following symbols,

$$C := (\ln \Lambda) \left(\frac{q_a q_b}{\epsilon_0} \right)^2 \left(1 + \frac{m_b}{m_a} \right), \quad (2.60)$$

$$\tilde{\mathbf{v}}_a := \sqrt{\frac{m_b}{2T_b}} (\mathbf{v}_a - \bar{\mathbf{v}}_b), \quad (2.61)$$

$$\Phi(v) := \frac{2}{\sqrt{\pi}} \int_0^v \exp(-t^2) dt, \quad (2.62)$$

$$\Phi'(v) := \frac{d\Phi(v)}{dv} = \frac{2}{\sqrt{\pi}} \exp(-v^2). \quad (2.63)$$

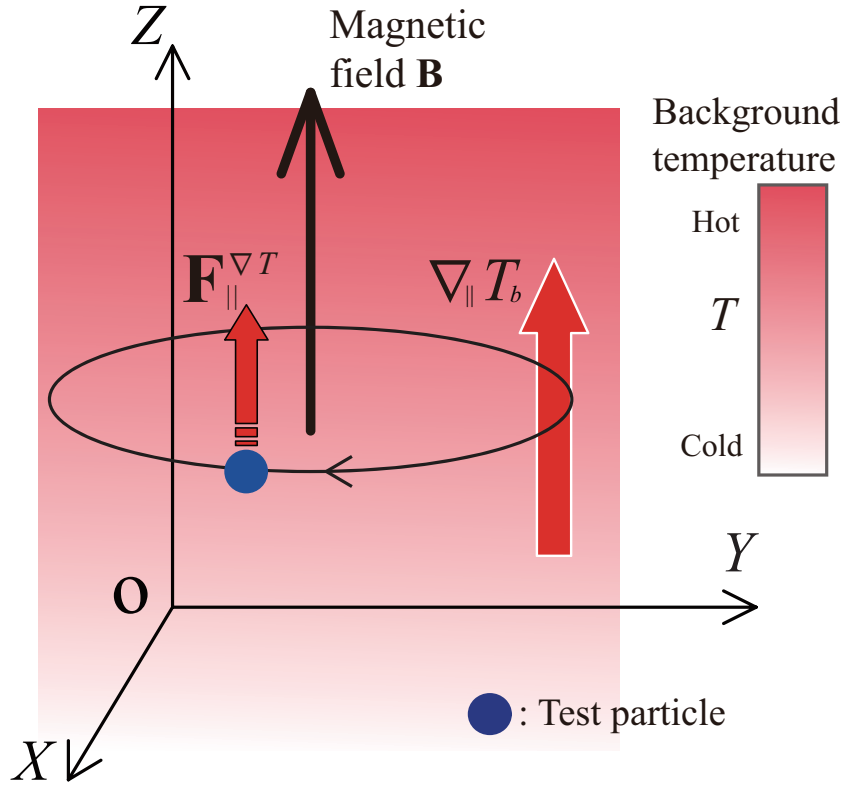


Figure 2.4: Parallel thermal force due to parallel temperature gradient $\nabla_{\parallel} T_b$. (cited from Ref. [30].)

The frictional force is denoted by \mathbf{F}^0 , and the thermal force is $\mathbf{F}^{\nabla T}$.

The frictional force \mathbf{F}^0 usually slows down the test particle, depending on its velocity \mathbf{v}_a and the background plasma flow $\bar{\mathbf{v}}_b$. Background temperature gradient does not affect \mathbf{F}^0 .

The thermal force $\mathbf{F}^{\nabla T}$ consists of the three components of different direction with respect to the B-field line,

$$\mathbf{F}^{\nabla T} = \mathbf{F}_{\parallel}^{\nabla T} + \mathbf{F}_{\wedge}^{\nabla T} + \mathbf{F}_{\perp}^{\nabla T}. \quad (2.64)$$

We will call such $\mathbf{F}_{\parallel}^{\nabla T}$, $\mathbf{F}_{\wedge}^{\nabla T}$, and $\mathbf{F}_{\perp}^{\nabla T}$, respectively as the *parallel* thermal force, the *diamagnetic* thermal force, and the *perpendicular* thermal force. The characteristics of these thermal forces are discussed in the following sections.

2.3.1 Parallel thermal force $\mathbf{F}_{\parallel}^{\nabla T}$

The parallel thermal force is caused by the parallel temperature gradient $\nabla_{\parallel} T_b$. From Eq. (2.51), the gradient $\nabla_{\parallel} T_b$ leads to a heat flux

$$\mathbf{q}_{b, \parallel} := -\kappa_{\parallel} \nabla_{\parallel} T_b = -3.9 \frac{n_b T_b \tau_b}{m_b} \nabla_{\parallel} T_b. \quad (2.65)$$

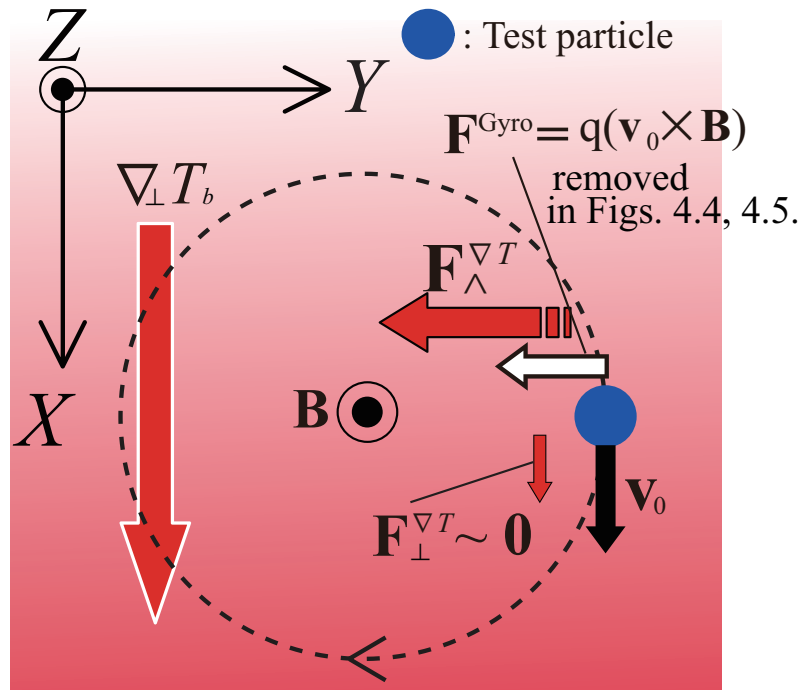


Figure 2.5: Thermal force due to perpendicular temperature gradient $\nabla_{\perp} T_b$: The diamagnetic thermal force $F_{\wedge}^{\nabla T}$ is much larger than the perpendicular thermal force $F_{\perp}^{\nabla T}$ under the strongly magnetized condition ($\Omega_b \tau_b \gg 1$). (cited from Ref. [30].)

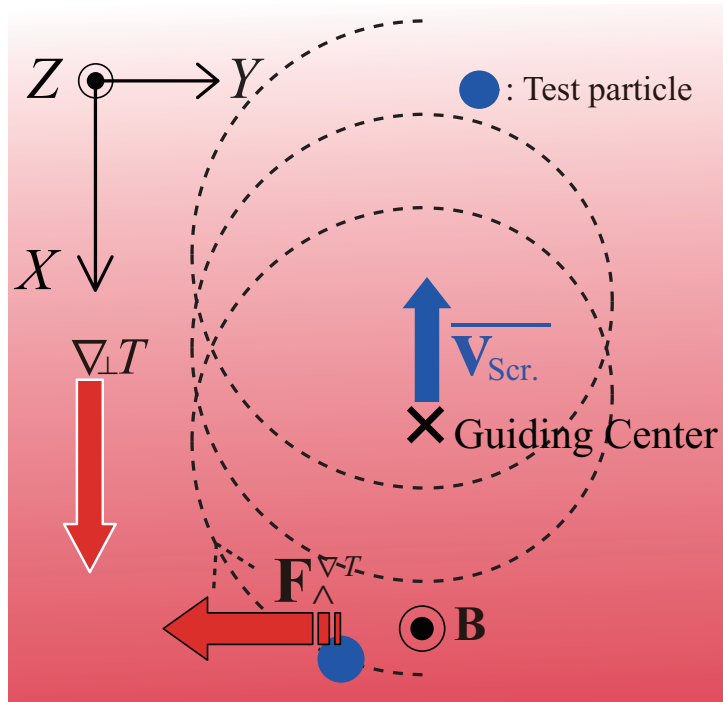


Figure 2.6: Temperature screening effect. (cited from Ref. [30].)

2.3. THERMAL FORCE

Substituting such $\mathbf{q}_{b, \parallel}$ in Eq. (2.59), we obtain the expression

$$\mathbf{F}_{\parallel}^{\nabla T} = \frac{(3.9) \cdot 12}{10\sqrt{2}} \left(1 + \frac{m_b}{m_a}\right) \left(\frac{q_a}{q_b}\right)^2 \exp(-\tilde{v}_a^2) \cdot [\nabla_{\parallel} T_b - 2(\nabla_{\parallel} T_b \cdot \tilde{\mathbf{v}}_a) \tilde{\mathbf{v}}_a]. \quad (2.66)$$

The parallel thermal force $\mathbf{F}_{\parallel}^{\nabla T}$ is characterized as follows.

- 1. Magnitude of the thermal force:** The magnitude of the parallel thermal force is proportional to that of the temperature gradient $|\mathbf{F}_{\parallel}^{\nabla T}| \propto |\nabla_{\parallel} T_b|$.
- 2. Thermal force on a slower test particle:** When a test particle moves much more slowly compared with the background thermal speed, meaning $|\tilde{v}_a| \ll 1$, the second term in the square brackets in Eq. (2.66) can be ignored³. Then, the thermal force acts in the direction of the temperature gradient,

$$\mathbf{F}_{\parallel}^{\nabla T} \propto \nabla_{\parallel} T_b, \quad (2.67)$$

driving the test particle from lower to higher temperature region along the magnetic field line. It is a distinguished feature of parallel thermal force, in contrast with other physical phenomena such as the diffusion where the transport occurs in the opposite direction to the number density gradient ∇n .

- 3. Thermal force on a faster test particle:** On the other hand, when the test particle moves faster than the background thermal speed ($|\tilde{\mathbf{v}}_a| \geq 1$), the second term in the square brackets in Eq. (2.66) becomes dominant, i.e. $\mathbf{F}_{\parallel}^{\nabla T} \propto -(\nabla_{\parallel} T_b \cdot \tilde{\mathbf{v}}_a) \tilde{\mathbf{v}}_a$. In this situation, if \mathbf{v}_a is parallel to the temperature gradient $\nabla_{\parallel} T_b$, then $\mathbf{F}_{\parallel}^{\nabla T}$ acts in the opposite direction to $\nabla_{\parallel} T_b$. It is a *reversal phenomenon* of parallel thermal force, and its mechanism is explained qualitatively as follows. When a test particle moves very fast along the temperature gradient, less background ions from the lower T_b region can catch up with the test particle. Consequently, the test particle collides only with ions coming from the higher T_b region, and the net force on the test particle is directed toward the lower T_b region.

As mentioned by Reiser *et al.* [17], this mechanism prevents test particles from being infinitely accelerated by the thermal force. While a test particle moves slowly along the temperature gradient, it is continuously accelerated by the parallel thermal force. However, it cannot exceed a certain velocity limit, at which the magnitude of parallel thermal force changes the sign.

- 4. Dependence on the background number density:** Parallel thermal force does not depend on the number density of background plasma n_b as seen in Eq. (2.66), whereas the frictional force is proportional to n_b .

³When considering high- Z heavy impurities for test particle, the condition $|\tilde{v}_a| \ll 1$ is almost always satisfied.

2.3. THERMAL FORCE

In the next chapter 3, we will check if these characteristics listed above can be correctly simulated by our numerical model.

2.3.2 Diamagnetic thermal force $\mathbf{F}_{\wedge}^{\nabla T}$ and perpendicular thermal force $\mathbf{F}_{\perp}^{\nabla T}$

The diamagnetic and perpendicular thermal force are caused by perpendicular temperature gradient $\nabla_{\perp} T_b$. Their characteristics are summarized here.

The diamagnetic thermal force $\mathbf{F}_{\wedge}^{\nabla T}$ acts on the test particle in the diamagnetic direction as shown in Fig. 2.5, and produces the *temperature screening effect (TSE)* [19]. The TSE is understood as a guiding center drift by the diamagnetic thermal force, as shown in Fig. 2.6. The test particles are transported, as a whole, to the opposite direction to $\nabla_{\perp} T_b$, i.e. perpendicularly from higher to lower temperature. The temperature screening effect may be non-negligible under steep temperature gradient in the edge region of fusion plasma (See Sec. 4.6.3). In existing impurity transport simulation codes, the perpendicular temperature gradient $\nabla_{\perp} T_b$ and the diamagnetic thermal force $\mathbf{F}_{\wedge}^{\nabla T}$ have not been taken into account yet.

It is also interesting to note that the diamagnetic thermal force does not include the collision time of background ions τ_b (See κ_{\wedge} in Eq. (2.53)). Even in a very hot plasma where Coulomb collisions occur less frequently ($\nu_b \propto \tau_b^{-1}$ with increased τ_b), e.g. in the core, the same magnitude of diamagnetic thermal force $\mathbf{F}_{\wedge}^{\nabla T}$ always occurs.

The perpendicular thermal force $\mathbf{F}_{\perp}^{\nabla T}$ acts along the perpendicular temperature gradient $\nabla_{\perp} T_b$ (See Fig. 2.5). However, $\mathbf{F}_{\perp}^{\nabla T}$ is negligibly small in the fusion plasmas. The reason is described as below.

When we consider the test particle to be heavier than the background ion, its velocity \tilde{v}_a normalized to the thermal speed of background ion is small ($\tilde{v}_a \ll 1$). Hence, the following relation holds from Eq. (2.59),

$$\mathbf{F}^{\nabla T} \propto -\mathbf{q}_b. \quad (2.68)$$

Due to the ordering of the heat flux components $q_{b,\parallel}$, $q_{b,\wedge}$, $q_{b,\perp}$ in Eq. (2.56), the same ordering is applied to each component of the thermal force,

$$|\mathbf{F}_{\parallel}^{\nabla T}| : |\mathbf{F}_{\wedge}^{\nabla T}| : |\mathbf{F}_{\perp}^{\nabla T}| = |\nabla_{\parallel} T_b| : \frac{1}{\Omega_b \tau_b} |\nabla_{\perp} T_b| : \left(\frac{1}{\Omega_b \tau_b} \right)^2 |\nabla_{\perp} T_b|. \quad (2.69)$$

Since fusion plasmas are strongly magnetized ($\Omega_b \tau_b \gg 1$), the perpendicular thermal force $\mathbf{F}_{\perp}^{\nabla T}$ becomes much smaller than the other forces such as the Lorentz force, the frictional force,

2.3. THERMAL FORCE

the parallel and the diamagnetic thermal force, roughly by a factor of $\Omega_b \tau_b$. In this study, the perpendicular thermal force $\mathbf{F}_{\perp}^{\nabla T}$ is neglected.

In the chapter 4, we will check the diamagnetic thermal force $\mathbf{F}_{\wedge}^{\nabla T}$ and its macroscopic effect on test particle transport, TSE.

Chapter 3

Numerical model of thermal force based on Monte Carlo Binary Collision model in unmagnetized plasma

This section describes a numerical model of thermal force in unmagnetized plasma. As an important first step toward our goal, we have started from such simpler case without magnetic field. In fact, this model can be applied straightforwardly for simulation of the parallel thermal force in magnetized plasma. It is because that the motion of charged particles along the \mathbf{B} -field line is not restricted by the Lorentz force, i.e. the equation of motion along \mathbf{B} -field is identical with the case without \mathbf{B} -field. Therefore, the thermal force in unmagnetized plasma is equivalent to the parallel thermal force in magnetized plasma.

Figure 3.1 presents graphically the basic concept of our thermal force model. Basic procedures of the model, for a single test particle at a single collision time step, are shown in Fig. 3.2. The details of Figs. 3.1 and 3.2 will be described step by step in Sec. 3.2.

By test simulations in the latter part of this chapter, we will check our new numerical model. The same characteristics as those of parallel thermal force mentioned in Sec. 2.3.1 will be examined.

3.1 Distorted Maxwellian and thermal force in unmagnetized plasma

Following the same discussion as in Chapter 2, we can derive velocity distribution function of unmagnetized plasma ions by solving the kinetic equation Eq. (2.38) without \mathbf{B} -field. The distorted

3.1. DISTORTED MAXWELLIAN AND THERMAL FORCE IN UNMAGNETIZED PLASMA

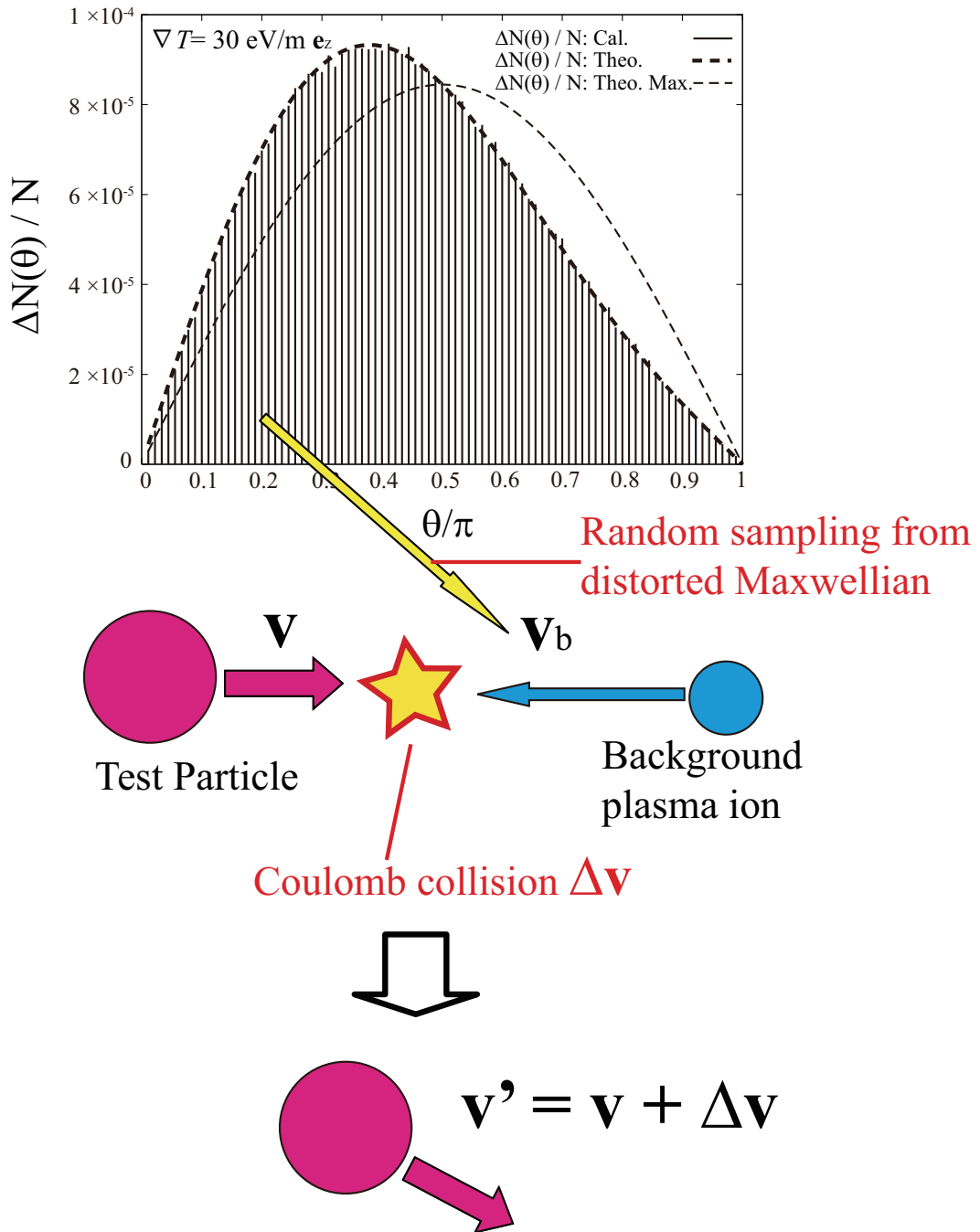


Figure 3.1: Basic concept of the present thermal force model.

Maxwellian distribution of unmagnetized plasma is given by [33, 50]

$$f_b(\mathbf{w}) = n_b \left(\frac{m_b}{2\pi T_b} \right)^{\frac{3}{2}} \exp \left(-\frac{m_b w^2}{2T_b} \right) \times \left[1 + A(T_b) \cdot \left(1 - \frac{w^2}{5v_{th,b}^2} \right) \left(\frac{\mathbf{w}}{v_{th,b}} \cdot \nabla T_b \right) \right], \quad (3.1)$$

where the coefficient $A(T_b)$ is defined as ¹

$$A(T_b) := \frac{75}{2} \pi^{3/2} \frac{\epsilon_0^2}{(\ln \Lambda)} \frac{T_b}{n_b q_b^4}. \quad (3.2)$$

Eq. (3.1) is basically the same function as the distorted Maxwellian in magnetized plasma in Eq. (2.50) caused by only parallel temperature gradient $\nabla T_b = \nabla_{\parallel} T_b$.

By substituting f_b in Eq. (2.33), the thermal force in unmagnetized plasma is analytically obtained as

$$\mathbf{F}_{\mathbf{B}=0}^{\nabla T} = \frac{15\sqrt{2}}{8} \left(1 + \frac{m_b}{m_a} \right) \left(\frac{q_a}{q_b} \right)^2 \exp(-\tilde{v}_a^2) \cdot [\nabla T_b - 2(\nabla T_b \cdot \tilde{\mathbf{v}}_a) \tilde{\mathbf{v}}_a]. \quad (3.3)$$

Equation (3.3) is expressed in the same manner as the parallel thermal force in Eq. (2.66). The same characteristic features in Sec. 2.3.1 are expected to be true for $\mathbf{F}_{\mathbf{B}=0}^{\nabla T}$.

3.2 Numerical model of the thermal force based on BCM

The basic steps of the present model are summarized as follows:

1. The parameters of the test particle and the background plasma are specified. The mass m_a , charge state Z_a , position $\mathbf{r}_a(t)$, and velocity $\mathbf{v}_a(t)$, of the test particle are given. As for the background plasma ions, the mass m_b , charge state Z_b , number density n_b , temperature T_b , temperature gradient ∇T_b , and flow velocity $\bar{\mathbf{v}}_b$, are necessary.
2. The velocity of a background ion \mathbf{v}_b , coming to collide with the test particle, is found from the distorted Maxwell distribution in Eq. (3.1) (given in Sec. 3.3.2). A detailed algorithm for this step will be explained in Sec. 3.3.
3. The Binary Collision Model (BCM) calculates the random scattering of test particle velocity $\Delta \mathbf{v}_a$ due to collisions with background ions. The BCM will be explained in Sec. 3.5.
4. Time is advanced by the collision time step, Δt . New velocity and position of the test particle are calculated:

$$\begin{aligned} \mathbf{v}_a(t + \Delta t) &= \mathbf{v}_a(t) + \Delta \mathbf{v}_a, \\ \mathbf{r}_a(t + \Delta t) &= \mathbf{r}_a(t) + \mathbf{v}_a(t) \Delta t. \end{aligned}$$

¹Roughly evaluated by $A(T_b) \sim \lambda_{\text{MFP}}/T_b$ (λ_{MFP} is the mean free path of background ions).

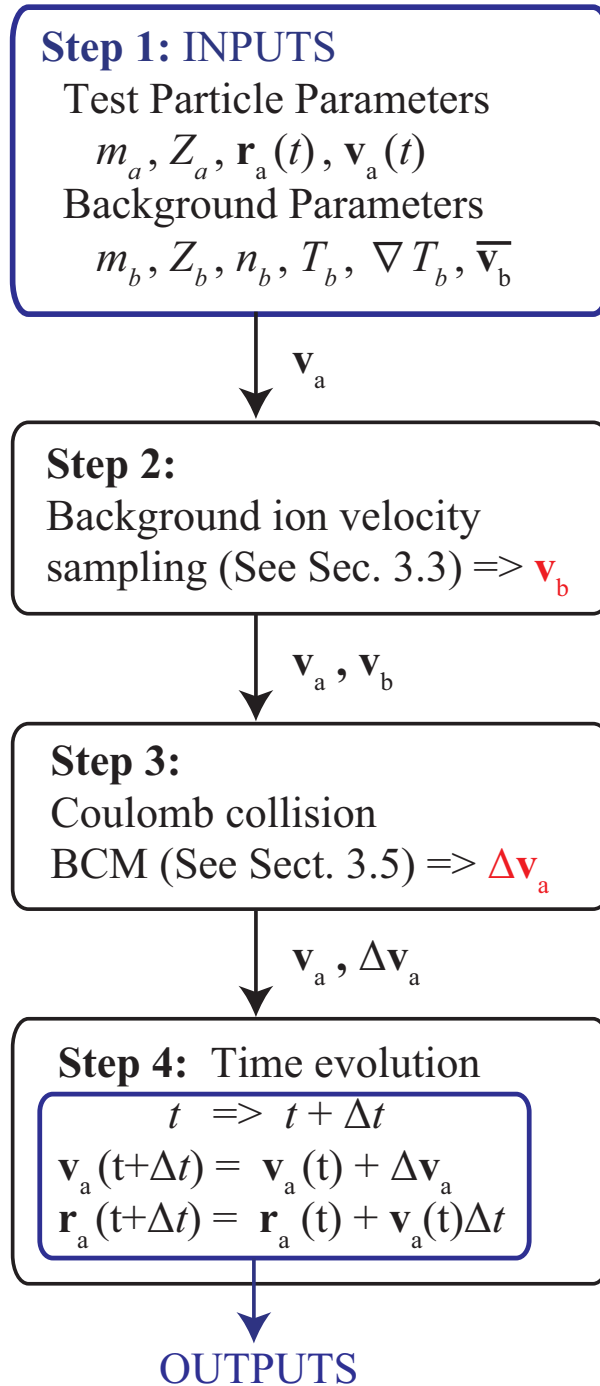


Figure 3.2: Basic procedures of the model. (cited from Ref. [50].)

3.3. RANDOM VELOCITY SAMPLING FROM THE DISTORTED MAXWELLIAN (STEP 2)

For general simulation where we use many test particles, we iterate the basic steps above at every collision event for each test particle.

3.3 Random velocity sampling from the distorted Maxwellian (Step 2)

For the Step 2 in the basic procedures of the model in Fig. 3.2, the numerical random sampling of the background ion velocity from the distorted Maxwellian, is now described. This method plays a key role in our new model.

3.3.1 Preparation: Two coordinate systems for the velocity space

To sample ion velocity easily from the distorted Maxwell distribution in Eq. (3.1), we use two coordinate systems for the velocity space, called ‘‘System I’’ and ‘‘System II’’. Hereinafter, we distinguish variables for Systems I and II by subscripts I and II, respectively. The coordinate System I (X_I, Y_I, Z_I) is the laboratory frame at rest. A temperature gradient ∇T_b is assumed to exist in System I, such as

$$\nabla T_b = |\nabla T_b| \begin{pmatrix} \sin \theta \cos \phi \\ \sin \theta \sin \phi \\ \cos \theta \end{pmatrix}, \quad (3.4)$$

where angles θ and ϕ are defined as in Fig. 3.3. On the other hand, the System II (X_{II}, Y_{II}, Z_{II}) is the coordinate system with the Z_{II} -axis parallel to the temperature gradient, as shown in Fig. 3.4.

A variable transformation from System II to System I is realized by using the matrix $\mathbf{T}^{II \rightarrow I}$,

$$\mathbf{T}^{II \rightarrow I} := \begin{pmatrix} \cos \phi \cos \theta & -\sin \phi & \cos \phi \sin \theta \\ \sin \phi \cos \theta & \cos \phi & \sin \phi \sin \theta \\ -\sin \theta & 0 & \cos \theta \end{pmatrix}. \quad (3.5)$$

As a result, when we have vector \mathbf{v}_{II} in System II, we obtain its expression in System I, \mathbf{v}_I , by taking its product with $\mathbf{T}^{II \rightarrow I}$, $\mathbf{v}_I = \mathbf{T}^{II \rightarrow I} \cdot \mathbf{v}_{II}$.

3.3.2 Distorted Maxwellian expressed in System II

A background velocity \mathbf{v}_I in the laboratory frame consists of a background flow velocity $\overline{\mathbf{v}}_b$ and a random velocity \mathbf{w}_I : $\mathbf{v}_I = \overline{\mathbf{v}}_b + \mathbf{w}_I$. As $\overline{\mathbf{v}}_b$ is a given parameter, we only have to determine \mathbf{w}_I distributed according to the distorted Maxwellian $f_b(\mathbf{w}_I)$ in Eq. (3.1).

3.3. RANDOM VELOCITY SAMPLING FROM THE DISTORTED MAXWELLIAN (STEP 2)

For the sake of computation, rather than choosing a value of \mathbf{w}_I directly from $f_b(\mathbf{w}_I)$ in Eq. (3.1), it is easier to determine its expression, \mathbf{w}_{II} , in System II first. Then we convert \mathbf{w}_{II} into \mathbf{w}_I .

To specify \mathbf{w}_{II} , we use the three parameters as shown in Fig. 3.4: (i) speed w . (ii) inclination angle θ_{II} , measured from the Z_{II} -axis. (iii) rotational angle ϕ_{II} , around the Z_{II} -axis, measured from the X_{II} -axis. Notice that the rotation by the matrix $\mathbf{T}^{II \rightarrow I}$ does not affect the absolute value of \mathbf{w}_I . So we use w in common for the speed of both \mathbf{w}_I and \mathbf{w}_{II} .

Since the Jacobian determinant $|\det \mathbf{T}^{II \rightarrow I}|$ is 1, we obtain the distribution, $f_{b,II}$, of velocity \mathbf{w}_{II} in System II as follows,

$$f_b(\mathbf{w}_I)d\mathbf{w}_I = f_b(\mathbf{T}^{II \rightarrow I} \cdot \mathbf{w}_{II}) \cdot |\det \mathbf{T}^{II \rightarrow I}| d\mathbf{w}_{II} = f_{b,II}(\mathbf{w}_{II})d\mathbf{w}_{II}. \quad (3.6)$$

Hence, from Eq. (3.1),

$$\begin{aligned} f_{b,II}(\mathbf{w}_{II})d\mathbf{w}_{II} &= n_b \left(\frac{m_b}{2\pi T_b} \right)^{\frac{3}{2}} w^2 \sin \theta_{II} \cdot \exp \left(-\frac{m_b w^2}{2T_b} \right) \\ &\times \left[1 + A(T_b) \left(1 - \frac{w^2}{5v_{th,b}^2} \right) \cdot \frac{w}{v_{th,b}} |\nabla T_b| \cos \theta_{II} \right] dw d\theta_{II} d\phi_{II}. \end{aligned} \quad (3.7)$$

The distribution function $f_{b,II}$ can be decomposed into three functions f , g , and h , such that $(f_{b,II}/n_b)d\mathbf{w}_{II} = (fdw)(gd\theta_{II})(hd\phi_{II})$, each of which is defined as

$$f(w)dw = \sqrt{\frac{2}{\pi}} \left(\frac{m_b}{T_b} \right)^{\frac{3}{2}} w^2 \exp \left(-\frac{m_b w^2}{2T_b} \right) dw, \quad (3.8)$$

$$g(w, \theta_{II})d\theta_{II} = \frac{1}{2} \left[1 + A(T_b) \left(1 - \frac{w^2}{5v_{th,b}^2} \right) \cdot \frac{w}{v_{th,b}} |\nabla T_b| \cos \theta_{II} \right] \sin \theta_{II} d\theta_{II}, \quad (3.9)$$

$$h(\phi_{II})d\phi_{II} = d\phi_{II}/2\pi. \quad (3.10)$$

The functions f , g , and h are the probability density functions associated with the random variables w , θ_{II} , and ϕ_{II} .

3.3.3 Sampling of random variable w

In our numerical model, the speed of background ion w , is first chosen randomly from the probability density function $f(w)$ in Eq. (3.8). This density function is, in fact, the same as that for the speed of the Maxwell distribution with temperature T_b . We can generate w as follows:

1. Let R be a uniform random number over the interval $[0, 1]$. Hereinafter, it is written in the manner $R \sim U[0, 1]$. We generate four uniform random numbers R_k ($k = 1, 2, 3, 4$).

3.3. RANDOM VELOCITY SAMPLING FROM THE DISTORTED MAXWELLIAN (STEP 2)

- Then, by using the Box-Muller transform [39], we determine the values of three independent random numbers w_x , w_y , and w_z , which have a Gaussian distribution with mean zero and standard deviation $v_{th,b} = \sqrt{T_b/m_b}$,

$$w_x = v_{th,b} \times \sqrt{-2 \ln R_1} \cos(2\pi R_2),$$

$$w_y = v_{th,b} \times \sqrt{-2 \ln R_1} \sin(2\pi R_2),$$

$$w_z = v_{th,b} \times \sqrt{-2 \ln R_3} \cos(2\pi R_4).$$

- The random speed w is then obtained as $w = \sqrt{w_x^2 + w_y^2 + w_z^2}$.

3.3.4 Sampling of random variable θ_{II}

The inclination angle θ_{II} between \mathbf{w}_{II} and ∇T_b is next given from the distribution $g(w, \theta_{II})$ in Eq. (3.9). The correlation between w and θ_{II} is taken into account. By introducing the function α

$$\alpha(w, T_b, \nabla T_b) := A(T_b) \left(1 - \frac{w^2}{5v_{th,b}^2} \right) \cdot \frac{w}{v_{th,b}} |\nabla T_b|, \quad (3.11)$$

we can rewrite $g(w, \theta_{II})$ from Eq. (3.9) in a simpler form

$$g(w, \theta_{II}) d\theta_{II} = \frac{1}{2} [1 + \alpha \cos \theta_{II}] \sin \theta_{II} d\theta_{II}. \quad (3.12)$$

The angle θ_{II} is sampled from Eq. (3.12) by the following manner:

- To fix the distribution $g(w, \theta_{II})$, substitute into Eq. (3.11) the value of the random speed w' , which is already chosen in the previous process (Sec. 3.3.3).
- According to the value of α , the variable θ_{II} is given by using a random number $R \sim U[0, 1]$, such as

- (a) If $\alpha = 0$: $\cos \theta_{II} = 2R - 1$.

- (b) If $0 < \alpha \leq 1$: $\cos \theta_{II} = \left\{ \sqrt{4\alpha R + (1 - \alpha)^2} - 1 \right\} / \alpha$.

- (c) If $\alpha > 1$: The distribution function $g(w', \theta_{II})$ becomes negative at certain angle θ_{II} . In order to avoid it, we take the limit of $\alpha \rightarrow 1$. Thus, $\cos \theta_{II} = 2\sqrt{R} - 1$.

- (d) If $-1 \leq \alpha < 0$: $\cos \theta_{II} = \left\{ \sqrt{-4\alpha R + (1 + \alpha)^2} - 1 \right\} / \alpha$.

- (e) If $\alpha < -1$: The function $g(w', \theta_{II})$ becomes negative at certain angle θ_{II} . In order to avoid it, we take the limit of $\alpha \rightarrow -1$. Thus, $\cos \theta_{II} = 1 - 2\sqrt{R}$.

Thus sampled θ_{II} obeys the distribution of Eq.(3.12) (see Appendix).

3.4. APPLICABLE CONDITION FOR THE MODEL

3.3.5 Sampling of random variable ϕ_{II}

From distribution function $h(\phi_{\text{II}})$ in Eq.(3.10), the rotational angle ϕ_{II} is given by $\phi_{\text{II}} = 2\pi R$, with $R \sim U[0, 1]$.

3.3.6 Background ion velocity, \mathbf{v}_{I}

By using three variables $(w, \theta_{\text{II}}, \phi_{\text{II}})$, the background ion velocity \mathbf{w}_{II} is expressed as

$$\mathbf{w}_{\text{II}} = w \begin{pmatrix} \sin \theta_{\text{II}} \cos \phi_{\text{II}} \\ \sin \theta_{\text{II}} \sin \phi_{\text{II}} \\ \cos \theta_{\text{II}} \end{pmatrix}. \quad (3.13)$$

The random velocity \mathbf{w}_{I} in System I (the laboratory frame) is obtained by $\mathbf{w}_{\text{I}} = \mathbf{T}^{\text{II} \rightarrow \text{I}} \cdot \mathbf{w}_{\text{II}}$. Adding the background flow velocity $\bar{\mathbf{v}}_b$, we numerically obtain the background ion velocity $\mathbf{v}_{\text{I}} (= \mathbf{w}_{\text{I}} + \bar{\mathbf{v}}_b)$, which follows the distorted Maxwell distribution in Eq. (3.1).

3.4 Applicable Condition for the Model

The distorted Maxwellian in Eq. (3.1) is in the form $f = f_0 + f_1$, consisting of the Maxwell distribution f_0 and a correction term f_1 . The correction term f_1 should be small enough when compared to the Maxwellian term f_0 . By approximating the random speed w by the thermal speed $v_{th,b}$, the ratio $|f_1/f_0|$ is estimated as: $|f_1/f_0| \sim \lambda_{\text{MFP}}/L_T$, where $L_T := T_b/|\nabla T_b|$. Our model is applicable under the condition: $\lambda_{\text{MFP}}/L_T \ll 1$.

3.4. APPLICABLE CONDITION FOR THE MODEL

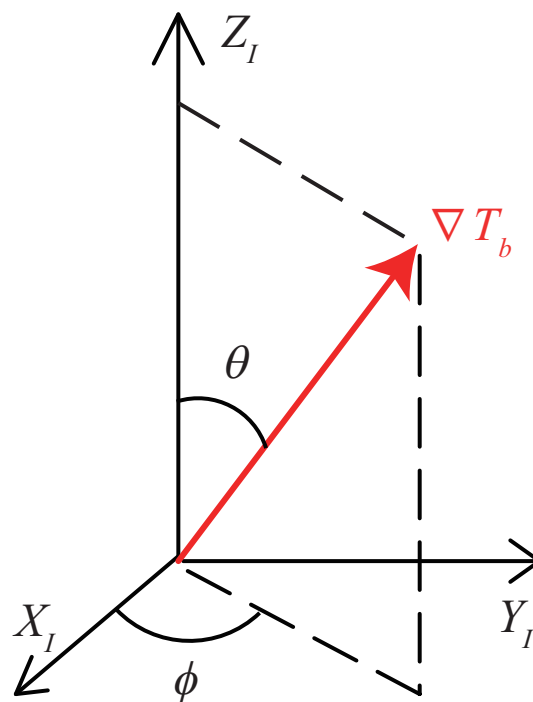


Figure 3.3: System I. (cited from Ref. [50].)

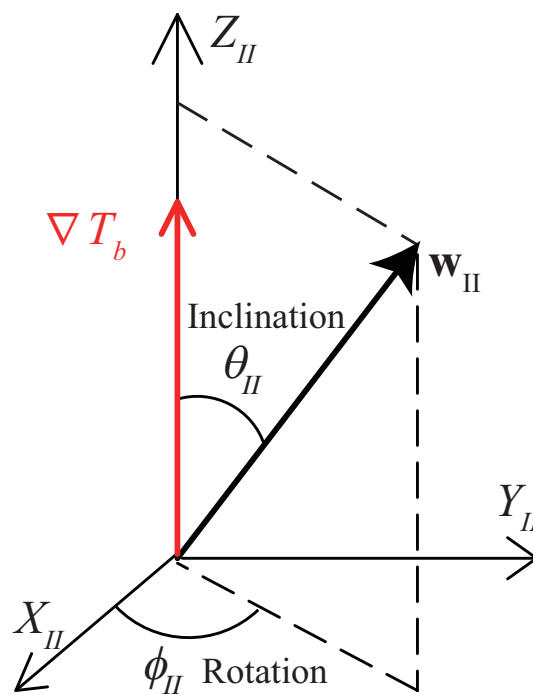


Figure 3.4: System II. (cited from Ref. [50].)

3.5 Monte Carlo Binary Collision Model (Step 3)

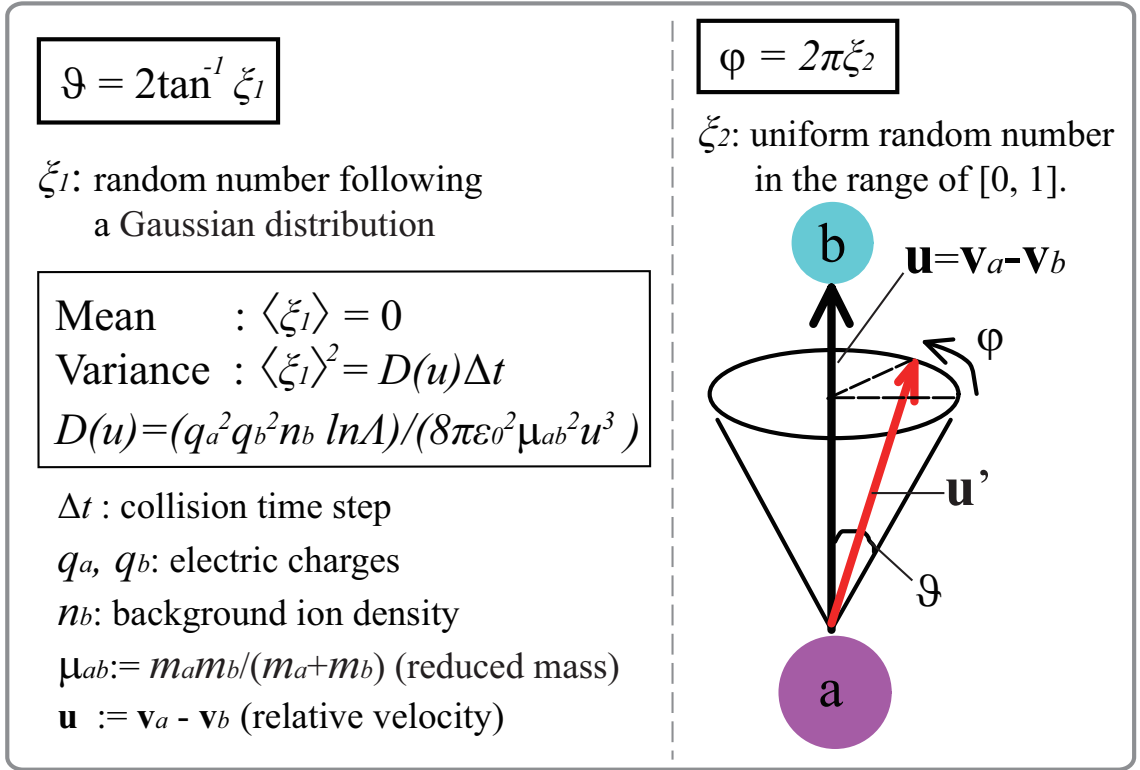


Figure 3.5: Monte Carlo Binary Collision model. (cited from Ref. [50].)

In order to simulate Coulomb collision between the test particle and the background ion chosen in Sec. 3.3, we use the Monte Carlo Binary Collision Model (BCM) [32]. From the relative velocity between the colliding two particles, the BCM calculates the random velocity change $\Delta \mathbf{v}^{\text{Coll}}$ by the collision.

Suppose that we have two particles (species a and b). They are moving, respectively, with the velocity \mathbf{v}_a and \mathbf{v}_b , and they are to collide with each other. The collision is simulated by the following procedures.

1. The two particles collide with relative velocity $\mathbf{u} = \mathbf{v}_a - \mathbf{v}_b$. At the collision, two scattering angles, ϑ and φ (as shown in Fig. 3.5) are calculated. The angle ϑ is modeled as $\vartheta = 2 \tan^{-1} \xi_1$, where ξ_1 is a random variable following a Gaussian distribution with the mean $\langle \xi_1 \rangle$ and the variance $\langle \xi_1^2 \rangle$, such as

$$\langle \xi_1 \rangle = 0, \quad (3.14)$$

$$\langle \xi_1^2 \rangle = D(u) \Delta t, \quad (3.15)$$

$$D(u) = q_a^2 q_b^2 n_b (\ln \Lambda) / (8 \pi \epsilon_0^2 \mu_{ab}^2 u^3). \quad (3.16)$$

3.5. MONTE CARLO BINARY COLLISION MODEL (STEP 3)

The other rotation angle φ is obtained by $\varphi = 2\pi\xi_2$, where ξ_2 is a uniform random number in the interval $[0, 1]$.

2. From the scattering angles ϑ and φ , the velocity change caused by the collision, $\Delta\mathbf{v}_j$ ($j = a$ and b), is calculated for the two particles. Detail of the calculations are described by Takizuka and Abe [32]. The new velocities \mathbf{v}'_j are then $\mathbf{v}'_j = \mathbf{v}_j + \Delta\mathbf{v}_j$.

There exists a limitation of collision time step Δt such as

$$\langle \xi_1^2 \rangle = D(u)\Delta t \ll 1, \quad (3.17)$$

because of the fact that the Coulomb scattering angle θ (or ξ_1) is essentially quite small. In order to find an appropriate time step Δt , we approximate the relative velocity u in $D(u)$ by the thermal speed of the faster particle.

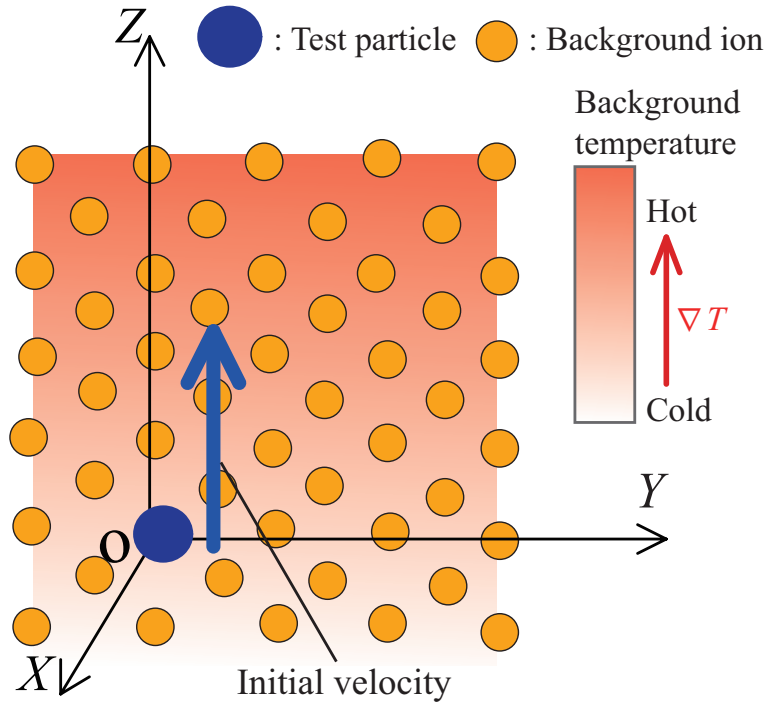


Figure 3.6: Configuration of the test simulations. (cited from Ref. [50].)

3.6 Test simulations

3.6.1 Simulation parameters

Figure 3.6 shows the model geometry of the test simulations. Cartesian coordinates (X, Y, Z) are used to describe the real space of the laboratory frame.

The numerical parameters for simulation are summarized in Table 3.1. The simulation starts with the injection of $N = 5 \times 10^4$ test particles from the origin $(0, 0, 0)$. The test particle species is tungsten ion W^{3+} ($Z_a = 3$), and all of them are injected in the positive Z -direction, with the initial speed corresponding to the kinetic energy of 50 eV (i.e., $\mathbf{v}_a(t=0) := \mathbf{v}_0 = \sqrt{3E_0/m_a} \mathbf{e}_Z$, where m_a is the mass of the W^{3+} ion, $E_0 = 50$ eV, and \mathbf{e}_Z is the unit vector in the Z -direction).

The background plasma is assumed to be composed of hydrogen ions H^+ ($Z_b = 1$). The electrons are not taken into account. The background flow velocity $\bar{\mathbf{v}}_b$ is set to $\mathbf{0}$, the number density of background ions n_b is 10^{20} m^{-3} . The background temperature $T_b(\mathbf{r} = \mathbf{0})$ is 50 eV. The temperature gradient ∇T_b is along the Z -direction or X -direction in the following simulations. These parameters are of a typical divertor plasma in present tokamaks.

We take the simulation time step as $\Delta t = 10^{-3}/D(v_{\text{th},b})$. To estimate $D(u)$ in Eq. (3.16), we have approximated the relative velocity u between two colliding particles, by the thermal speed of background ion $v_{\text{th},b}$ because $v_{\text{th},b} \gg v_0$.

3.6. TEST SIMULATIONS

Table 3.1: Numerical Parameters for the reference case. (cited from Ref. [50].)

Test particle species		W^{3+}
Initial test particle velocity, $\mathbf{v}_a(t=0)$	$8.84 \times 10^3 \text{ ms}^{-1} \mathbf{e}_Z$	(50 eV)
Normalized test particle velocity, $\tilde{\mathbf{v}}_a(t=0)$		$0.13 \mathbf{e}_Z$
No. of test particles, N		5×10^4
Background plasma ion		H^+
Number density of background ions, n_b		10^{20} m^{-3}
Temperature at the origin, $T_b(\mathbf{0})$		50 eV
Temperature gradient, ∇T_b		depends on each case
Coulomb logarithm, $\ln \Lambda$		15
$1/D(v_{\text{th},b})$		$2.03 \times 10^{-7} \text{ s}$
Collision time step, Δt		$1/D(v_{\text{th},b}) \times 10^{-3} \text{ s}$
Slowing-down time, τ_s		$7.10 \times 10^{-5} \text{ s}$

3.6.2 Reference simulation with $\nabla T_b = 0$

Prior to examining the thermal force, we perform a test calculation without temperature gradient $\nabla T = 0$. Only the frictional force is examined as a basis for the following test simulations.

In this case, the initial test particle velocity is oriented in the $+Z$ -direction and there is no temperature gradient. According to Eqs. (2.58) and (2.59), i.e. only the frictional force acts on the test particles in the negative Z -direction. Net collisional force does not act in the X and Y -direction.

Figures 3.7(a) and 3.7(b) show the time evolution of the average velocity $\overline{\mathbf{v}}_a(t)$ of test particles. The average velocity $\overline{\mathbf{v}}_a(t)$ is defined by the ensemble average over the test particles at each time step,

$$\overline{\mathbf{v}}_a(t) := \frac{1}{N} \sum_{i=1}^N \mathbf{v}_{a,i}(t). \quad (3.18)$$

The X - and Z - component, $\overline{v_{a,X}}(t)$ and $\overline{v_{a,Z}}(t)$ are shown, respectively, in Figs. 3.7(a) and 3.7(b). Their theoretical value is expressed by the solid line. The rate of change $d\mathbf{v}_a/dt$ (i.e. $= \mathbf{F}/m_a$) is calculated from the formula of collisional force Eq. (2.58), with the initial test particle velocity ($\mathbf{v}_a = \mathbf{v}_0$). The ordinate of the figures is the averaged speed normalized to the initial speed v_0 , and their abscissa is the time normalized to the slowing-down time τ_s , which is a characteristic time for the test particle to slow down due to collisions, defined by [13]

$$\tau_s := \frac{1}{\left(1 + \frac{m_a}{m_b}\right) \mu(x)} \frac{4\pi\epsilon_0^2 m_a^2 v_0^3}{q_a^2 q_b^2 n_b \ln \Lambda}, \quad (3.19)$$

3.6. TEST SIMULATIONS

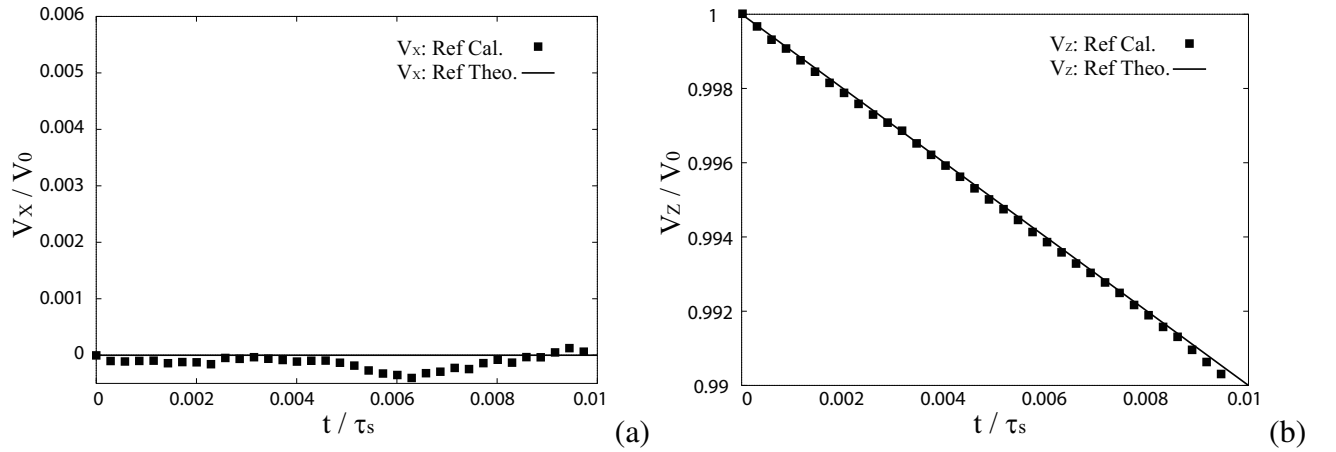


Figure 3.7: Time evolution of the average velocity $\overline{v_a}(t)$ (Eq. (3.18)): (a) X -component $\overline{v_X}(t)$, (b) Z -component $\overline{v_Z}(t)$. The velocity is normalized to the initial speed v_0 , and the time is normalized to the slowing-down time τ_s . (cited from Ref. [50].)

where $x := m_b v_0^2 / 2T_b$, and $\mu(x) := (2/\sqrt{\pi}) \int_0^x \exp(-\xi) \sqrt{\xi} d\xi$.

As shown in Fig. 3.7(a), the numerical results of $\overline{v_{a,X}}(t)$ agree well with its theoretical value. The $\overline{v_{a,X}}(t)$ remains almost zero throughout the simulated period $0 \leq t \leq 0.01\tau_s$, meaning that no net collisional force acts in the X -direction. Although the result is not shown here, the same results have been obtained for the Y -component ($\overline{v_{a,Y}}(t) \approx 0$).

On the other hand, the Z -component $\overline{v_{a,Z}}(t)$ is clearly decreasing as shown in Fig. 3.7(b). The slope agrees well with the theoretical value. It means that the test particles have received a slowing-down collisional force whose magnitude is the same as the frictional force deduced from Eq. (2.58).

Above comparisons between the numerical and theoretical results show that our numerical model simulates the frictional force correctly.

3.6.3 Test simulations with finite test simulation ∇T_b

Conditions

After validating the frictional force in the reference case, we have performed a series of test simulations on the thermal force, under various conditions. As summarized in Section 2.3.1, the thermal force can change widely in magnitude and direction, depending on the temperature gradient and test particle velocity. The calculation conditions are summarized in Table 3.2 and Fig. 3.8. The remaining parameters are the same as those of the reference case (Table 3.1). These test conditions are within the applicable condition of the model in Sec. 3.4. Each test condition is described below.

Case 1: $\mathbf{F}^{\nabla T} // \mathbf{v}_a$. The temperature gradient is set to be in the Z -direction, parallel to the initial test particle velocity. Two different magnitudes are supposed, i.e. 3 eV/m (Case 1-1), 5 eV/m (Case

3.6. TEST SIMULATIONS

Table 3.2: Test conditions. (cited from Ref. [50].)

		∇T_X [eV/m]	∇T_Y [eV/m]	∇T_Z [eV/m]	$ \tilde{\mathbf{v}}_a $ -	n_b [m ⁻³]
Case 1	1-1	0	0	3	0.13	1×10^{20}
	1-2	0	0	5	0.13	1×10^{20}
Case 2	2-1	3	0	0	0.13	1×10^{20}
	2-2	5	0	0	0.13	1×10^{20}
Case 3	3-1	0	0	0	1.8	1×10^{20}
	3-2	0	0	10	1.8	1×10^{20}
Case 4	4-1	0	0	5	0.13	0.85×10^{20}
	4-2	0	0	5	0.13	2.0×10^{20}

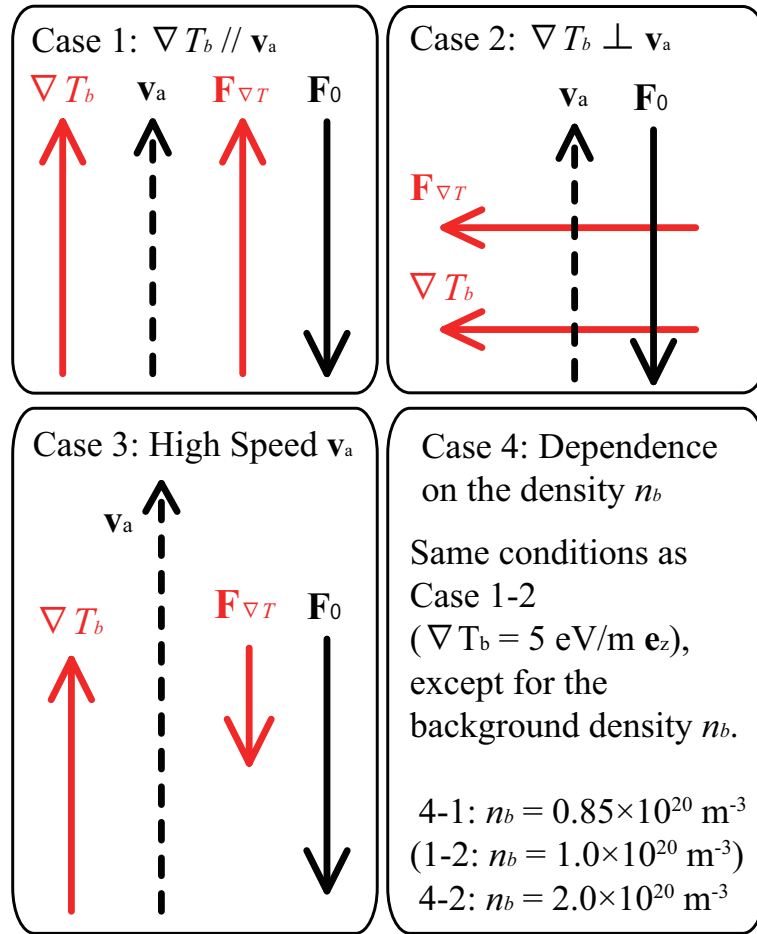


Figure 3.8: Relationships between temperature gradient and the initial velocity of test particle for each case. (cited from Ref. [50].)

3.6. TEST SIMULATIONS

1-2). The test particles move sufficiently slowly ($|\tilde{v}_a| \ll 1$). The thermal force should act in the Z -direction as discussed in Sec. 2.3.1 (characteristic feature 2: $\mathbf{F}^{\nabla T} // \nabla T_b$). We will also check if the magnitude of the thermal force is proportional to that of the temperature gradient (characteristic feature 1: $|\mathbf{F}^{\nabla T}| \propto |\nabla T_b|$).

Case 2: $\mathbf{F}^{\nabla T} \perp \mathbf{v}_a$. Differently from Case 1, the temperature gradient is set to be in the X -direction, perpendicular to the initial test particle velocity. The thermal force should act in the X -direction. We use two different magnitudes of temperature gradient: 3 eV/m (Case 2-1), 5 eV/m (Case 2-2), in order to check the proportionality of the thermal force ($|\mathbf{F}_{\nabla T}| \propto |\nabla T_b|$).

Case 3: Thermal force on high-speed test particles. In Case 1 and 2, we have chosen the initial test particle velocity slower than the background thermal speed ($|\tilde{v}_a| \ll 1$). For Case 3, we examine the thermal force on faster test particles ($|\tilde{v}_a| \geq 1$). The initial test particle velocity is set to be $\mathbf{v}_0 = \sqrt{3E_a/m_a} \mathbf{e}_Z$, with $E_a = 10,000$ eV ($|\tilde{v}_a| = 1.8$). At first, we have performed a calculation without ∇T (Case 3-1). Next, we have given a temperature gradient in the Z -direction with magnitude 10 eV/m (Case 3-2). Under this condition, the thermal force should act in the opposite direction to the temperature gradient (characteristic feature 3. in Sec. 2.3.1).

Case 4: Dependence on the number density of background plasma. For this case, we use the same condition as Case 1-2, except for the number density of background plasma n_b . Case 4 examines whether the simulated thermal force is independent of the background number density (characteristic feature 4 in Sec. 2.3.1).

Results of Case 1

We have a temperature gradient in the Z -direction: $\nabla T = 3$ eV/m $\cdot \mathbf{e}_Z$ (Case 1-1), 5 eV/m $\cdot \mathbf{e}_Z$ (Case 1-2), and the other parameters remain unchanged from Table 3.1. According to Eqs. (2.58) and (2.59), the thermal force is generated in the ($+Z$)-direction while the frictional force is along ($-Z$)-direction. Forces in the X - and Y -direction are null.

Figure 3.9 shows the velocity relaxation in the Z -direction of Case 1-1 and 1-2. The squares show the simulated average velocity $\overline{v_{a,Z}(t)}$ in Case 1-1, and the circles are the results of Case 1-2. The solid line and the dashed line represent the theoretical values calculated from Eqs. (2.58) and (2.59), respectively, for Case 1-1 and 1-2. As a reference, the velocity simulated in the previous reference case without thermal force, is plotted by the triangles.

The results of both Case 1-1 (squares) and 1-2 (circles) agree well with their theoretical values. It should be noted that their slopes are less steep than that of the reference case (triangles). The thermal force has acted in the direction of temperature gradient, i.e. in the positive Z -direction, and reduced the total collisional force on the test particles. The slope of Case 1-2 is even less steep than that of

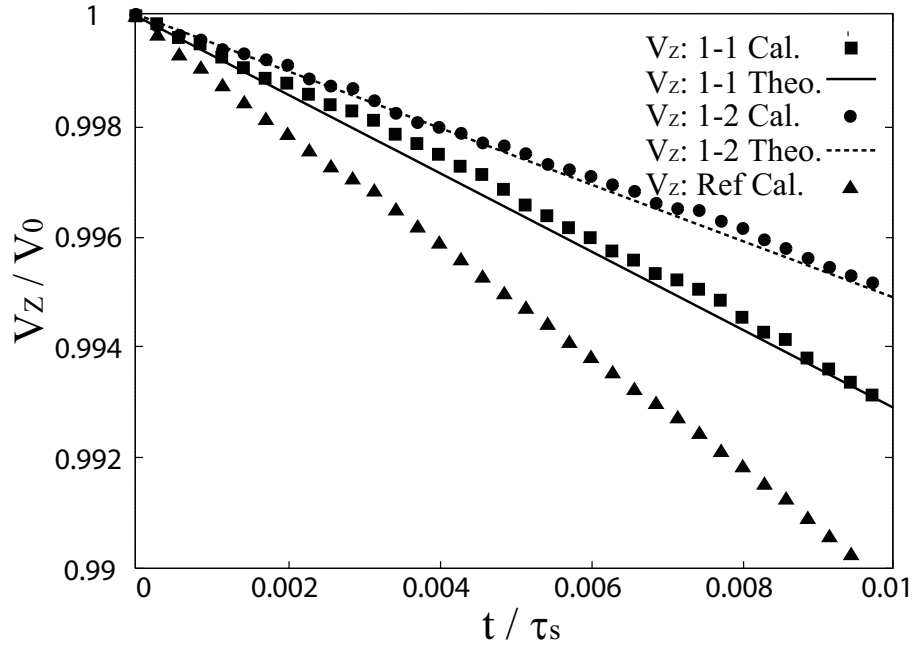


Figure 3.9: Time evolution of the average velocity $\overline{v_z}(t)$ for Case 1-1 and 1-2. (cited from Ref. [50].)

Case 1-1. It suggests that simulated thermal force has become greater, as its theoretical value expects, proportionally to the magnitude of temperature gradient which has been raised from Case 1-1 to 1-2.

From above results, the thermal force is correctly simulated both in direction and in magnitude ($\mathbf{F}^{\nabla T} // \nabla T_b$, $|\mathbf{F}^{\nabla T}| \propto |\nabla T_b|$), under a parallel temperature gradient ($\nabla T_b // \mathbf{v}_a$).

Results of Case 2

In this case, the temperature gradients are taken in the X -direction: $\nabla T = 3 \text{ eV/m} \cdot \mathbf{e}_X$ (Case 2-1), $5 \text{ eV/m} \cdot \mathbf{e}_X$ (Case 2-2), and the other parameters are the same as those in Table 3.1.

Under perpendicular temperature gradients ($\nabla T_b \perp \mathbf{v}_a$), as expected from Eqs. (2.58) and (2.59), the thermal force acts in the X -direction and does not affect the frictional force in the Z -direction. Contribution of the thermal force in the X -direction leads to acceleration of test particles toward the positive X -direction. So we focus on the X -component of the velocity $\overline{v_{a,X}}(t)$ to examine the thermal force².

Figure 3.10 shows the time evolution of simulated average velocity in the X -direction $\overline{v_{a,X}}(t)$ by squares and circles, respectively, for Case 2-1 and 2-2. The solid and dashed line denote the expected acceleration deduced from the theoretical thermal force $\mathbf{F}_{\mathbf{B}=0}^{\nabla T}$ from Eq. (2.59), respectively, for Case 2-1 and 2-2. As a reference, the average velocity $\overline{v_{a,X}}(t)$ simulated in the reference case is plotted by the triangles.

²Concerning the Z -component of velocity $\overline{v_{a,Z}}(t)$, the same result as Fig. 3.7(b) of the reference case has been obtained (not shown). The frictional force in the Z -direction is correctly simulated.

3.6. TEST SIMULATIONS

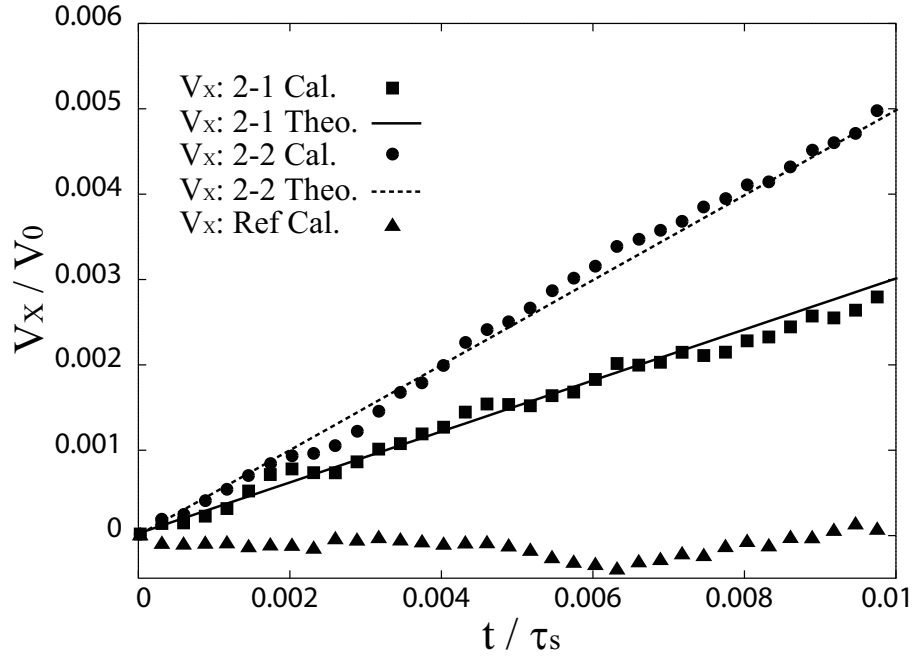


Figure 3.10: Time evolution of the average velocity $\overline{v_X}(t)$ for Case 2-1 and 2-2. (cited from Ref. [50].)

The calculated results are in good agreement with the theoretical values. In addition, the result of Case 2-2 has a slope greater than that of Case 2-1. The thermal force in Case 2-2 (with greater ∇T) is stronger than in Case 2-1. The thermal force is correctly simulated (i.e. $\mathbf{F}^{\nabla T} / |\nabla T_b|$, $|\mathbf{F}^{\nabla T}| \propto |\nabla T_b|$) by our model under a perpendicular temperature gradient ($\nabla T_b \perp \mathbf{v}_a$).

Results of Case 3

Characteristic feature 3, discussed in Sec. 2.3.1, is to be examined below. We have raised the initial velocity of test particles up to $\tilde{v}_0 = 1.8e_Z$, and have simulated the velocity relaxation without ∇T in Case 3-1 at first. Then, we have introduced a temperature gradient $\nabla T = 10 \text{ eV/m} \cdot e_Z$ in Case 3-2 in order to see the effect of thermal force on fast test particles. Since the frictional and the thermal force both act in the Z -direction in this case, we examine the Z -component of the average velocity $\overline{v_Z}(t)$.

Numerical results $\overline{v_{a,Z}}(t)$ are shown in Fig. 3.11 by squares and circles, respectively, for Case 3-1 and 3-2. Their theoretical values calculated from Eqs. (2.58) and (2.59) are expressed by solid and dashed line, respectively, for Case 3-1 and 3-2.

Compared with the result of Case 3-1 without ∇T , the result of Case 3-2, with ∇T , shows a steeper slope. It means that the thermal force occurred in the negative Z -direction, enhancing the total collisional force. Differently from Case 1, the direction of the thermal force is in the opposite direction to the temperature gradient. It is consistent with the theoretical characteristic 3 of the thermal force. From good agreement of the numerical results with their theoretical value, we confirm that the

3.6. TEST SIMULATIONS

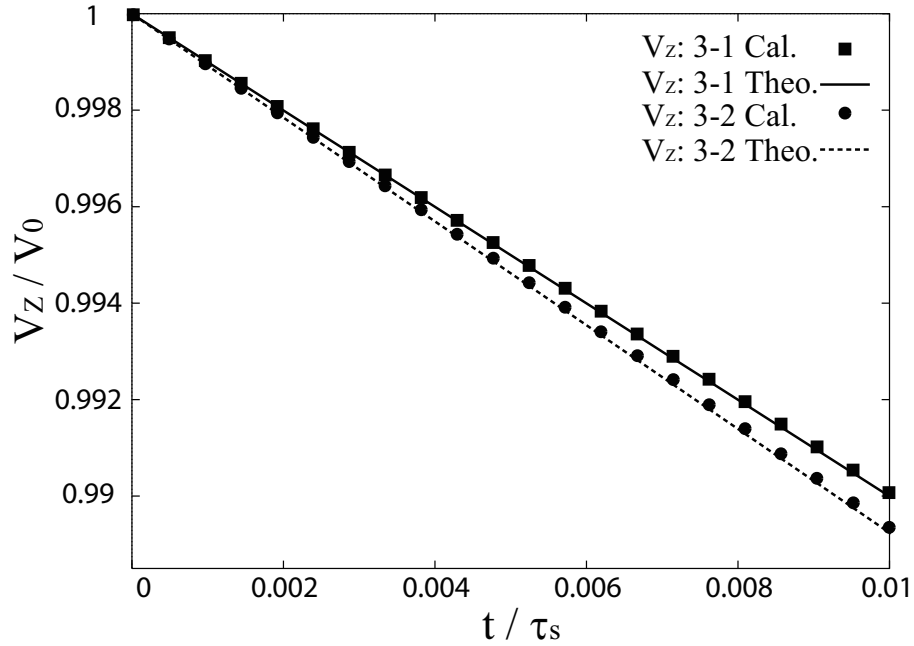


Figure 3.11: Time evolution of the average velocity $\overline{v_Z}(t)$ for Case 3-1 and 3-2. (cited from Ref. [50].)

thermal force on fast test particles is simulated accurately by our model.

Results of Case 4

In Case 4, we examine the dependence of the thermal force on the number density of background plasma ions n_b . By using the same parameters as Case 1-2, we change only the value of n_b as shown in Table 3.2.

Simulated average velocity $\overline{v_{a,Z}}(t)$ are presented in Fig. 3.12 by squares and circles, respectively, for Case 4-1 and 4-2. Theoretical values of Eqs. (2.58) and (2.59) are also presented by solid and dashed line, respectively, for Case 4-1 and 4-2. As a reference, the result of Case 1-2 is plotted by triangles.

Good agreement between the numerical results and the theoretical values are seen for both Case 4-1 and 4-2 in Fig. 3.12. It confirms that the model simulates the frictional force and the thermal force, with their correct dependence on the background number density (i.e. $|\mathbf{F}_0| \propto n_b$, $|\mathbf{F}^{\nabla T}|$ is independent of n_b).

Quantitative discussion on simulation results

In above sections, we have seen that the thermal force is simulated qualitatively well. In the present section, we examine the simulation results quantitatively. The results are summarized in Table 3.3. To obtain these results, we have performed 10 times of calculation for each test case (from Case 1-1

3.6. TEST SIMULATIONS

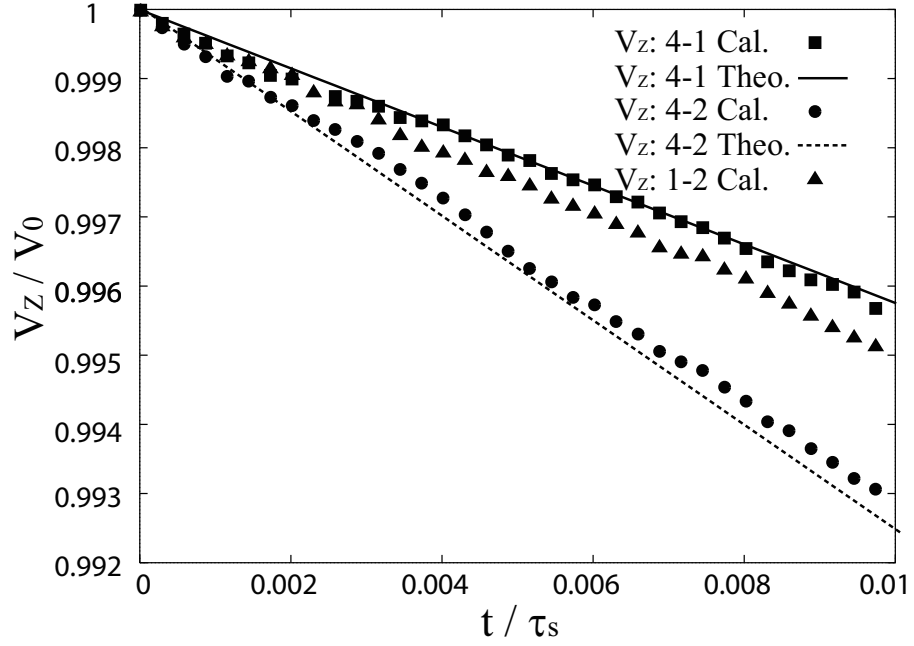


Figure 3.12: Time evolution of the average velocity $\bar{v}_z(t)$ for Case 4-1 and 4-2 (and 1-2). (cited from Ref. [50].)

Table 3.3: Quantitative comparison of collisional force. (cited from Ref. [50].)

	Simulated $\langle \mathbf{F} \rangle$ [$\times 10^{-17}$ N]	Theoretical \mathbf{F} [$\times 10^{-17}$ N]
Ref.: F_Z	-3.72 (± 0.065)	-3.83
Ref.: F_X	-0.026 (± 0.075)	0
1-1: F_Z	-2.58 (± 0.082)	-2.70
1-2: F_Z	-1.855 (± 0.081)	-1.95
2-1: F_X	1.22 (± 0.088)	1.14
2-2: F_X	1.87 (± 0.11)	1.91
3-1: F_Z	-22.3 (± 0.03)	-22.5
3-2: F_Z	-23.9 (± 0.03)	-24.2
4-1: F_Z	-1.33 (± 0.073)	-1.38
4-2: F_Z	-5.61 (± 0.155)	-5.78

3.6. TEST SIMULATIONS

Table 3.4: Estimation of simulated thermal force. (cited from Ref. [50].)

	$\langle \mathbf{F}^{\nabla T} \rangle$ [$\times 10^{-17}$ N]	$\mathbf{F}^{\nabla T}$ [$\times 10^{-17}$ N]	$\langle \mathbf{F}^{\nabla T} \rangle / \mathbf{F}^{\nabla T}$
1-1: $F_{\nabla T,Z}$	1.14	1.125	1.015
1-2: $F_{\nabla T,Z}$	1.87	1.875	0.997
2-1: $F_{\nabla T,X}$	1.24	1.14	1.09
2-2: $F_{\nabla T,X}$	1.89	1.91	0.99
3-2: $F_{\nabla T,Z}$	-1.575	-1.7	0.93
4-1: $F_{\nabla T,Z}$	1.81	1.875	0.96
4-2: $F_{\nabla T,Z}$	1.78	1.875	0.95

to Case 4-2) under the same condition but with different series of random numbers. Then, the rate of velocity change of test particles $d\bar{v}_a/dt$ has been calculated by using the least-square method. Finally, we have obtained the average value $\langle \mathbf{F} \rangle$ of the simulated collisional force over 10 runs, together with its statistical error $\pm \sqrt{\langle (F - \langle F \rangle)^2 \rangle}$ which is also presented in the parenthesis in Table 3.3. The theoretical value of \mathbf{F} from Eqs. (2.58) and (2.59) are compared with the simulation results in Table 3.3.

Unfortunately, it is difficult to directly separate the numerical results $\langle \mathbf{F} \rangle$ in Table 3.3 into the thermal force part and the frictional force part. However, we can still estimate the simulated thermal force $\langle \mathbf{F}^{\nabla T} \rangle$ by the following manner: $\langle \mathbf{F}^{\nabla T} \rangle := \langle \mathbf{F} \rangle - \langle \mathbf{F}_0 \rangle$, where we assume $\langle \mathbf{F}_0 \rangle = \langle \mathbf{F} \rangle_{\nabla T=0}$, i.e. the frictional force is supposed to be the collisional force without ∇T . The $\langle \mathbf{F} \rangle_{\nabla T=0}$ has been newly calculated for each case, and the results of $\langle \mathbf{F}^{\nabla T} \rangle$ are presented in Table 3.4. The ratio between estimated $\langle \mathbf{F}^{\nabla T} \rangle$ and its theoretical value $\mathbf{F}^{\nabla T}$ from Eq. (2.59) are also given in Table 3.4.

It is clearly confirmed from Table 3.4 that our model is able to simulate the thermal force accurately in the quantitative sense, within the relative error of 10% under actual test simulation conditions (Tables 3.1 and 3.2). It is of course possible to reduce further the statistical error by increasing the number of test particles. The choice, however, depends on the trade-off between the calculation cost and required accuracy of each problem to be solved.

3.7 Summary of Chapter 3

A new numerical model of the thermal force, based on the Monte Carlo Binary Collision model (BCM), has been developed. This model can be applied for the transport simulation of test ions in a plasma without magnetic field. The model consists of two main procedures: (i) choosing a background plasma ion velocity from a distorted Maxwellian distribution under the temperature gradient, and (ii) calculating a Coulomb collision between a test particle and the above chosen ion by using the BCM.

To confirm the validity of the model, we have performed test simulations for various conditions about background temperature gradients and initial velocities of test particle. The time rate of change $d\bar{v}/dt$ of the test particle's average velocity has been compared with its theoretical value calculated from the analytical formulae of the frictional force and the thermal force. The comparisons have shown good agreements for all the test cases. Our new model is able to simulate the thermal force correctly, reproducing the important characteristic features listed in Sec. 2.3.1, i.e. dependences on the temperature gradient, on the test particle velocity, and on the number density of background plasma.

The numerical method proposed in this chapter will be extended to the case of magnetized plasma in the next chapter.

Chapter 4

Extended numerical model of thermal force based on Monte Carlo Binary Collision model in magnetized plasma

A numerical model of thermal force extended to magnetized background plasma is described in this chapter. Figure 4.1 shows the basic procedure to calculate one collision event of a test particle. They are basically the same as those in Chapter 3 (also in Ref. [50]), but now we use an extended distorted Maxwellian and have added the step 5, Buneman-Boris method [43], to simulate the Larmor gyration motion of test particles in the presence of magnetic field.

4.1 Algorithm of the model

Our model consists of the following steps as summarized in Fig. 4.1:

Step 1. Parameters of the test particle and those of the background plasma are specified. The mass m_a , charge state Z_a , present position $\mathbf{r}_a(t)$, and velocity $\mathbf{v}_a(t)$, of the test particle are input parameters. For the background plasma ion, likewise, the mass m_b , charge state Z_b , number density n_b , temperature $T_b(\mathbf{r}_a)$, temperature gradient ∇T_b , and flow velocity $\bar{\mathbf{v}}_b$ are given. The magnetic field \mathbf{B} has to be also specified.

Step 2. The heat flux density \mathbf{q} of background plasma ions is calculated by considering the magnetic field \mathbf{B} . (Sec. 4.2.1)

Step 3. Velocity of a background plasma ion \mathbf{v}_b is randomly chosen from the distorted Maxwellian distribution in Eq. (2.50 or 4.6). (Sec. 4.2)

4.1. ALGORITHM OF THE MODEL

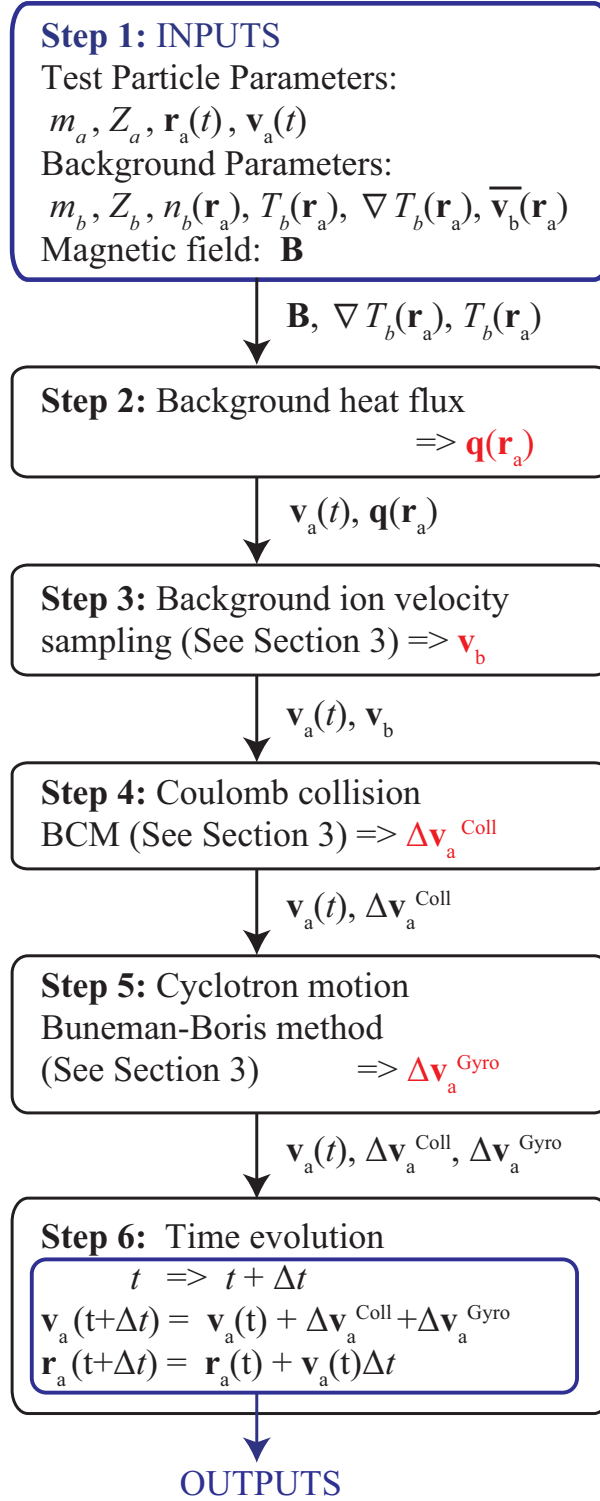


Figure 4.1: Basic flowchart of the model. (cited from Ref. [30].)

4.2. RANDOM VELOCITY SAMPLING FROM DISTORTED MAXWELLIAN (STEP 3)

Step 4. The velocity change $\Delta \mathbf{v}^{\text{Coll}}$ of the test particle due to Coulomb collision with the chosen background ion is calculated by the Monte Carlo Binary Collision Model (BCM) [32]. (Sec. 4.3)

Step 5. Larmor gyro motion of the test particle is integrated. Velocity change $\Delta \mathbf{v}^{\text{Gyro}}$ due to the Lorentz force is calculated by the Buneman-Boris method [43]. (Sec. 4.4)

Step 6. Time is advanced by the time step Δt (Sec. 4.4). The new velocity and the new position of the test particle are updated,

$$\mathbf{v}_a(t + \Delta t) = \mathbf{v}_a(t) + \Delta \mathbf{v}^{\text{Coll}} + \Delta \mathbf{v}^{\text{Gyro}}, \quad (4.1)$$

$$\mathbf{r}(t + \Delta t) = \mathbf{r}(t) + \mathbf{v}_a(t)\Delta t. \quad (4.2)$$

For general simulations with many test particles, we iterate the basic steps above at every collision event for each test particle.

Our model can be applied to any scale system, because only the local values of the background plasma parameters are referred to through the basic collision processes above.

Numerical efficiency of the model is mainly determined by the number of test particles used. The efficiency is the trade-off with the statistical accuracy and the spatial resolution for the results needed.

4.2 Random velocity sampling from distorted Maxwellian (Step 3)

In order to choose randomly a background ion velocity from the distorted Maxwellian distribution in Eq. (2.50 or 4.6), we can use almost the same algorithm as presented in the previous Chapter 3.

4.2.1 Preparation

As in Ref. [50], we introduce two coordinate systems for the velocity space, called ‘‘System I’’ and ‘‘System II’’. We distinguish variables belonging to System I and II by using subscripts I and II, respectively. The coordinates for System I (X_I, Y_I, Z_I) are those of the laboratory frame at rest. The Z_I -axis is defined along the magnetic field line \mathbf{B} , and the X_I -axis is taken to the direction of the perpendicular temperature gradient $\nabla_{\perp} T_b$. The Y_I -axis is in the diamagnetic direction ($\mathbf{B} \times \nabla_{\perp} T_b$).

In the presence of a temperature gradient $\nabla T_b = \nabla_{\parallel} T_b + \nabla_{\perp} T_b$ ¹, the background heat flux is calculated from Eq. (2.51) such as $\mathbf{q} = -\kappa_{\parallel} \nabla_{\parallel} T_b + \kappa_{\perp} \mathbf{e}_{\parallel} \times \nabla_{\perp} T_b - \kappa_{\perp} \nabla_{\perp} T_b$. We express it in the

¹Given the magnetic field vector \mathbf{B} , an arbitrary gradient is easily separated in the parallel and perpendicular component as, $\nabla_{\parallel} T := \nabla T \cdot (\mathbf{B}/|\mathbf{B}|)$, and $\nabla T_{\perp} := \nabla T - \nabla_{\parallel} T$.

4.2. RANDOM VELOCITY SAMPLING FROM DISTORTED MAXWELLIAN (STEP 3)

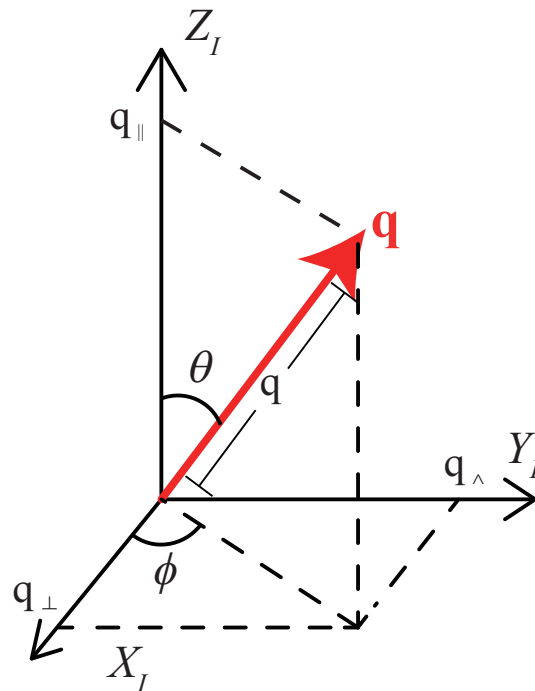


Figure 4.2: Coordinate system: System I (Laboratory frame at rest). (cited from Ref. [30].)

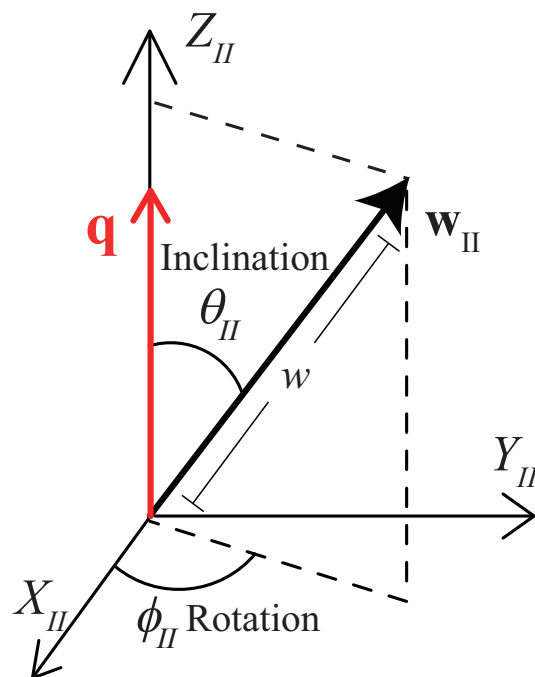


Figure 4.3: Coordinate system: System II based on the heat flux q . (cited from Ref. [30].)

4.2. RANDOM VELOCITY SAMPLING FROM DISTORTED MAXWELLIAN (STEP 3)

laboratory frame (System I) as shown in Fig. 4.2,

$$\mathbf{q} = |\mathbf{q}| \begin{pmatrix} \sin \theta \cos \phi \\ \sin \theta \sin \phi \\ \cos \theta \end{pmatrix}, \quad (4.3)$$

where $\theta := \cos^{-1}(q_{\parallel}/q)$ and $\phi := \tan^{-1}(q_{\wedge}/q_{\perp})$. On the basis of such \mathbf{q} , we define the coordinate System II ($X_{\text{II}}, Y_{\text{II}}, Z_{\text{II}}$) so as for the Z_{II} -axis to take the direction of \mathbf{q} . Variable transformation from System II to System I is realized by the following transformation matrix:

$$\mathbf{T}^{\text{II} \rightarrow \text{I}} := \begin{pmatrix} \cos \phi \cos \theta & -\sin \phi & \cos \phi \sin \theta \\ \sin \phi \cos \theta & \cos \phi & \sin \phi \sin \theta \\ -\sin \theta & 0 & \cos \theta \end{pmatrix}. \quad (4.4)$$

Once we have a vector \mathbf{v}_{II} in System II, its expression in System I is obtained by taking the product with $\mathbf{T}^{\text{II} \rightarrow \text{I}}$, i.e. $\mathbf{v}_{\text{I}} = \mathbf{T}^{\text{II} \rightarrow \text{I}} \cdot \mathbf{v}_{\text{II}}$.

4.2.2 Distorted Maxwellian in System II

Background ion velocity \mathbf{v}_{I} in the laboratory frame consists of a flow velocity $\overline{\mathbf{v}}_b$ (a given parameter) and a random velocity of thermal motion \mathbf{w}_{I} , hence $\mathbf{v}_{\text{I}} = \overline{\mathbf{v}}_b + \mathbf{w}_{\text{I}}$. Rather than choosing a value of \mathbf{w}_{I} directly from the distorted Maxwellian in Eq. (2.50), it is easier to determine its expression in System II, \mathbf{w}_{II} , first. Then we convert \mathbf{w}_{II} into \mathbf{w}_{I} . Random velocity \mathbf{w}_{II} is specified by the speed w , the inclination angle θ_{II} that is measured from the Z_{II} -axis, and the rotational angle ϕ_{II} that is measured from the X_{II} -axis, as shown in Fig. 4.3. The rotational transformation matrix $\mathbf{T}^{\text{II} \rightarrow \text{I}}$ does not affect the magnitude of a vector, because its Jacobian determinant $|\det \mathbf{T}^{\text{II} \rightarrow \text{I}}|$ is 1. So we use the symbol w in common to represent the speed of \mathbf{w}_{I} and \mathbf{w}_{II} . The velocity distribution $f_{b,\text{II}}$ of \mathbf{w}_{II} in System II is obtained by,

$$f_b(\mathbf{w}_{\text{I}})d\mathbf{w}_{\text{I}} = f_b(\mathbf{T}^{\text{II} \rightarrow \text{I}} \cdot \mathbf{w}_{\text{II}}) \cdot |\det \mathbf{T}^{\text{II} \rightarrow \text{I}}|d\mathbf{w}_{\text{II}} = f_{b,\text{II}}(\mathbf{w}_{\text{II}})d\mathbf{w}_{\text{II}}. \quad (4.5)$$

Hence,

$$\begin{aligned} f_{b,\text{II}}(\mathbf{w}_{\text{II}})d\mathbf{w}_{\text{II}} &= n_b \left(\frac{m_b}{2\pi T_b} \right)^{\frac{3}{2}} \cdot w^2 \sin \theta_{\text{II}} \cdot \exp \left(-\frac{m_b w^2}{2T_b} \right) \\ &\times \left[1 - \frac{m_b}{n_b} \frac{1}{T_b^2} \left(1 - \frac{w^2}{5v_{th,b}^2} \right) w |\mathbf{q}| \cos \theta_{\text{II}} \right] dw d\theta_{\text{II}} d\phi_{\text{II}}. \end{aligned} \quad (4.6)$$

The distribution function $(f_{b,\text{II}}/n_b)d\mathbf{w}_{\text{II}}$ is decomposed into three parts $f dw$, $g d\theta_{\text{II}}$, and $h d\phi_{\text{II}}$, respectively defined as,

$$f(w)dw := \sqrt{\frac{2}{\pi}} \left(\frac{m_b}{T_b} \right)^{\frac{3}{2}} \cdot w^2 \exp \left(-\frac{m_b w^2}{2T_b} \right) dw, \quad (4.7)$$

4.3. BINARY COLLISION MODEL (STEP 4)

$$g(w, \theta_{\text{II}})d\theta_{\text{II}} := \frac{1}{2} [1 + \alpha \cos \theta_{\text{II}}] \sin \theta_{\text{II}} d\theta_{\text{II}}, \quad (4.8)$$

$$h(\phi_{\text{II}})d\phi_{\text{II}} := d\phi_{\text{II}}/2\pi, \quad (4.9)$$

$$\text{where } \alpha(w, T_b(\mathbf{r}_a), \mathbf{q}(\mathbf{r}_a)) := -\frac{m_b}{n_b} \frac{1}{T_b^2} \left(1 - \frac{w^2}{5v_{th,b}^2} \right) w |\mathbf{q}|.$$

From the relation $(f_{b,\text{II}}/n_b)d\mathbf{w}_{\text{II}} = (fdw)(gd\theta_{\text{II}})(hd\phi_{\text{II}})$, the functions f , g , and h are interpreted as the probability density functions associated with the random variables w , θ_{II} , and ϕ_{II} .

4.2.3 Random sampling of background ion velocity

The three components w , θ_{II} , and ϕ_{II} are randomly chosen from their distributions Eqs. (4.7), (4.8), and (4.9), by the same algorithm described in Chapter 3 (also in Ref. [50]). Then we obtain a random velocity of a background ion in the laboratory frame (System I) by $\mathbf{w}_{\text{I}} = \mathbf{T}^{\text{II} \rightarrow \text{I}} \cdot \mathbf{w}_{\text{II}}$.

For the calculation, we should pay attention to the values of $T_b(\mathbf{r}_a)$, $\mathbf{q}(\mathbf{r}_a)$, and $\mathbf{T}^{\text{II} \rightarrow \text{I}}(\mathbf{r}_a)$ which are dependent on the position of each test particle $\mathbf{r}_a(t)$. They have to be updated, every time the position $\mathbf{r}_a(t)$ changes.

4.3 Binary Collision Model (Step 4)

In order to simulate Coulomb collision between the test particle and the background ion chosen in Sec. 4.2, we use the Monte Carlo Binary Collision Model (BCM) which has been explained in detail in Sec. 3.5. From the relative velocity between the colliding two particles, the BCM calculates the velocity change $\Delta \mathbf{v}^{\text{Coll}}$ of test particles by collision with a background ion.

For application of the BCM, we use a time step of $\Delta t^{\text{BCM}} = \{1/D(v_{th,b})\} \times 10^{-3}$, where $D(u) := q_a^2 q_b^2 n_b (\ln \Lambda) / (8\pi \varepsilon_0^2 \mu_{ab}^2 u^3)$, as used in Refs. [50, 51]. The relative speed u is approximated by the thermal speed of background ion $v_{th,b}$, if it is much faster than the speed of test particle.

4.4 Buneman-Boris method (Step 5)

The Buneman-Boris method is applied to simulate the Larmor gyro-motion of charged test particles in a magnetic field. The velocity change of test particle by the Lorentz force $\Delta \mathbf{v}^{\text{Gyro}}$ is calculated. (Please refer to Ref. [43] for the details.)

4.5. APPLICABILITY LIMITS

The Buneman-Boris method requires to use a time step Δt^{Gyro} which satisfies the inequality $\Omega_a \Delta t^{\text{Gyro}} \ll 1$, where $\Omega_a := q_a |\mathbf{B}| / m_a$ is the cyclotron frequency of the test particle.

4.5 Applicability limits

Our numerical model of thermal force can work with any background velocity distribution which has the structure,

$$f_b(\mathbf{w}) = f_0 [1 + \mathbf{A}(w) \cdot \mathbf{w}], \quad (4.10)$$

where f_0 is the normal Maxwellian, and $\mathbf{A}(w)$ is a known vector which can contain the random speed $w := |\mathbf{w}|$.

However, the classical limit supposed in this study (See Sec. 2.2) requires that the deformation term $f_0 [\mathbf{A}(w) \cdot \mathbf{w}]$ has to be small enough than the Maxwellian f_0 . Applying such restriction to Eqs. (2.50, 2.51), we obtain the applicability limits of the model within the classical limit,

$$|\mathbf{A}(w) \cdot \mathbf{w}| = \left| -\frac{m_b}{n_b} \frac{1}{T_b^2} \left(1 - \frac{w^2}{5v_{th,b}^2} \right) \{ -\kappa_{\parallel} (\nabla_{\parallel} T_b) \cdot \mathbf{w} + \kappa_{\wedge} (\mathbf{e}_{\parallel} \times \nabla_{\perp} T_b) \cdot \mathbf{w} - \kappa_{\perp} (\nabla_{\perp} T_b) \cdot \mathbf{w} \} \right| \ll 1. \quad (4.11)$$

We substitute the thermal speed of background ion $v_{th,b}$ for its random speed w in the relation (4.11), which leads to the typical classical conditions, such as

$$\frac{\lambda_{b,\parallel}}{L_{\parallel}^{\nabla T}}, \frac{r_{b,L}}{L_{\perp}^{\nabla T}}, \frac{1}{\Omega_b \tau_b} \ll 1. \quad (4.12)$$

Here the mean free path of background ions along the magnetic field line is denoted as $\lambda_{b,\parallel}$, the Larmor radius of background ion is $r_{b,L}$. The characteristic lengths along/perpendicular to the magnetic field line are respectively defined as: $L_{\parallel}^{\nabla T} := T_b / |\nabla_{\parallel} T_b|$, and $L_{\perp}^{\nabla T} := T_b / |\nabla_{\perp} T_b|$. The conditions in Eq. (4.12) are the same as the orderings in Eqs. (2.44, 2.45) that we have assumed to solve the kinetic equation Eq. (2.40).

More concretely, the test simulation results in Sec. 4.6 provide a rough criterion for the smallness of $|\mathbf{A}(w) \cdot \mathbf{w}|$. It is better to satisfy the condition

$$|\mathbf{A}(v_{th,b})| v_{th,b} \leq 0.1. \quad (4.13)$$

All test simulations in Sec. 4.6 have been performed within this limit Eq. (4.13)², and the reasonable results of the thermal force have been obtained, as will be shown in Sec. 4.6. This fact means that our model works correctly at least within this criterion.

²The most severe condition is that of Case I-2 with weaker magnetic field $|\mathbf{B}| = 0.1$ T and steeper temperature gradient $\nabla_{\perp} T_b = 300$ eV/m, which gives $|\mathbf{A}(v_{th,b})| v_{th,b} \approx 0.09$.

4.5. APPLICABILITY LIMITS

In the present study, the deformation of the background velocity distribution function caused by the ELM [15], the neo-classical transport [19], the turbulence effect [41], the strong viscosity due to the flow-reversal [14], or any other effects occurring in fusion plasmas than the classical transport are not taken into account. However, our model can be, in principle, still extended by using more sophisticated forms of distribution function. It is an interesting study subject to define appropriate distribution functions to include the above effects.

One currently available way of model extension is to use a more general form of distorted Maxwellian distribution presented in Ref. [44], for the case where $\Omega_b\tau_b$ is arbitrary, $\nabla p \neq \mathbf{0}$, and $\mathbf{E} \neq \mathbf{0}$. It may also be possible to model more realistic background plasma by using the expression of heat flux \mathbf{q} with the heat flux limiter [42].

4.6 Test simulations

To validate our extended numerical model, we have performed the following two types of test simulations.

Test Simulation I: short time scale ($0 \leq \Omega_a t \leq 0.01$). We simulate the time evolution of the average velocity of test particles, in the presence of a perpendicular temperature gradient, for time scales much shorter than the Larmor gyration period of test particles, in order to directly examine the thermal force $\mathbf{F}^{\nabla T}$. In such short time scale simulation, we can easily separate the diamagnetic thermal force from the friction force and the Lorentz force in numerical results.

Test Simulation II: long time scale ($0 \leq \Omega_a t \leq 650$). We solve the trajectories of test particles for a long period of time. The ensemble-average position of test particles is simulated to check the temperature screening effect. As is explained in Ref. [19], the diamagnetic thermal force $\mathbf{F}_\Lambda^{\nabla T}$ drives the guiding center drift of test particles as shown in Fig. 2.6. The test particles move continuously, as a whole, toward $(-\nabla_\perp T_b)$ -direction. Such macroscopic consequence of the thermal force has not been taken into account in any kinetic test particle simulation model so far.

4.6.1 Numerical parameters for test simulation I and II

Table 4.1: Numerical Parameters for test simulations. (cited from Ref. [30].)

Test particle species	\mathbf{W}^{3+}
Initial position of test particles, $\mathbf{r}_{a,i}(t=0)$	$\mathbf{0}$
Initial test particle velocity, $\mathbf{v}_a(t=0)$	$8.84 \times 10^3 \text{ ms}^{-1} \mathbf{e}_X$ (50 eV)
Normalized test particle velocity, $\tilde{\mathbf{v}}_a(t=0)$	$0.09 \mathbf{e}_X$
No. of test particles for test simulation I, N_1	10^6
No. of test particles for test simulation II, N_2	10^4
Background plasma ion species	\mathbf{H}^+
Number density of background ions, n_b	10^{20} m^{-3}
Background flow velocity, $\bar{\mathbf{v}}_b$	$\mathbf{0} \text{ ms}^{-1}$
Temperature at the origin, $T_b(\mathbf{0})$	50 eV
Temperature gradient, ∇T_b	given for each case
Coulomb logarithm, $\ln \Lambda$	15

4.6. TEST SIMULATIONS

Table 4.2: Characteristic time scales. (cited from Ref. [30].)

Magnetic field B	0.1 T (Test I)	1 T (Test II)
Time step for BCM, Δt^{BCM}	2.03×10^{-10} s	2.03×10^{-10} s
Time step for Buneman-Boris method, Δt^{Gyro}	6.40×10^{-7} s	6.40×10^{-8} s
Simulation time step, Δt	2.03×10^{-10} s	2.03×10^{-10} s
Gyration period of test particle, Ω_a^{-1}	6.40×10^{-6} s	6.40×10^{-7} s
Slowing-down time of test particle, τ_s	7.10×10^{-5} s	7.10×10^{-5} s
Energy-exchange time of test particle, τ_E	2.67×10^{-5} s	2.67×10^{-5} s
Total calculated time, t	$0 \leq \Omega_a t \leq 0.01$	$0 \leq \Omega_a t \leq 650$
Collision time of background ions, τ_b	4.91×10^{-6} s	4.91×10^{-6} s
Cyclotron frequency of background ion, Ω_b	9.58×10^6 s $^{-1}$	9.58×10^7 s $^{-1}$
Degree of magnetization, $\Omega_b \tau_b$	47	470

For the test simulations I and II, we use the Cartesian coordinates (X, Y, Z) . The magnetic field \mathbf{B} is along the Z -axis. The perpendicular temperature gradient $\nabla_{\perp} T_b$ is taken along the X -axis.

Numerical parameters used in the test simulation I and II are summarized in Table 4.1. The test particle species is tungsten ion W^{3+} (mass m_a , electric charge q_a). The background plasma ion is hydrogen ion H^+ (mass m_b , electric charge q_b). Electrons are not considered. The plasma temperature at the origin is 50 eV, and the temperature gradient is specified for each simulation case. The number density of background plasma ion is $n_b = 10^{20}$ m $^{-3}$, and the background flow velocity $\bar{\mathbf{v}}_b$ is set to 0. The Coulomb logarithm is taken as $\ln \Lambda = 15$.

Magnetic field and characteristic time scales are presented in Table 4.2. The slowing-down time of the test particle τ_s is defined by,

$$\tau_s := \frac{1}{\left(1 + \frac{m_a}{m_b}\right) \mu(x)} \frac{4\pi\epsilon_0^2 m_a^2 v_0^3}{q_a^2 q_b^2 n_b \ln \Lambda}, \quad (4.14)$$

where $v_0 := |\mathbf{v}_a(t=0)|$, $x := m_b v_0^2 / (2T_b)$, and $\mu(x) := (2/\sqrt{\pi}) \int_0^x \exp(-\xi) \sqrt{\xi} d\xi$. This is a characteristic time scale for a test particle to be slowed down by collisions with background ions. The gyration time scale of the test particle is $\Omega_a^{-1} := (q_a |\mathbf{B}| / m_a)^{-1}$.

The simulation time step is decided by $\Delta t = \min\{\Delta t^{\text{BCM}}, \Delta t^{\text{Gyro}}\}$, where the time step required for the BCM is $\Delta t^{\text{BCM}} = \{1/D(v_{th,b})\} \times 10^{-3}$, and the time step for the Buneman-Boris method is $\Delta t^{\text{Gyro}} = \Omega_a^{-1} \times 10^{-1}$. The time step for BCM Δt^{BCM} has been estimated from the formula in Sec. 4.3 by approximating the relative speed of colliding two particles $u := |\mathbf{v}_a - \mathbf{v}_b|$ by the thermal speed of the background ion $v_{th,b}$, which is much faster than \mathbf{v}_a ($u \approx v_{th,b} \gg v_a$).

4.6. TEST SIMULATIONS

The test simulations are carried out for the case of collisional background plasma, where the heat flux q is specified by the classical formula Eq. (2.51).

Magnetic field strength and number of test particles used in the test simulation I and II

In the test simulation I, we use a weaker magnetic field ($B = 0.1$ T) and a large number of test particles ($N_1 = 10^6$). It enables us to make the diamagnetic thermal force relatively stronger, and take a large ensemble average of the test particle velocity, in order to output and check the acceleration by the diamagnetic thermal force, with negligible Monte Carlo noise. The following facts are being exploited.

1. The magnitude of the diamagnetic thermal force $\mathbf{F}_\wedge^{\nabla T}$ is inversely proportional to that of the magnetic field ($|\mathbf{F}_\wedge^{\nabla T}| \propto |\mathbf{B}|^{-1}$). When $\mathbf{F}_\wedge^{\nabla T}$ becomes stronger, it may be easier to separate the thermal force from the other forces.
2. By weakening the magnetic field, we can reduce the Lorentz force ($|\mathbf{F}^{\text{Gyro}}| \propto |\mathbf{B}|$) which acts in the same direction as the diamagnetic thermal force (Fig. 2.5), at the initial moment of the test simulation I.
3. The thermal force appears after averaging random collisions on the test particle. However, during the short simulated time ($\Omega_a t \approx 0.01$) of the test simulation I, each test particle experiences only a few times of Coulomb collisions. If the number of test particle and the total number of collisions are insufficient, the standard deviation of the value of the averaged velocity of test particles from its mean becomes non-negligible, so we cannot compare the numerical result with its theoretical value, with a good statistical accuracy.

In the test simulation II (Fig. 2.6), we use a typical magnetic field strength for fusion plasma ($B = 1$ T) and a smaller number of test particle ($N_2 = 10^4$). It is because that the temperature screening effect ($|\mathbf{v}^{\text{Scr.}}| \propto B^{-2}$) is still non-negligible when $B = 1$ T, and also that the simulation is performed for a long time scale ($\Omega_a t \gg 100$). Since each test particle collides with background ions much more times than the test simulation I, the collisional force on test particle is sufficiently averaged over the time. Therefore, a smaller number of test particle N_2 is enough to simulate the thermal force as well as the temperature screening effect occurring on a long time scale.

Both test simulations I and II prove the correctness of our model.

4.6.2 Test simulation I – Diamagnetic thermal force –

In the test simulation I with short time scale, simulated time evolution of test particle velocity will be directly compared with the theoretical values of the thermal force calculated from Eq. (2.59). We

4.6. TEST SIMULATIONS

start the simulation by injecting test particles with the initial velocity $\mathbf{v}_a(t=0)$ in the $+X$ -direction (See Table 1). As shown in Fig. 2.5, the diamagnetic thermal force $\mathbf{F}_\wedge^{\nabla T}$ and the Lorentz force $\mathbf{F}^{\text{Gyro}} := q_a(\mathbf{v}_a(t) \times \mathbf{B})$ act on the test particle, initially, in the $(-Y)$ -direction under the presence of perpendicular temperature gradient $\nabla_\perp T_b$ and magnetic field \mathbf{B} . The frictional force \mathbf{F}^0 (not shown in Fig. 2.5) acts in the $-X$ -direction, opposite to the test particle initial velocity. We focus on the Y -component of test particle velocity, in order to see the diamagnetic thermal force $\mathbf{F}_\wedge^{\nabla T}$. We will, first, calculate the velocity changes of each test particle. Next we remove the acceleration by Lorentz force from the simulated results. Finally we compare such results with the theoretical value of thermal force Eq. (2.59).

We test the following three values of temperature gradients,

Case (I-1) $\nabla T_b = 100 \text{ eV/m } \mathbf{e}_X$,

Case (I-2) $\nabla T_b = 300 \text{ eV/m } \mathbf{e}_X$,

Case (I-3) $\nabla T_b = 300 \text{ eV/m } \mathbf{e}_X + 5 \text{ eV/m } \mathbf{e}_Z$.

In Case (I-1) and (I-2), we examine the diamagnetic thermal force $\mathbf{F}_\wedge^{\nabla T}$ alone, focusing on its direction ($\mathbf{F}_\wedge^{\nabla T} \parallel -\mathbf{e}_\wedge$) and magnitude ($|\mathbf{F}_\wedge^{\nabla T}| \propto |\nabla_\perp T_b|$). Then in Case (I-3), we check if the parallel ($\mathbf{F}_\parallel^{\nabla T}$) and diamagnetic ($\mathbf{F}_\wedge^{\nabla T}$) thermal force can be simulated simultaneously under complex temperature gradient having both parallel and perpendicular components.

The magnetic field \mathbf{B} is set to $0.1 \text{ T } \mathbf{e}_Z$. The number $N_1 = 10^6$ of test particles start moving along the X -axis from the coordinate origin $\mathbf{0}$ (Fig. 2.5), with the initial velocity $\mathbf{v}_a(t=0) := \mathbf{v}_0 = \sqrt{3kE_0/m_a} \mathbf{e}_X$, where $E_0 = 50 \text{ eV}$.

During a period of time much shorter than both the Larmor gyration period Ω_a^{-1} and the slowing down time of test particle τ_s ($0 < \Omega_a t < 0.01$, i.e. $0 < t/\tau_s < 0.001$), we calculate the time evolution of the average velocity of test particles $\overline{\mathbf{v}}_a(t)$, defined as,

$$\overline{\mathbf{v}}_a(t) := \sum_{i=1}^{N_1} \mathbf{v}_{a,i}(t) / N_1, \quad (4.15)$$

where $\mathbf{v}_{a,i}(t)$ is the velocity of i -th test particle ($i = 1 \sim N_1$) at the time t .

Before comparison with the theoretical value Eq. (2.59), we remove the acceleration of the Lorentz force from $\overline{\mathbf{v}}_a(t)$. Since the test particle velocity does not change substantially ($\mathbf{v}_i(t) \approx \mathbf{v}_0$) during the simulation (because of $\Omega_a t \ll 1$, and $t/\tau_s \ll 1$), the Lorentz force remains almost constant ($\mathbf{F}^{\text{Gyro}} \approx q_a(\mathbf{v}_0 \times \mathbf{B})$). By removing the Lorentz force, we define the average test particle velocity accelerated only by the thermal force, such as

$$\overline{\mathbf{v}}_a^{\nabla T}(t) := \overline{\mathbf{v}}_a(t) - \{q_a(\mathbf{v}_0 \times \mathbf{B})/m_a\} \cdot t. \quad (4.16)$$

The values of $\overline{\mathbf{v}}_a^{\nabla T}(t)$ will be outputted in the following sections 4.6.2-4.6.2 as simulated results.

4.6. TEST SIMULATIONS

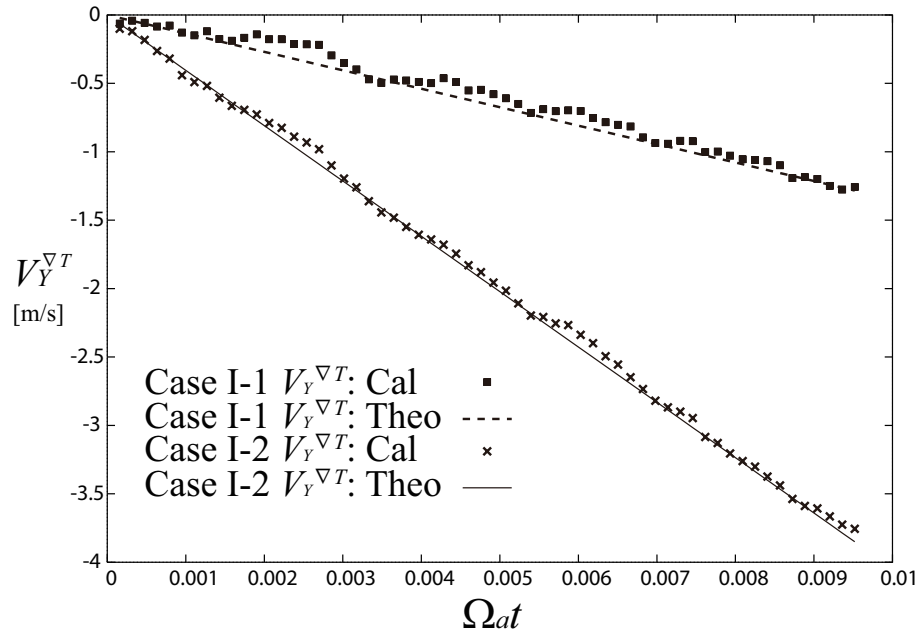


Figure 4.4: Result of Case I-1 and I-2: The Y -component of the average velocity of test particles accelerated only by the diamagnetic thermal force $\overline{v_{a,Y}^{\nabla T}}(t)$. (cited from Ref. [30].)

Results of Case (I-1) and (I-2)

Figure 4.4 shows the Y -component of simulated average velocity without Lorentz force, $\overline{v_{a,Y}^{\nabla T}}(t)$, for the vertical axis, and the normalized time $\Omega_a t$ for the horizontal axis. Closed squares and crosses correspond to Case (I-1) and (I-2), respectively. The theoretical value calculated from Eq. (2.59) by $v_Y^{\nabla T, \text{Theo}} = v_{0,Y} + \{F_{\wedge}^{\nabla T}(\mathbf{v}_0)/m_a\} \cdot t$, is presented by the dashed and solid line for Case (I-1) and (I-2).

In both Cases, the results agree very well with the theoretical acceleration by the diamagnetic thermal force $\mathbf{F}_{\wedge}^{\nabla T}$. The comparison between the results of Case (I-1) and (I-2) shows that the strength of the diamagnetic thermal force is proportional to the magnitude of temperature gradient ($|\mathbf{F}_{\wedge}^{\nabla T}| \propto |\nabla_{\perp} T_b|$).

Result of Case (I-3)

We have already checked our model on the parallel thermal force in Sec. 5.2 (as well as in Refs. [50, 51]), and on the diamagnetic thermal force in the previous Sec. 4.6.2. Here we check the thermal force under the *combined* temperature gradient which has both parallel and perpendicular component, $\nabla T_b = 300 \text{ eV/m } \mathbf{e}_X + 5 \text{ eV/m } \mathbf{e}_Z$. The initial velocity of test particle is the same as in Cases (I-1) and (I-2), i.e. along the X -axis. According to Eq. (2.59), the test particles should be accelerated at once, to the $(-Y)$ -direction by the diamagnetic thermal force (Fig. 2.5), and to the $(+Z)$ -direction by the parallel thermal force (Fig. 2.4).

Figure 4.5 shows the time evolution of the Y -component of simulated test particle speed (closed

4.6. TEST SIMULATIONS

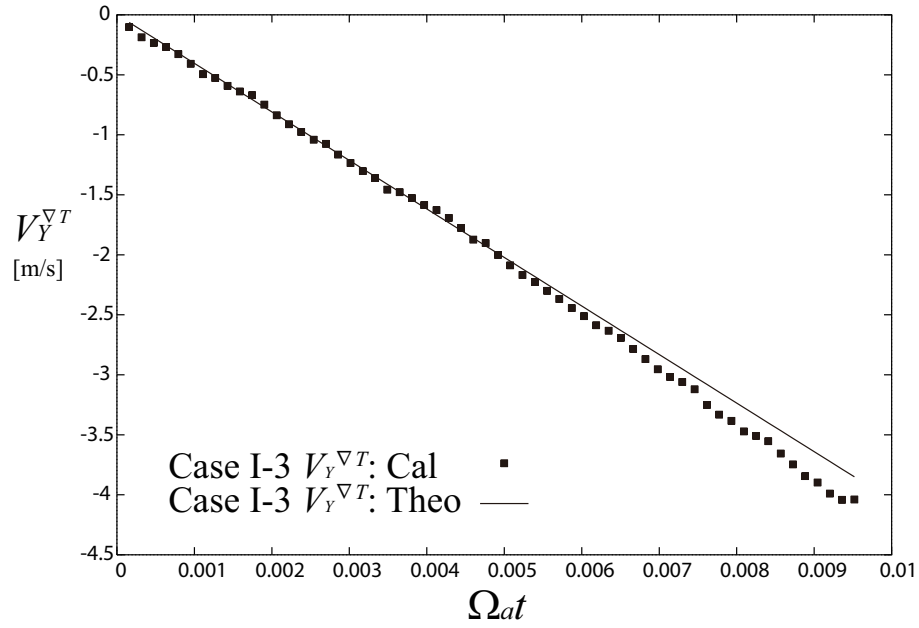


Figure 4.5: Result of Case I-3: The Y -component of the average velocity of test particles accelerated only by the diamagnetic thermal force $\overline{v_{a,Y}^{\nabla T}}(t)$. (cited from Ref. [30].)

squares) without acceleration of the Lorentz force $\overline{v_{a,Y}^{\nabla T}}(t)$. The theoretical value is also plotted as a solid line. The result agrees well with its theoretical value. The diamagnetic thermal force is correctly simulated.

On the other hand, Figure 4.6 presents the simulated Z -component of test particle average velocity $\overline{v_Z}(t)$ by closed squares. The simulated time in the horizontal axis is normalized to the Larmor gyration time scale Ω_a^{-1} and also by the slowing down time τ_s . We can compare the result $\overline{v_Z}(t)$ directly with its theoretical value $(F_{\parallel}^{\nabla T}(\mathbf{v}_0)/m_a) \cdot t$, solid line in the figure, because neither the frictional force \mathbf{F}^0 nor the Lorentz force act in the Z -direction (Fig. 2.4) on the initial condition that $\mathbf{v}_0 \parallel \mathbf{e}_X$ (Fig. 2.4). Good agreement has been obtained. The parallel thermal force $\mathbf{F}_{\parallel}^{\nabla T}$ is correctly simulated simultaneously with the diamagnetic thermal force $\mathbf{F}_{\perp}^{\nabla T}$.

From the results of Cases (I-1), (I-2), and (I-3), it is concluded that our numerical model is able to correctly simulate the thermal force caused by both the parallel and the perpendicular temperature gradient.

4.6.3 Test simulation II – Temperature screening effect –

In the test simulation II, we solve the trajectories of test particles for a relatively long period of time ($\Omega_a t \approx 650$), and discuss whether our kinetic model is able to simulate the temperature screening effect [19].

Two perpendicular temperature gradients have been used,

4.6. TEST SIMULATIONS

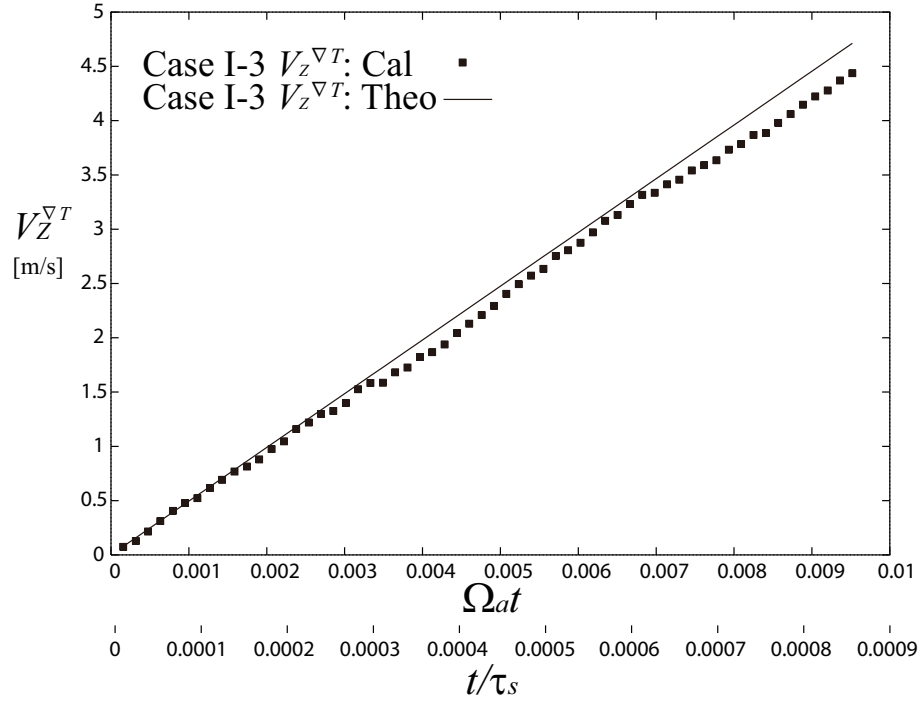


Figure 4.6: Result of Case I-3: The Z -component of the average velocity of test particles accelerated by the parallel thermal force $\overline{v_{a,Z}^{\nabla T}}(t)$. (cited from Ref. [30].)

(II-1) $\nabla_{\perp} T_b = 100 \text{ eV/m } \mathbf{e}_X,$

(II-2) $\nabla_{\perp} T_b = 300 \text{ eV/m } \mathbf{e}_X.$

The number $N_2 = 10^4$ of test particles start from the coordinate origin $\mathbf{0}$. Velocity of each test particle is randomly chosen from the Maxwellian distribution with average energy of $T_a = 50 \text{ eV}$ ($= T_b(\mathbf{r}_a = \mathbf{0})$). We use a magnetic field $\mathbf{B} = 1 \text{ T } \mathbf{e}_Z$. The calculation is performed for a long time ($t \gg \Omega_a^{-1}$) so as for the test particles to gyrate for many times. The other parameters are the same as those presented in Table 4.1 and 4.2.

The transport simulation of tungsten impurities under these values of parameters, which are typical for the SOL-divertor plasma in present tokamaks, is one of the important topics for the fusion research. Normally, a strong perpendicular temperature gradient in the direction toward the core exists close to the separatrix in the SOL-divertor plasma. The temperature screening effect due to such steep temperature gradient, which prevents impurities from penetrating the hot core, might have an impact on the impurity transport in fusion plasmas.

Theoretical value of the temperature screening effect

Before the simulation, we explain the theoretical value of the drift velocity of test particle $\mathbf{v}_a^{\text{Scr}}$ driven by the diamagnetic thermal force $\mathbf{F}_{\wedge}^{\nabla T}$ that we use to check the simulation results. We use the

4.6. TEST SIMULATIONS

fluid estimation of $\mathbf{v}_a^{\text{Scr.}}$ as presented in Ref. [19], because the test particles seem to be relaxed with the background plasma, during the simulation time much longer than the energy-exchange time τ_E of test particle (Table 4.2)³.

Average diamagnetic thermal force acting on a fluid element of the test particle species per unit volume [19] is given by

$$\mathbf{R}^{\nabla T} = -\frac{3n_b}{2\Omega_b\tau_{ba}^{\text{B}}} \frac{\mathbf{B} \times \nabla_{\perp} T_b}{|\mathbf{B}|}, \quad (4.17)$$

with the collision time τ_{ba}^{B} , and the number density of test particle species n_a . The collision time τ_{ba}^{B} is defined by Braginskii [14] as,

$$\tau_{ba}^{\text{B}} := \frac{12\pi^{3/2} \epsilon_0^2 \sqrt{m_b} T_b^{3/2}}{\sqrt{2} n_a q_a^2 q_b^2 \ln \Lambda}. \quad (4.18)$$

We substitute $\mathbf{R}^{\nabla T}$ in the usual formula of guiding center drift, $\mathbf{v}_a^{\text{Scr.}} = (\mathbf{R}^{\nabla T} \times \mathbf{B}) / (m_a n_a \Omega_a |\mathbf{B}|)$, to obtain

$$\mathbf{v}_a^{\text{Scr.}} = -\frac{3}{2} \frac{m_b}{q_a q_b B^2} \frac{n_b}{n_a \tau_{ba}^{\text{B}}} \cdot \nabla_{\perp} T_b. \quad (4.19)$$

The velocity $\mathbf{v}_a^{\text{Scr.}}$ is proportional to the gradient, $\mathbf{v}_a^{\text{Scr.}} \propto -\nabla_{\perp} T_b$.

Here, we have to be careful to use such fluid estimation of $\mathbf{v}_a^{\text{Scr.}}$ to our kinetic test simulation, because there exists theoretical uncertainty in the definition of the Braginskii collision time τ_{ba}^{B} . Originally, the collision time τ_{ba}^{B} has been derived under the condition that $\alpha := n_a q_a^2 / (n_b q_b^2) = 1$. In our kinetic test simulation, however, we do not know exactly the number density n_a of the test particles, neither the value of α ⁴. Even though the Braginskii collision time is widely used [14, 19, 45], we should take care of the fact that the numerical coefficient of τ_{ba}^{B} is dependent on the value of α .

Instead, there is another definition of collision time. The basic collision time τ_{ba}^{T} has been defined by Trubnikov [13] as,

$$\tau_{ba}^{\text{T}} := 8\sqrt{2}\pi \frac{\epsilon_0^2 \sqrt{m_b} T_b^{3/2}}{n_a q_a^2 q_b^2 \ln \Lambda}, \quad (4.20)$$

under the condition that $m_a \gg m_b$. This condition is satisfied in our test simulation II.

In the present study, we use the both collision times τ_{ba}^{B} and τ_{ba}^{T} for estimating the temperature screening effect. They have the same order of magnitude, and are only different in their numerical coefficient, $\tau_{ba}^{\text{B}} : \tau_{ba}^{\text{T}} = 1 : 0.75$. We expect that the both collision times may give reasonable and useful estimations of $\mathbf{v}_a^{\text{Scr.}}$ (Eq. (4.19)), to examine the numerical results.

³The energy-exchange time τ_E is defined by, $\tau_E := \frac{|\tilde{\mathbf{v}}_a|^2}{4} \left(1 + \frac{m_a}{m_b}\right) \tau_s$.

⁴Even though we do not know explicitly the number density of test particle n_a , we can still evaluate the temperature screening effect in Eq. (4.19). The number density n_a disappears as a result of the term $n_a \tau_{ba}^{\text{B}}$ in the denominator.

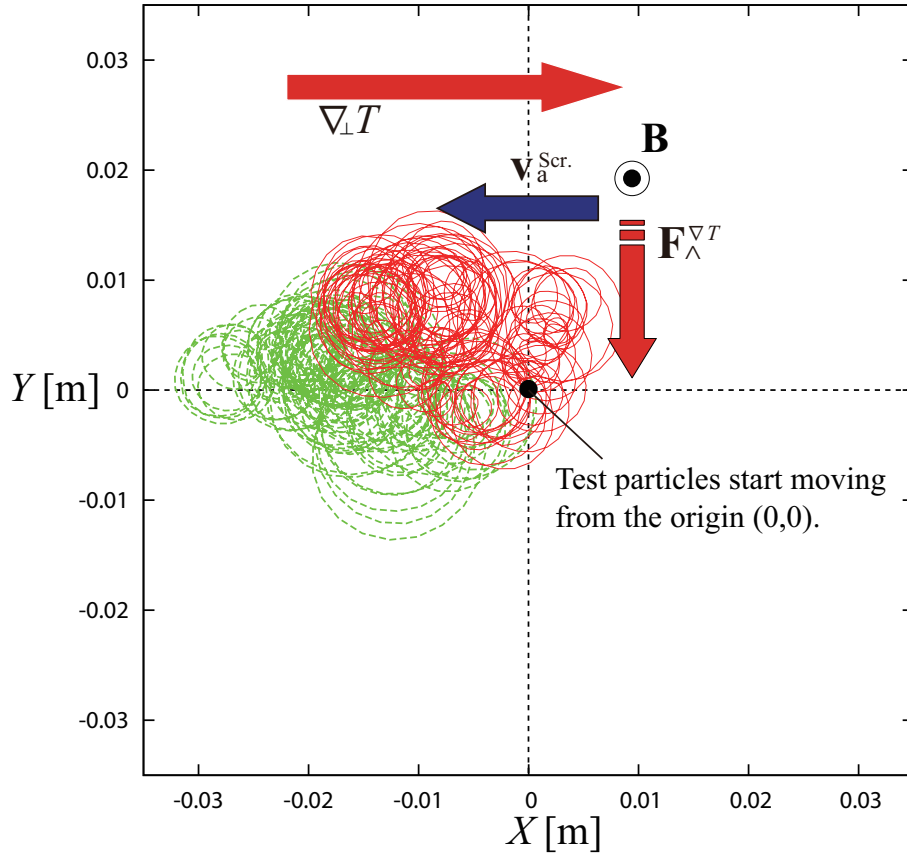


Figure 4.7: Examples of a test particle trajectory in the test simulation II, projected onto the XY -plane. (cited from Ref. [30].)

Example of a test particle trajectory

Prior to the full results, we show some examples of test particle trajectory for better understanding of the situation.

Figure 4.7 shows typical trajectories of test particles, projected onto the perpendicular XY -plane. The dashed line (green) and solid line (red) correspond to the 1st and 2nd test particle, respectively. Their trajectories tend to move gradually toward $(-\nabla_{\perp} T_b)$ -direction, as is expected from Eq. (4.19).

Result of test simulation II

Figures 4.8 and 4.9 show the time evolution of the average position of test particle $\bar{\mathbf{r}}(t)$, respectively for Case (II-1) and (II-2), which is defined as

$$\bar{\mathbf{r}}(t) := \sum_{i=1}^{N_2} \mathbf{r}_{a,i}(t) / N_2, \quad (4.21)$$

where $\mathbf{r}_{a,i}(t)$ is the position of i -th test particle ($i = 1 \sim N_2$) at time t . Closed squares and cross marks represent the value of the X -component $\bar{X}(t)$ and the Y -component $\bar{Y}(t)$ of the average position $\bar{\mathbf{r}}(t)$,

4.6. TEST SIMULATIONS

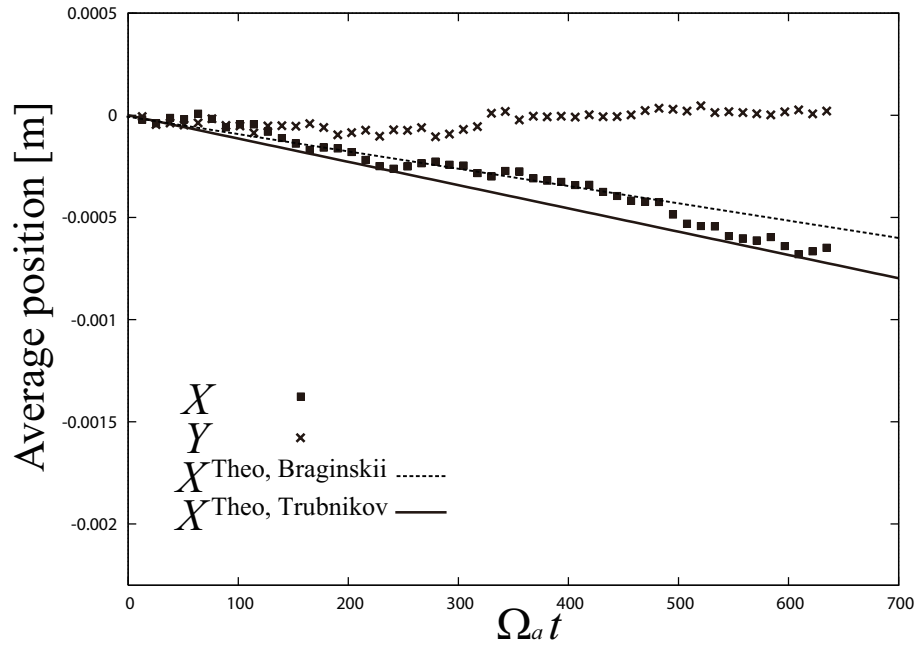


Figure 4.8: Result of Case II-1: Closed squares and cross marks represent the average value of the simulated X -position $\bar{X}(t)$ and the Y -position $\bar{Y}(t)$ of the test particles. The Braginskii estimation using τ_{ba}^B and the Trubnikov estimation by τ_{ba}^T are plotted, respectively by the dashed and the solid line. (cited from Ref. [30].)

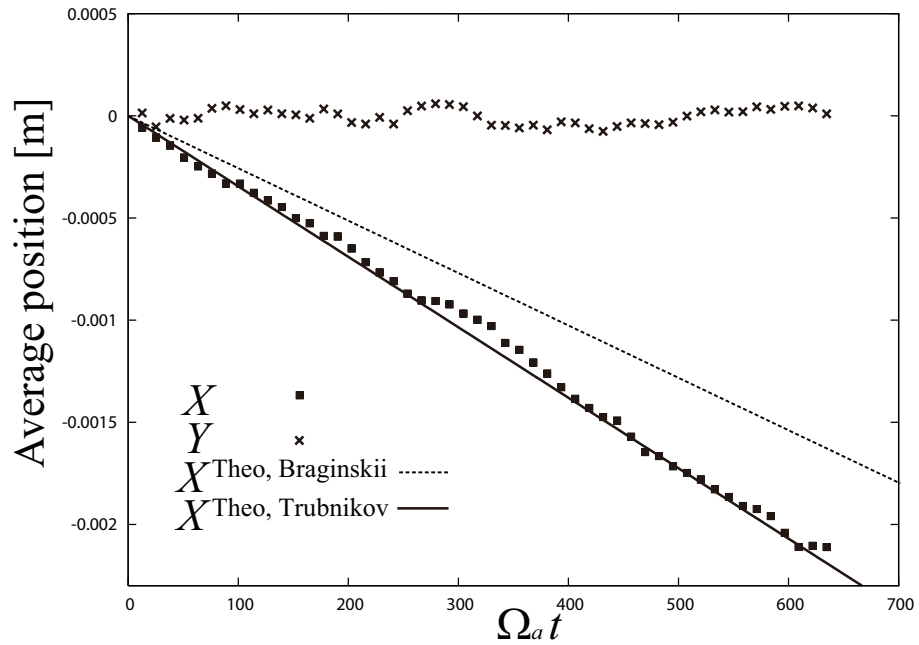


Figure 4.9: Result of Case II-2: Closed squares and cross marks represent the average value of the simulated X -position $\bar{X}(t)$ and the Y -position $\bar{Y}(t)$ of the test particles. The Braginskii estimation using τ_{ba}^B and the Trubnikov estimation by τ_{ba}^T are plotted, respectively by the dashed and the solid line. (cited from Ref. [30].)

4.6. TEST SIMULATIONS

for each case.

In both Cases (II-1) and (II-2), the test particles are clearly moving as a whole toward the $(-X)$ -direction, i.e. to lower temperature region, while its averaged Y -position remains around 0. Furthermore, as the magnitude of temperature gradient increases from Case (II-1) to (II-2), the slope of $\bar{X}(t)$, i.e. the average speed along the X -axis $\bar{v}_{\bar{X}}(t) := d\bar{X}(t)/dt$, is enhanced. From these results, the temperature screening effect is reproduced qualitatively well (for the direction and the magnitude $|\mathbf{v}_a^{\text{Scr.}}| \propto |\nabla_{\perp} T_b|$).

To examine more quantitatively the results in Figs. 4.8 and 4.9, we use Eq. (4.19). By substituting the present parameters (Table 1 and 2, ∇T_b , $T_b(\mathbf{r}) \approx T_b(\mathbf{0}) = 50$ eV) in Eq. (4.19) with the two collision times τ_{ba}^{B} and τ_{ba}^{T} , we obtain the theoretical velocity of guiding center drift as follows,

Case (II-1):

$$\begin{aligned} \mathbf{v}^{\text{Scr.}} &= -1.33 \text{ ms}^{-1} \mathbf{e}_X \text{ (using Braginskii } \tau_{ba}^{\text{B}}), \\ \mathbf{v}^{\text{Scr.}} &= -1.78 \text{ ms}^{-1} \mathbf{e}_X \text{ (using Trubnikov } \tau_{ba}^{\text{T}}), \end{aligned}$$

Case (II-2):

$$\begin{aligned} \mathbf{v}^{\text{Scr.}} &= -4.04 \text{ ms}^{-1} \mathbf{e}_X \text{ (using Braginskii } \tau_{ba}^{\text{B}}), \\ \mathbf{v}^{\text{Scr.}} &= -5.39 \text{ ms}^{-1} \mathbf{e}_X \text{ (using Trubnikov } \tau_{ba}^{\text{T}}). \end{aligned}$$

The theoretical value of X -coordinate x^{Theo} is calculated by $x^{\text{Theo}} = v_a^{\text{Scr.}} \cdot t$. The Braginskii estimation using τ_{ba}^{B} and the Trubnikov estimation by τ_{ba}^{T} are plotted, respectively by the dashed and the solid line in Figs. 4.8 and 4.9. The simulated X -position of test particles $\bar{X}(t)$ shows good agreements with both the Braginskii/Trubnikov estimation in Case (II-1) and Case (II-2), within the ambiguity of theoretical definition of the collision times. Especially, the results agree quite well with the Trubnikov estimation under the present simulation condition.

It has been confirmed that our numerical model is able to simulate the temperature screening effect caused by the perpendicular temperature gradient which may have non-negligible effect on the impurity transport processes in fusion plasmas. In the present tokamak plasmas, the anomalous transport process is considered to have one of the dominant effects on the impurity transport in the radial direction. In many existing impurity transport simulations, the anomalous transport is taken into account. The particle diffusion velocity due to the anomalous transport is estimated from the typical characteristic values as follows. A representative value of the radial anomalous diffusion coefficient is estimated to be $D_{\perp} \sim 0.25 \text{ m}^2\text{s}^{-1}$, according to Refs. [?, 46]. And, if we assume that the characteristic scale length of the impurity number density L_{W} is of the same order as that of the background electrons, then it is estimated as $L_{\text{W}} := |\nabla n_{\text{W}}/n_{\text{W}}|^{-1} = 0.01 \sim 0.1\text{m}$, from Ref. [47]. The anomalous diffusion is of the order of $v^{\text{anomalous}} = D_{\perp}/L = 2.5 \sim 25 \text{ ms}^{-1}$. The temperature screening effect $\mathbf{v}^{\text{Scr.}}$ above is expected to be non-negligible compared with such anomalous diffusion.

4.7 Summary of Chapter 4

We have developed a numerical model of the thermal force for test-ion transport simulation in magnetized plasmas, based on the Monte Carlo Binary Collision Model. When the background plasma has a temperature gradient with parallel ($\nabla_{\parallel}T_b$) and perpendicular ($\nabla_{\perp}T_b$) components to the magnetic field, our kinetic model is able to simulate the thermal force on individual test particle, caused by such temperature gradients. The model is basically the same as presented in previous Chapter 3 for the case without magnetic field, but this time, we have introduced a more extended form of the distorted Maxwellian distribution for the velocity distribution of background plasma ions. The most important part of the model is a numerical method for random sampling of a background plasma ion velocity from the distorted Maxwellian distribution, including the background ion heat flux \mathbf{q}_b caused by the temperature gradient $\nabla_{\parallel}T_b$ and $\nabla_{\perp}T_b$.

In Sec. 2.2, the distorted Maxwellian distribution has been derived on the simple classical conditions that the background plasma is collisional and strongly magnetized (\mathbf{q} is expressed by the classical formula, $\Omega_b\tau_b \gg 1$), and there exist neither pressure gradient nor electric field ($\nabla p = \mathbf{0}$, $\mathbf{E} = \mathbf{0}$). However, our model can be easily further extended to cases without such restrictions (i.e. other suitable formula of \mathbf{q} can be employed, the degree of magnetization $\Omega_b\tau_b$ is arbitrary, $\nabla p \neq \mathbf{0}$, $\mathbf{E} \neq \mathbf{0}$), by using a more general form of distribution function, e.g. those given in Ref. [44].

In order to confirm the validity of the model, we have performed two types of test simulations. In the first test simulation, we have calculated the time evolution of the average velocity of test particles, in the presence of a perpendicular temperature gradient, for time scales much shorter than the test particle Larmor gyration period. The results agreed very well with the theoretical values of acceleration by the thermal force obtained from the kinetic theory.

Then we have performed the second test simulation, for time scales much longer than the test particle Larmor gyration period, in order to check the temperature screening effect caused by the diamagnetic thermal force. The simulated trajectories of test particles have moved, as a whole, toward ($-\nabla_{\perp}T_b$) direction as expected by the theory [19]. We expect that such temperature screening effect may be non-negligible compared with the order of magnitude of the anomalous diffusion in fusion plasmas.

Good agreement of these test simulation results with the theory has shown that our thermal force model is correct and reliable enough to be applied for realistic transport simulations. Our next step is to integrate this model into existing kinetic impurity transport simulation codes (e.g. the IMPGYRO code [26, 48, 49] which solves the full orbit of test impurities by using the BCM for Coulomb collision) for realizing more accurate, reliable impurity transport simulation in nuclear fusion plasmas.

Furthermore, the present BCM-based model can be easily applied to more sophisticated integrated impurity transport simulations which can consider dynamic changes in background fusion plasmas.

Chapter 5

Numerical kinetic model of thermal force based on Fokker-Planck collision operator

We have developed another type of thermal force model for magnetized background plasmas, by using the Fokker-Planck (FP) collision operator to simulate Coulomb collisions. The FP collision operators are obtained on the basis of the study done in the previous Chapters 2, 3, and 4. In addition to the Binary Collision model, the FP method is also widely used (e.g. ASCOT code [46]) because the FP approximation realizes more rapid calculation as far as the trace impurity limit holds. Since almost all the kinetic impurity transport simulation codes for fusion plasmas use either of BCM or FP approximation for Coulomb collision, the FP-based algorithm presented in this chapter will largely expand the applicability of our model.

Model validation are performed to confirm that the FP approximation model can simulate the thermal force as accurately as the BCM-based model in Chapter 4.

5.1 Model description

According to Refs [19, 53], the Coulomb collision process can be modeled by the Fokker-Planck collision operators: the drift vector \mathbf{A} and the diffusion coefficient matrix \mathbf{D} . They are defined by,

5.1. MODEL DESCRIPTION

respectively

$$\mathbf{A} := - \left(1 + \frac{m_a}{m_b} \right) L_{\text{SI}}^{a/b} \nabla_{\mathbf{v}} (\Delta_{\mathbf{v}} \Psi(\mathbf{v}_a)) = \mathbf{F}/m_a, \quad (5.1)$$

$$D_{ij} := -L_{\text{SI}}^{a/b} \frac{\partial^2}{\partial v_i \partial v_j} \Psi(\mathbf{v}_a) = D_{ij}^0 + D_{ij}^{\nabla T}, \quad (5.2)$$

$$D_{ij}^0 = \frac{n_b}{16\pi} \sqrt{\frac{m_b}{2T_b}} L_{\text{SI}}^{a/b} \left(\left[\left(\frac{2}{\tilde{v}} - \frac{1}{\tilde{v}^3} \right) \Phi(\tilde{v}) + \frac{1}{\tilde{v}^2} \Phi'(\tilde{v}) \right] \delta_{ij} \right. \\ \left. + \left[\left(-\frac{2}{\tilde{v}^3} + \frac{3}{\tilde{v}^5} \right) \Phi(\tilde{v}) - \frac{3}{\tilde{v}^4} \Phi'(\tilde{v}) \right] \tilde{v}_i \tilde{v}_j \right), \quad (5.3)$$

$$D_{ij}^{\nabla T} = \frac{m_b}{40\pi T_b^2} L_{\text{SI}}^{a/b} \left(\left[-\frac{3}{2\tilde{v}^5} \Phi(\tilde{v}) + \left(\frac{1}{\tilde{v}^2} + \frac{3}{2\tilde{v}^4} \right) \Phi'(\tilde{v}) \right] \{q_i \tilde{v}_j + q_j \tilde{v}_i + (\mathbf{q} \cdot \tilde{\mathbf{v}}) \delta_{ij}\} \right. \\ \left. + \left[\frac{15}{2\tilde{v}^7} \Phi(\tilde{v}) + \left(-\frac{2}{\tilde{v}^2} - \frac{5}{\tilde{v}^4} - \frac{15}{2\tilde{v}^6} \right) \Phi'(\tilde{v}) \right] (\mathbf{q} \cdot \tilde{\mathbf{v}}) \tilde{v}_i \tilde{v}_j \right). \quad (5.4)$$

The force \mathbf{F} in Eq. (5.1) is the Coulomb collisional force given in Eqs. (2.57), (2.58), and (2.59). The constant $L_{\text{SI}}^{a/b}$ is defined in the SI-unit system $L_{\text{SI}}^{a/b} := (q_a q_b / (m_a \epsilon_0))^2 \ln \Lambda$. The Cartesian coordinates (X, Y, Z) are supposed, and the subscripts i and j in Eqs. (5.3) and (5.4) indicate X -, Y -, and Z -component, respectively. The subscript a of the normalized velocity of test particle $\tilde{\mathbf{v}}_a$ (Eq. (2.61)) has been omitted in Eqs. (5.2), (5.3), and (5.4) for simplicity. The function δ_{ij} is the Kronecker's delta¹. The Rosenbluth potential $\Psi(\mathbf{v}_a)$, already defined in Eq.(2.28), is a function of the test particle velocity $\Psi(\mathbf{v}_a) := -(1/8\pi) \iiint |\mathbf{v}_a - \mathbf{v}_b| f_b(\mathbf{v}_b) d\mathbf{v}_b$. These operators \mathbf{A} and \mathbf{D} describe the time evolution of the velocity distribution of test particle $f_a(\mathbf{v}_a)$ due to Coulomb collisions with background ions, according to the Fokker-Planck equation [53, 17, 19]

$$\left. \frac{\partial f_a(\mathbf{v}_a, t)}{\partial t} \right|_{\text{collisions}} = - \sum_{i=X,Y,Z} \frac{\partial}{\partial v_i} (A_i f_a) + \frac{1}{2} \sum_{i,j=X,Y,Z} \frac{\partial^2}{\partial v_i \partial v_j} (D_{ij} f_a). \quad (5.5)$$

The random velocity change $d\mathbf{v}_a$ of a test particle due to Coulomb collisions with background ions, over a time step Δt_{Coll} , is simulated as follows. Given the background velocity distribution f_b and the test particle actual velocity \mathbf{v}_a , we calculate the operators \mathbf{A} and \mathbf{D} . Since the diffusion coefficient matrix \mathbf{D} is almost always positive-definite, it can be decomposed into a matrix product, i.e. $\mathbf{D} = \mathbf{B}\mathbf{B}^T$, where \mathbf{B} is a lower triangular matrix and \mathbf{B}^T is \mathbf{B} 's transpose (Cholesky decomposition). Then, $d\mathbf{v}_a$ is simulated by the Ito stochastic differential equation [53]: $d\mathbf{v}_a = \mathbf{A}dt + \mathbf{B} \cdot d\mathbf{W}$. The vector $d\mathbf{W}$ is consisting of the Wiener process increment dW_i . Each component dW_i follows the Gaussian probability density distribution with the mean 0 and the variance Δt_{Coll} , and is independent of each other. Finally, the test particle velocity is updated as $\mathbf{v}_a(t + \Delta t_{\text{Coll}}) = \mathbf{v}_a(t) + d\mathbf{v}_a$.

¹ $\delta_{ij} := 1$ if $i = j$, $\delta_{ij} := 0$ otherwise.

5.1.1 Numerical implementation of the model

Numerical implementation of the Fokker-Planck (FP) collision process is easily done. For test simulations in the next Sec. 5.2, we have replaced the Coulomb collision part in the BCM-based simulation algorithm in Fig. 4.1 of previous Chapter 4, by the FP process described above in Sec. 5.1.

5.2 Test simulation

We have performed a series of test simulations to confirm the validity of our FP-based thermal force model and its numerical efficiency.

5.2.1 Test simulation 1: evaluation of the thermal force

The 1st test simulation for checking the thermal force has been performed under the identical conditions as the test simulations I and II in Chapter 4 (also in Ref. [30]). The simulated results on thermal force by temperature gradient $\nabla T_b = \nabla_{\parallel} T_b + \nabla_{\perp} T_b$ are compared with the theoretical value from Eq. (2.59). The results agreed well with the theory, as accurately as the results obtained by our previous BCM-based Coulomb collision model (Almost the same figures as Figs. 4.4, 4.5, and 4.6 of Chapter 4 have been obtained. The results are omitted here.)

In addition, the temperature screening effect (TSE) has been examined. As described in Ref. [30], the TSE is a guiding center drift of test particle by the thermal force, whose drift velocity is analytically estimated [19, 30] as

$$\mathbf{v}_a^{\text{Scr.}} = -\frac{3}{2} \frac{m_b}{q_a q_b B^2} \frac{n_b}{n_a \tau_{ba}^{\text{T}}} \cdot \nabla_{\perp} T_b, \quad (5.6)$$

where τ_{ba}^{T} is the basic collision time defined by Trubnikov [13] $\tau_{ba}^{\text{T}} := 8\sqrt{2}\pi\epsilon_0^2\sqrt{m_b}T_b^{3/2}/(n_a q_a^2 q_b^2 \ln \Lambda)$. This effect may have important impact on test particle transport, especially in the SOL-Divertor region of the tokamak where steep temperature gradients exist. Simulated results (omitted here) have shown good agreements with the theory, just as shown in Figs. 4.8 and 4.9 of Chapter 4 obtained by the BCM-based model. Our present numerical model based on FP operator is able to simulate the thermal force correctly.

5.2.2 Test simulation 2: effective length of collision time step Δt_{Coll} .

The 2nd test simulation focuses on effective length of the simulation time step of collision Δt_{Coll} . All the parameters remain the same as those used in the test simulation case (II-2) in Sec. 4.6.3, except the length of time step Δt_{Coll} , which was originally taken very small $\Delta t_{\text{Coll}} = 2.03 \times 10^{-10}$ s. We have increased Δt_{Coll} , and checked to which extent of Δt_{Coll} the TSE is correctly simulated.

5.3. SUMMARY OF CHAPTER 5

We use the Cartesian coordinate system, where the magnetic field $\mathbf{B} = 1 \text{ T } \mathbf{e}_Z$ is taken along the Z -axis and the perpendicular temperature gradient $\nabla_{\perp} T_b = 300 \text{ eV/m } \mathbf{e}_X$ is along the X -direction. The test particle species is tungsten ion W^{3+} , and the background plasma ion is hydrogen ion H^+ . Electrons are not considered. The plasma temperature $T_b(\mathbf{r})$ at the origin of position ($\mathbf{r} = \mathbf{0}$) is 50 eV. The number density of background plasma ions is $n_b = 10^{20} \text{ m}^{-3}$, its flow velocity $\bar{\mathbf{v}}_b$ is set to $\mathbf{0}$. The Coulomb logarithm is $\ln \Lambda = 15$. More details should be referred to in Ref. [30]. The number of $N = 10^4$ test particles are used. They start moving from the coordinate origin $\mathbf{r} = \mathbf{0}$, with random velocity which are chosen from the Maxwellian distribution of 50 eV. Their trajectories $\mathbf{r}_{a,i}(t)$ and ensemble average of position $\bar{\mathbf{r}}(t) := \sum_{i=1}^N \mathbf{r}_{a,i}(t)/N$, are simulated. The value of X -component \bar{X} of $\bar{\mathbf{r}}(t)$ is compared with its theoretical value $X^{\text{Theo.}}(t)$ calculated from Eq. (4.19).

Simulations have been performed by varying $\Delta t_{\text{Coll.}}$ from $0.001\tau_s$, to $0.50\tau_s$. The slowing-down time τ_s is a characteristic time for a test particle to be slowed down by collisions with background ions, defined as $\tau_s := \{(1 + m_a/m_b) \mu(x)\}^{-1} (4\pi\epsilon_0^2 m_a^2 v_a^3)/(q_a^2 q_b^2 n_b \ln \Lambda)$, where $x := m_b v_a^2/2T_b$, and $\mu(x) := (2/\sqrt{\pi}) \int_0^x \exp(-\xi) \sqrt{\xi} d\xi$.

Simulated results are shown for the cases $\Delta t_{\text{Coll.}} = (1) 0.05 \times \tau_s$, (2) $0.15 \times \tau_s$. Figures 5.1 and 5.3 show typical trajectories of 2 test particles, projected onto the XY -plane, respectively for the case (1) and (2). And figures 5.2 and 5.4 present time evolution of the averaged position \bar{X} and \bar{Y} for each case, where the horizontal axis is the simulated time normalized to the Larmor gyration time $\Omega_a^{-1} := (q_a |\mathbf{B}|/m_a)^{-1}$ and the vertical axis means the traveled distance. Theoretical values $X^{\text{Theo.}}(t) = v_a^{\text{scr.}} t$ and $Y^{\text{Theo.}}(t) = 0$ are also shown in broken lines. In Figs. 5.2 and 5.4, the simulated values \bar{X} and \bar{Y} agree well with their theoretical values. It means that the test particles move toward $(-\nabla_{\perp} T_b)$ -direction, i.e. to the $(-X)$ -direction as a whole, but stay in the Y -direction as is expected by Eq. (4.19). In addition, the trajectories in Figs. 5.1 and 5.3 change their Larmor gyration radius ceaselessly. This feature reflects an important characteristics of Coulomb collision that it acts on test particles continuously over the time because of its long interaction distance.

As a result of test simulations, we have confirmed that, in the range of $\Delta t_{\text{Coll.}} = 0.001\tau_s \sim 0.15\tau_s$, the simulated \bar{X} and \bar{Y} have agreed well with their theoretical value. Beyond $\Delta t_{\text{Coll.}} = 0.15\tau_s$, the both values \bar{X} and \bar{Y} , have started to deviate largely from their theoretical value.

This result is consistent with the criteria mentioned in Refs. [54, 55] that a time step of Fokker-Planck collision method up to $\Delta t_{\text{Coll.}} \approx 0.25\tau_s$ yields sufficiently correct simulation results of Coulomb collision.

5.3 Summary of Chapter 5

The numerical model of the thermal force based on the Fokker-Planck collision operator has been presented. For the model validation, we have performed the same test simulations as those performed

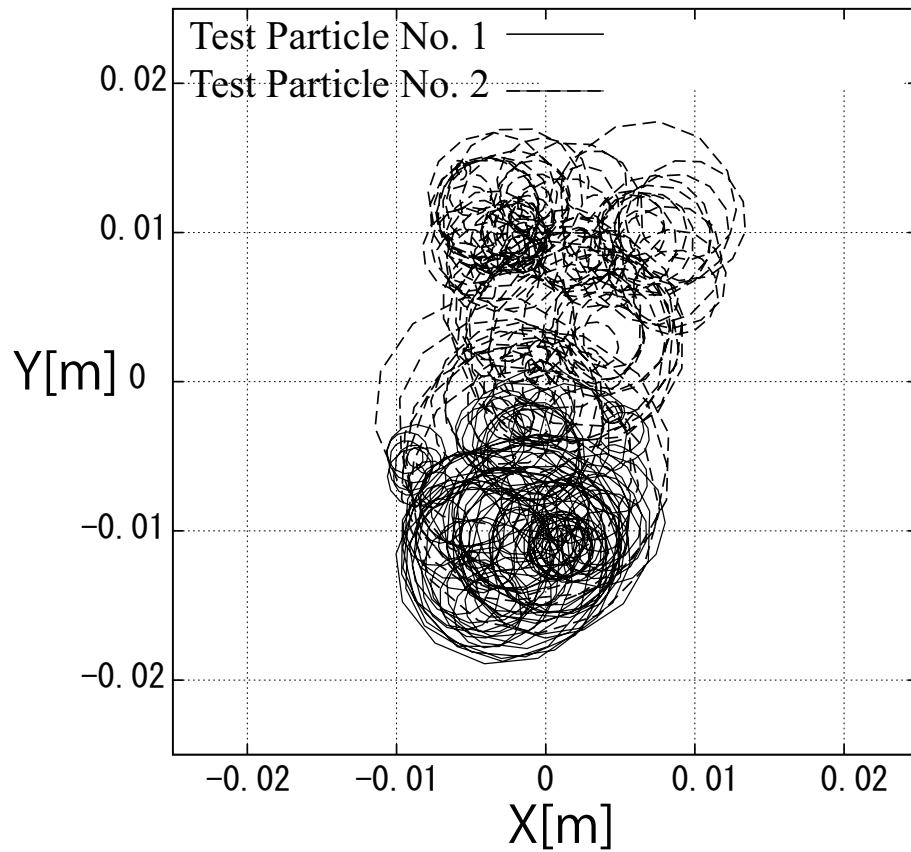


Figure 5.1: Exemplar trajectory of 2 test particles with $\Delta t_{\text{Coll.}} = 0.05\tau_s$. The solid line and broken line correspond, respectively, to the 1st and 2nd test particle. (cited from Ref. [52].)

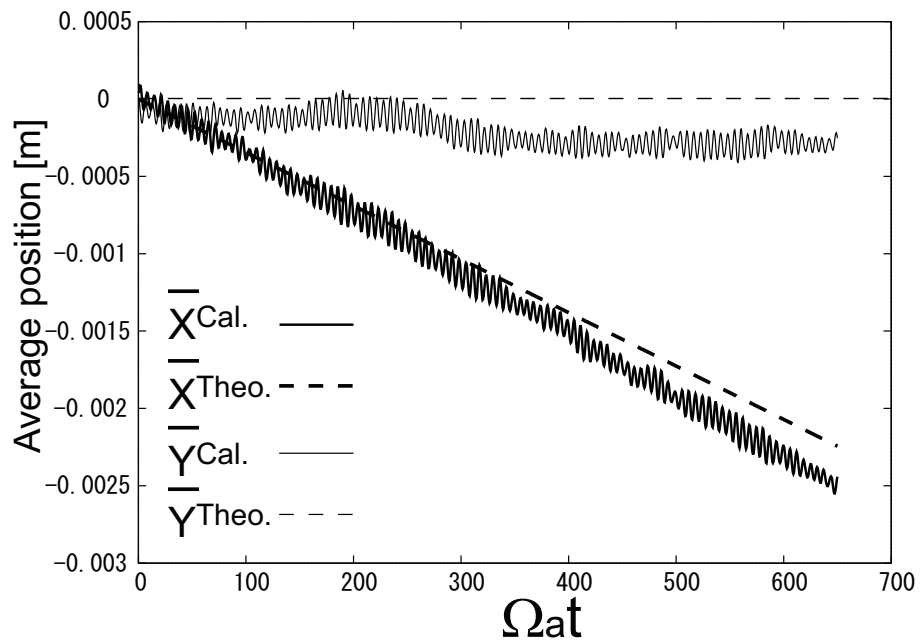


Figure 5.2: Time evolution of average test particle position \bar{X} and \bar{Y} with $\Delta t_{\text{Coll.}} = 0.05\tau_s$. (cited from Ref. [52].)

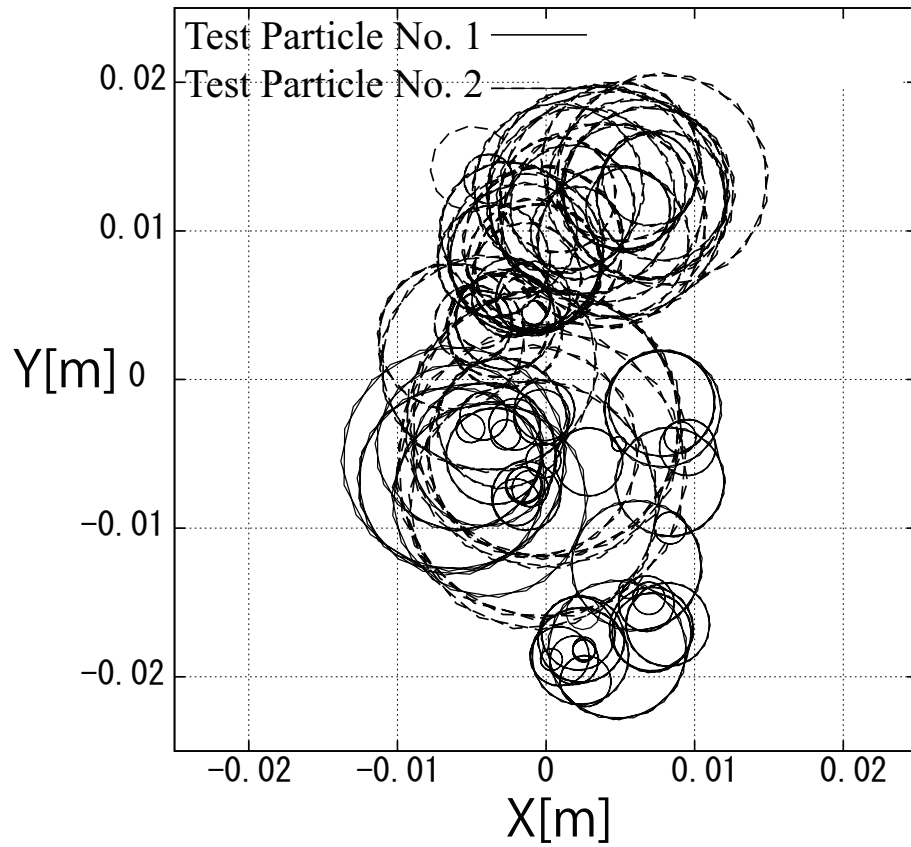


Figure 5.3: Exemplar trajectory of 2 test particles with $\Delta t_{\text{Coll.}} = 0.15\tau_s$. The solid line and broken line correspond, respectively, to the 1st and 2nd test particle. (cited from Ref. [52].)

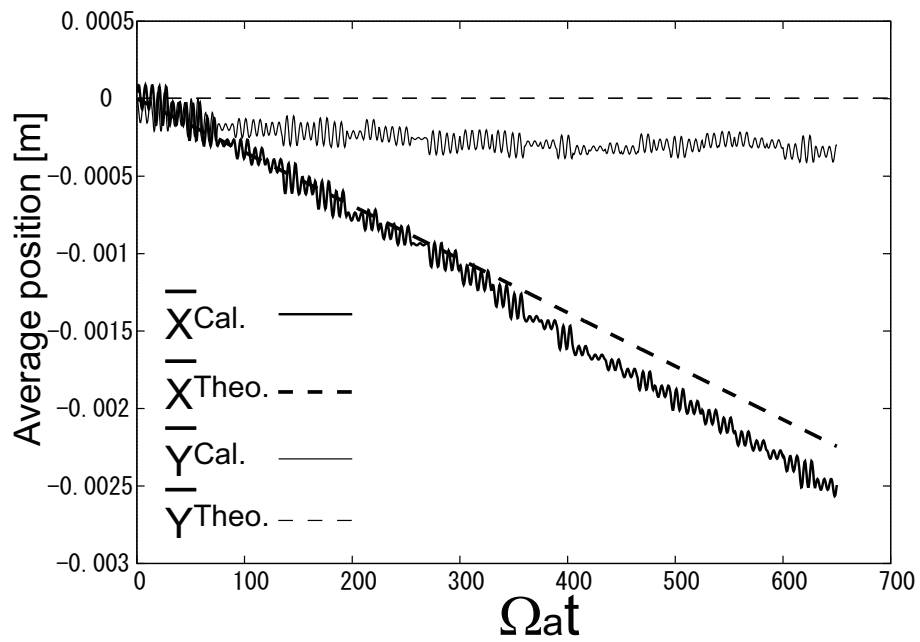


Figure 5.4: Time evolution of average test particle position \bar{X} and \bar{Y} with $\Delta t_{\text{Coll.}} = 0.15\tau_s$. (cited from Ref. [52].)

5.3. SUMMARY OF CHAPTER 5

previously for our thermal force model based on the Binary Collision model (Chapter 4). The results have shown good agreements with the theory. Our numerical model based on the FP collision operator is able to correctly simulate the thermal force caused by both the parallel $\nabla_{\parallel} T$ and the perpendicular $\nabla_{\perp} T$ temperature gradient. The temperature screening effect has also been simulated correctly.

In order to improve numerical efficiency of the model, effective simulation time step of collision has been examined. We have confirmed that, under our test simulation conditions, with collision time step Δt_{Coll} up to about 15 % of the test particle slowing-down time τ_s , our model can simulate the temperature screening effect by thermal force.

Chapter 6

Conclusion

To promote fusion reactions steadily, impurity particles have to be well controlled in order to keep the main fuel plasma hot and dense enough. Correct understanding of impurity transport processes in plasmas is one of the most important research subjects of nuclear fusion. Numerical simulations are widely used to investigate important effects of impurities in fusion plasmas, such as the cooling of core plasma or the mitigation of plasma heat load onto device walls.

In order to improve the impurity transport simulation, we have developed a new numerical model to simulate the thermal force acting on kinetic test-impurity particles. The thermal force is caused by Coulomb collisions with background plasma ions if the plasma has temperature gradient. The motion of impurity particles can be largely influenced by the thermal force. For example, in the parallel direction along the magnetic field line \mathbf{B} , the balance of frictional force and thermal force due to parallel temperature gradient determines the impurity transport. In the perpendicular direction to \mathbf{B} -line, guiding center drift of impurity particles (temperature screening effect, TSE) occurs by the thermal force due to perpendicular temperature gradient. Although the TSE can compete against other transport mechanisms across the \mathbf{B} -field such as the anomalous diffusion, the thermal force and its TSE have not been correctly taken into account in the existing impurity transport simulation codes so far.

Chapter 1 summarizes the motivation and the research subject. Importance of impurity transport process in fusion plasmas is emphasized. Our efforts are devoted to develop a new thermal force model to improve the impurity transport simulations.

Chapter 2 explains the basic theories. The kinetic transport model of charged test particle in plasma, and the Boltzmann equation describing the behavior of background plasma ions are the main physics fields of the study. Coulomb collisions are modeled as a random walk process in velocity change of particles, and background plasma ions with temperature gradient are modeled by the distorted Maxwellian velocity distribution. Averaging all collisions between the test particle and the

plasma ions, the formula of thermal force is analytically derived. Many interesting and important characteristics of the thermal force are presented.

Chapter 3 presents a new numerical model of thermal force in unmagnetized background plasma. Efficient algorithm to randomly sample plasma ion velocities from the distorted Maxwellian has been newly developed. After sampling background ion velocities, Coulomb collisions with the test impurity particles are simulated by the Binary Collision model (BCM). A series of test simulations has been carried out for model validation. The important characteristics of the thermal force in unmagnetized plasma have been examined such as:

- The thermal force pushes the test particles toward hotter plasma region.
- The magnitude of thermal force is directly proportional to the that of background temperature gradient.
- The direction of thermal force is reversed (i.e. toward lower temperature area) when the test particle moves as fast as, or even faster than the thermal speed of background plasma ion. This mechanism prevents the test particles from being infinitely accelerated by the thermal force.
- The direction and magnitude of thermal force is independent of the number density of background plasma ions.

This model is equivalent and applicable to the simulation of thermal force along magnetic field line in magnetized plasmas.

Chapter 4 extends the model to the case of magnetized background plasmas. By adopting more extended form of the distorted Maxwellian, we have succeeded, for the first time, to kinetically simulate the thermal force due to temperature gradient perpendicular to the magnetic field. As in Chapter 3, the BCM is used to simulate Coulomb collisions.

Because of the presence of magnetic field \mathbf{B} , the thermal force becomes anisotropic:

Parallel temperature gradient along the magnetic field line causes the parallel thermal force which acts on each test particle in the same direction as the magnetic field. The parallel thermal force has the same characteristic features as listed above since it is identical with the thermal force in unmagnetized plasma.

Perpendicular temperature gradient with respect to the magnetic field causes the diamagnetic thermal force which acts on test particles in the direction perpendicular to both the magnetic field and the temperature gradient. The diamagnetic thermal force drives the guiding center drift of test particles, which leads to macroscopic transport of test particles across the magnetic field, from higher to lower temperature region of background plasma. It is called temperature screening effect (TSE). The TSE drift velocity may be non-negligible compared with the anomalous diffusion process which has been considered to be dominant to the impurity transport across the \mathbf{B} -field so far.

Test simulations have been performed to check the correct evaluation of parallel and diamagnetic thermal force, as well as the temperature screening effect. All the simulation results have agreed well with the theoretical prediction. Our thermal force model has been confirmed to be able to correctly simulate the thermal force in magnetized fusion plasmas. This extended BCM-based model can be easily applied to more sophisticated integrated impurity transport simulations [48, 49, 56] which can consider dynamic changes in background fusion plasmas.

On the basis of the work done in Chapters 3 and 4, another new thermal force model based on the Fokker-Planck (FP) collision approximation has been developed in Chapter 5. The FP approximation realizes more rapid calculation as far as the trace impurity limit holds. The validity of the model has been checked by comparison with the results obtained in Chapter 4. We have confirmed that the Fokker-Planck version of the model can provide the same simulation results as accurately as the BCM-based model in Chapter 4.

Chapter 6 is the conclusion. Our new model has succeeded to simulate the thermal force due to parallel and perpendicular temperature gradient. Numerical impurity transport simulation in fusion plasmas will be further improved by implementing our model. We hope that this research can contribute to develop an effective way of controlling impurities in fusion plasmas, in order to achieve the net energy production by sustained fusion reactions.

Appendix A

Coulomb logarithm

A.1 Definition of Coulomb logarithm

The integral that appears in Eq. (2.10) diverges logarithmically when the impact parameter ϱ extends to infinity,

$$\begin{aligned}\int_0^\infty \frac{\rho}{\rho^2 + \rho_\perp^2} d\rho &= \lim_{\rho' \rightarrow \infty} \int_0^{\rho'} \frac{\rho}{\rho^2 + \rho_\perp^2} d\rho \\ &= \lim_{\rho' \rightarrow \infty} \left(\ln \frac{\sqrt{\rho'^2 + \rho_\perp^2}}{\rho_\perp} \right) \rightarrow \infty.\end{aligned}\quad (\text{A.1})$$

In the plasma gas, the ions and electrons can freely move because their kinetic energy is too high for their mutual recombination reactions to occur. Therefore, microscopic electric field generated by each ions and electrons is suppressed by such freely moving particles. This is one of the most remarkable features of plasma called *Debye shielding* (Fig. A.1). The Debye shielding effect makes the plasma gas macroscopically neutral, otherwise known as *quasi-neutral* state.

The electric field of individual ion and electron is shielded at the characteristic length, called *Debye length* λ_{Debye} , which is defined as

$$\lambda_{\text{Debye}} = \sqrt{\frac{\epsilon_0 T_b}{q_b^2 n_b}}. \quad (\text{A.2})$$

The incident b -ions passing with the impact parameter larger than λ_{Debye} does not feel anymore the Coulomb interaction force from the fixed a -particle in Fig. 2.1. Therefore, the integration range of the diverging integral in Eqs. (2.10, A.1) can be reduced from $(0 \leq \rho \leq \infty)$ to $(0 \leq \rho \leq \lambda_{\text{Debye}})$. The integral converges with a finite value called *Coulomb logarithm* ($\ln \Lambda$),

$$\ln \Lambda \equiv \int_0^\infty \frac{\rho}{\rho^2 + \rho_\perp^2} d\rho \approx \int_0^{\lambda_{\text{Debye}}} \frac{\rho}{\rho^2 + \rho_\perp^2} d\rho. \quad (\text{A.3})$$

The Coulomb logarithm is one of the most important parameters to characterize plasma. For typical tokamak plasma, the value is about $10 \sim 17$ [18].

A.2. JUSTIFICATION FOR THE VALUE OF COULOMB LOGARITHM TO BE REGARDED AS CONSTANT

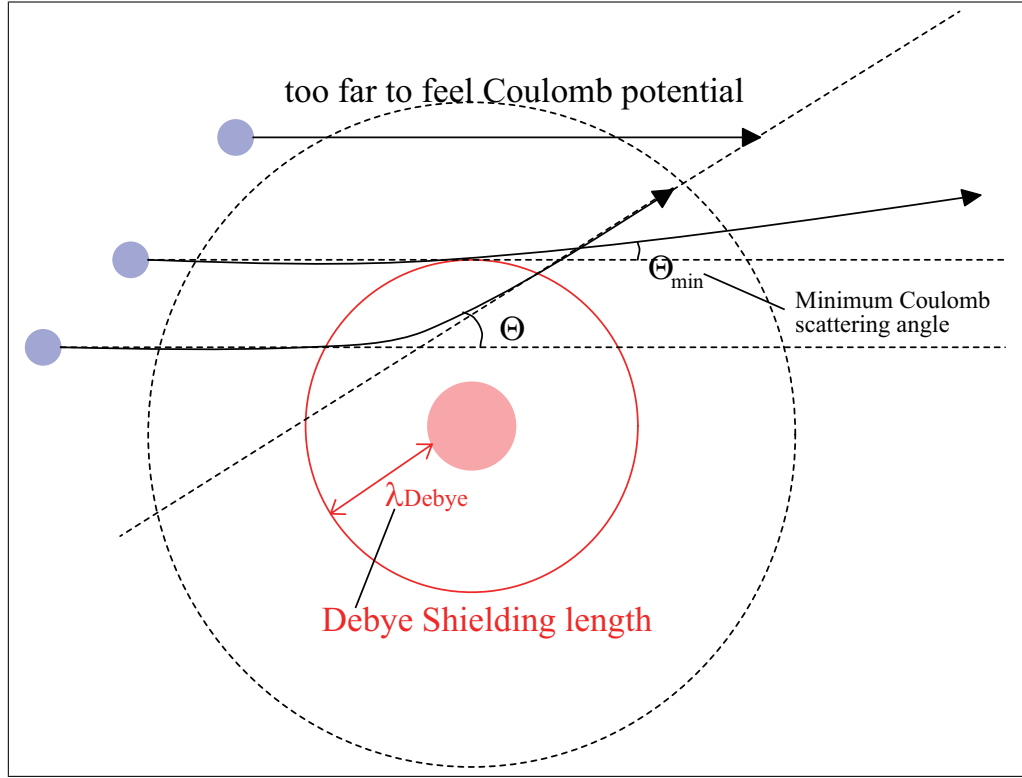


Figure A.1: Debye shielding.

A.2 Justification for the value of Coulomb logarithm to be regarded as constant

In Eq.(2.27), the Coulomb logarithm $\ln \Lambda$ has been treated as constant in the integration over the background b -ion velocities \mathbf{v}_b , although this logarithm depends on \mathbf{v}_b ,

$$\ln \Lambda = \lim_{\rho' \rightarrow \lambda_{\text{Debye}}} \left(\ln \frac{\sqrt{\rho'^2 + \rho_{\perp}^2}}{\rho_{\perp}} \right) \approx \ln \frac{\lambda_{\text{Debye}}}{\rho_{\perp}} = \ln \left(\lambda_{\text{Debye}} \cdot \frac{4\pi\epsilon_0 m_{ab} |\mathbf{v}_a - \mathbf{v}_b|^2}{q_a q_b} \right). \quad (\text{A.4})$$

Eq.(2.4) has been substituted into Eq. (A.4) for the impact parameter ρ_{\perp} for 90° scattering. And we have made use of the fact that the Debye length λ_{Debye} in fusion plasmas is very much larger than ρ_{\perp} : $\lambda_{\text{Debye}} \gg \rho_{\perp}$.¹

Since the logarithm is a slowly varying function, it is usually permitted in fusion plasmas to substitute a mean value $(3/2)(T_a + T_b)$ for the \mathbf{v}_b -dependent term $m_{ab} |\mathbf{v}_a - \mathbf{v}_b|^2 / 2$,

$$\ln \Lambda \approx \ln \frac{\lambda_{\text{Debye}}}{\langle \rho_{\perp} \rangle}, \quad (\text{A.5})$$

$$\langle \rho_{\perp} \rangle = \frac{q_a q_b}{4\pi\epsilon_0 \cdot 3(T_a + T_b)}. \quad (\text{A.6})$$

¹ $\lambda_{\text{Debye}} \approx 0.5 \times 10^{-5}$ m, $\rho_{\perp} \approx 0.5 \times 10^{-12}$ m, $\lambda_{\text{Debye}}/\rho_{\perp} \approx 10^7$, under conditions that $T = 1000$ eV and $n = 10^{21}$ m⁻³. [13]

Appendix B

Sampling of inclination angle θ_{II} from density distribution $g(w', \theta_{\text{II}})$

To sample the inclination angle θ_{II} from the probability density $g(w', \theta_{\text{II}})$ given in Eq. (3.12), we make use of a variable transformation. Firstly, we introduce a variable ζ , defined as $\zeta := \cos \theta_{\text{II}}$. Its density g_{ζ} is then deduced from

$$g_{\zeta}(\zeta) = g(\theta_{\text{II}}(\zeta)) |d\theta_{\text{II}}/d\zeta| = [1 + \alpha\zeta]/2. \quad (\text{B.1})$$

In (B.1), we find that the value of the function $\alpha := \alpha(w, T_b, \nabla T_b)$ determines the profile of g_{ζ} .

If $\alpha = 0$, the distribution g_{ζ} is a uniform distribution for the variable ζ . It is easy to determine the angle θ_{II} .

If $0 < \alpha \leq 1$, the variable ζ is transformed again into η by $1 + \alpha\zeta = \sqrt{\eta}$. The density g_{η} of η is deduced in the following manner,

$$g_{\eta}(\eta) = g(\zeta(\eta)) |d\zeta/d\eta| = 1/(4\alpha). \quad (\text{B.2})$$

The function g_{η} denotes a uniform distribution of η in the interval $[(1 - \alpha)^2, (1 + \alpha)^2]$. Thus, we generate η by using a uniform random number R ($R \sim U[0, 1]$) as, $\eta = 4\alpha R + (1 - \alpha)^2$. Consequently, the value of $\cos \theta_{\text{II}}$ is obtained,

$$\cos \theta_{\text{II}} = \zeta = \frac{\sqrt{4\alpha R + (1 - \alpha)^2} - 1}{\alpha}. \quad (\text{B.3})$$

We can also consider the case of $-1 \leq \alpha < 0$, in the same manner as above, to obtain the results presented in Section 3.3.4.

Appendix C

Examples of numerically sampled distorted Maxwellian distribution

In Figs. C.1, C.2, C.3, and C.4, we show examples of the distorted Maxwellian distribution of background ion velocity in Eq. (2.50) with parallel temperature gradient $\nabla_{\parallel}T$, numerically sampled by our method in Sec. 3.3. Anisotropic distribution in the inclination angle θ_{II} of test particle's random velocity (Fig. 3.4)

$$\mathbf{w} = |\mathbf{w}| \begin{pmatrix} \sin \theta_{\text{II}} \cos \phi_{\text{II}} \\ \sin \theta_{\text{II}} \sin \phi_{\text{II}} \\ \cos \theta_{\text{II}} \end{pmatrix}, \quad (\text{C.1})$$

is clearly shown. We have used the total sampling number $N = 7 \times 10^7$ of particles to obtain each result. The abscissa is the value of normalized inclination angle $\tilde{\theta}_{\text{II}} = \theta_{\text{II}}/\pi$. The ordinate is the normalized number of particles $\Delta N(\theta_{\text{II}})/N$ having the velocities \mathbf{w} being in the range between $w_1 \leq w \leq w_2$, $0 \leq \phi_{\text{II}} \leq 2\pi$, θ_{II} and $\theta_{\text{II}} + d\theta_{\text{II}}$, where w_1 , w_2 and $d\theta_{\text{II}}$ are taken as $w_1 = 0.99v_{th}$ and $w_2 = 1.01v_{th}$ ($v_{th} = \sqrt{T_b/m_b}$), and $d\theta_{\text{II}} = \pi/180$, respectively. The theoretical value of $\Delta N(\theta_{\text{II}})/N$ is obtained from Eq. (3.7) by

$$\left(\frac{\Delta N(\theta_{\text{II}})}{N} \right)_{\text{Theo.}} = \int_{w_1}^{w_2} dw \int_0^{2\pi} d\phi_{\text{II}} f(w, \theta_{\text{II}}, \phi_{\text{II}}) d\theta_{\text{II}}.$$

Four temperature gradients $\nabla_{\parallel}T = 0 \text{ eV/m } \mathbf{e}_Z$, $\nabla_{\parallel}T = 10 \text{ eV/m } \mathbf{e}_Z$, $\nabla_{\parallel}T = 20 \text{ eV/m } \mathbf{e}_Z$, and $\nabla_{\parallel}T = 30 \text{ eV/m } \mathbf{e}_Z$ have been supposed, respectively for Figs. C.1, C.2, C.3, and C.4. The remaining parameters are the same as shown in Table 3.1. Numerically sampled distribution is shown by the bar graph, while the theoretical value is presented by the bold dashed line. As a reference, the normal Maxwellian distribution with $\nabla_{\parallel}T = 0$ is also shown by the thin dashed line.

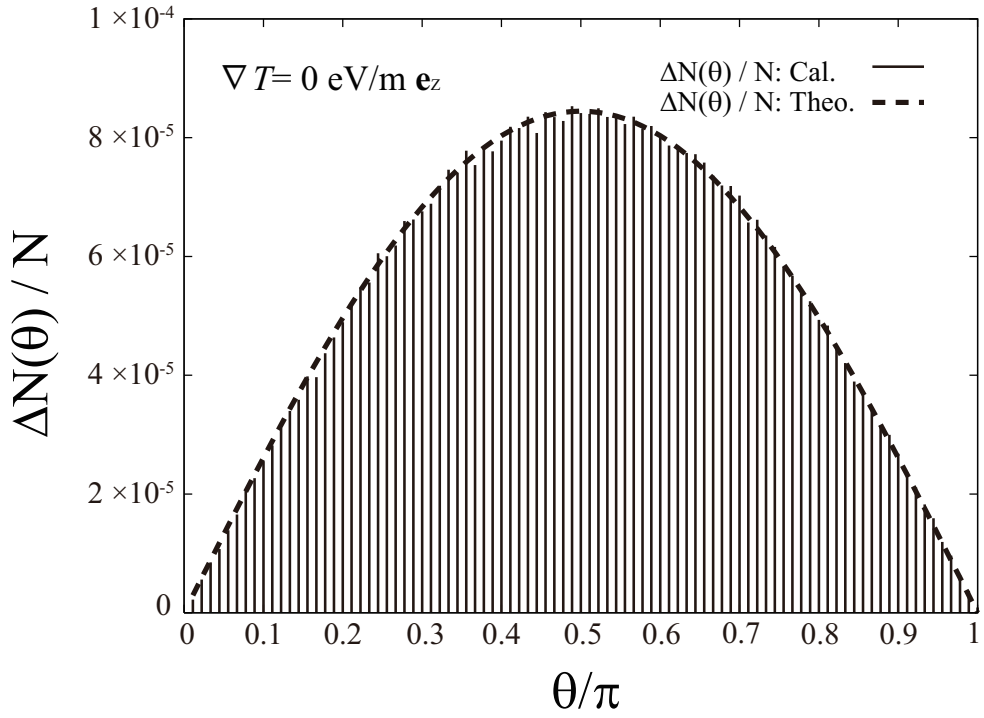


Figure C.1: Velocity distribution under $\nabla T = 0 \text{ eV/m } \mathbf{e}_z$. (cited from Ref. [50].)

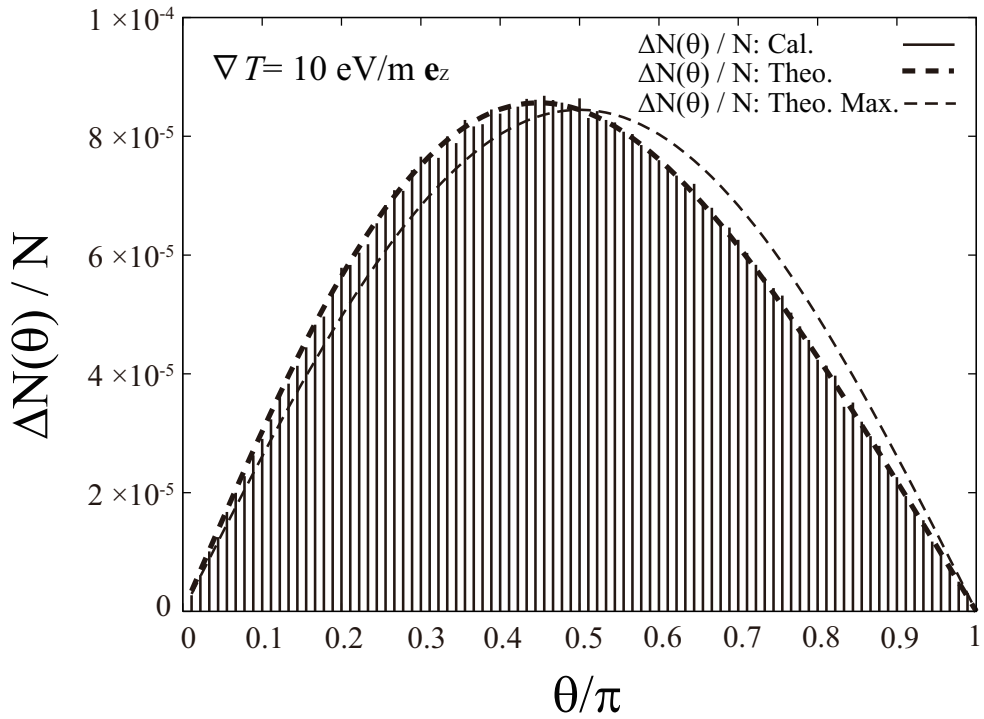


Figure C.2: Velocity distribution under $\nabla T = 10 \text{ eV/m } \mathbf{e}_z$. (cited from Ref. [50].)

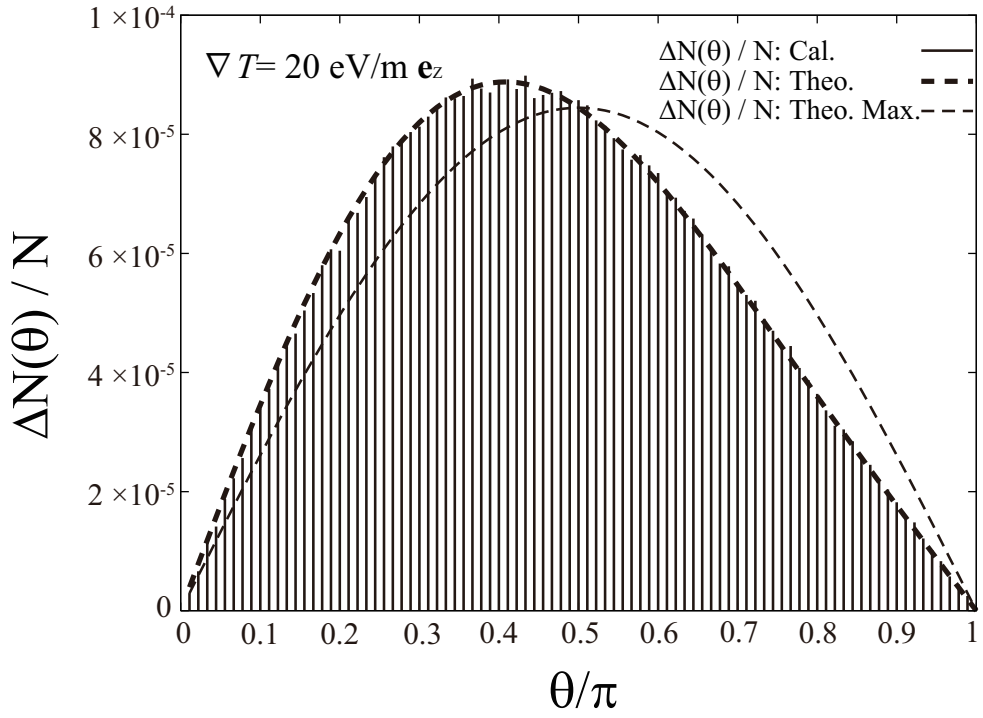


Figure C.3: Velocity distribution under $\nabla T = 20 \text{ eV/m } \mathbf{e}_z$. (cited from Ref. [50].)

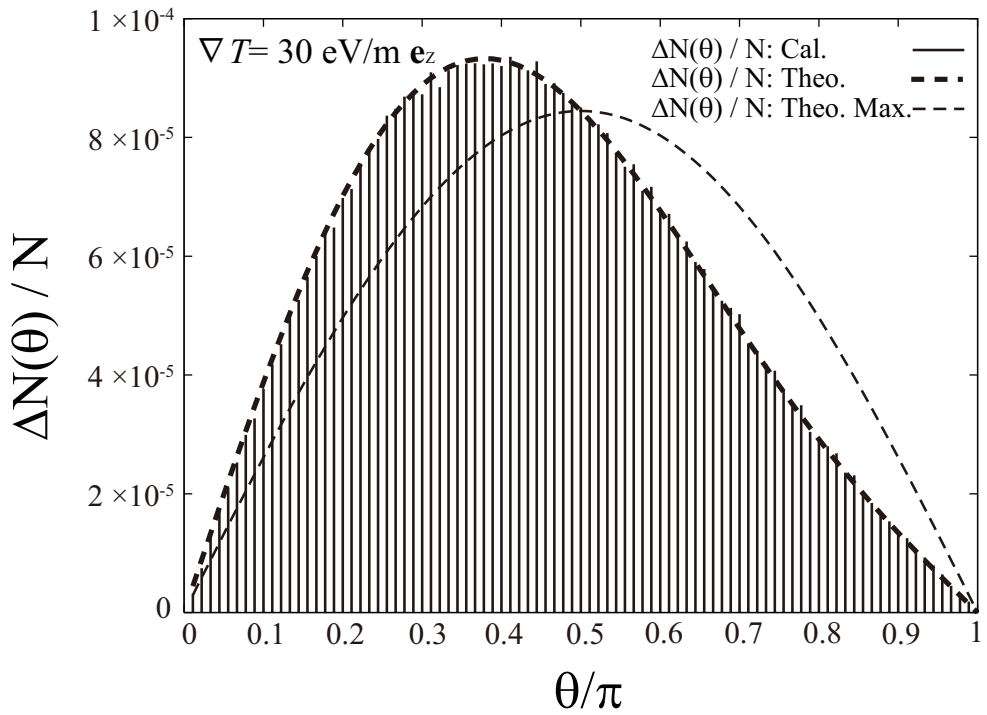


Figure C.4: Velocity distribution under $\nabla T = 30 \text{ eV/m } \mathbf{e}_z$. (cited from Ref. [50].)

Bibliography

- [1] Egbert Boeker, Rienk van Grondelle, *Environmental Physics - Sustainable Energy and Climate Change (Third Edition)*, Wiley, United Kingdom (2011).
- [2] K. Miyamoto, *Controlled Fusion and Plasma Physics*, Taylor & Francis Group, New York (2007).
- [3] T. Fujita, Y. Kamada, S. Ishida, *et al.*, *High performance experiments in JT-60U reversed shear discharges.*, Nuclear Fusion **39** (1999) 1627.
- [4] K. Tobita, the JT-60 Team, *Latest plasma performance and experiments on JT-60U.*, Plasma Phys. Control. Fusion **41** (1999) A333-A343.
- [5] S. Ishida, T. Fujita, H. Akasaka, *et al.*, *Achievement of High Fusion Performance in JT-60U Reversed Shear Discharges.*, Phys. Rev. Lett. **79** (1997) 3917-3921.
- [6] A. Herrmann, O. Gruber, *ASDEX Upgrade - introduction and overview.*, Fusion Science and Technology **44**(3) (2003) 569-577.
- [7] J. Pamela, J. Ongena, *et al.*, *Overview of JET results* , Nuclear Fusion **45** (2005) S63-S85.
- [8] F. Romanelli, R. Kamendjeon, *et al.*, *Overview of JET results* , Nuclear Fusion **49** (2009) 104006, doi:10.1088/0029-5515/49/10/104006
- [9] ITER Physics Basis Editors, *et al.*, Nuclear Fusion **39** (1999) 2137, doi:10.1088/0029-5515/39/12/301
- [10] K. Ikeda, *Progress in the ITER Physics Basis*, Nuclear Fusion **47** (2007).
- [11] Official ITER Website. <http://www.iter.org/>, 2009.
- [12] D. Maisonnier, *European DEMO design and maintenance strategy*, Fusion Engineering and Design **83**(7-9) (2008) 853-864.
- [13] B.A. Trubnikov, *Particle Interactions in a Fully Ionized Plasma, in Reviews of Plasma Physics, Vol.1*, Plenum, New York (1967).

BIBLIOGRAPHY

- [14] S.I. Braginskii, *Transport Processes in a Plasma, in Reviews of Plasma Physics, Vol.1*, Plenum, New York (1967).
- [15] P.C. Stangeby, *The Plasma Boundary of Magnetic Fusion Devices*, Institute of Physics, Bristol (2000).
- [16] K. Shimizu, T. Takizuka, A. Sakasai, *A review on impurity transport in divertors*, J. Nucl. Mater. **241-243** (1997) 167.
- [17] D. Reiser, D. Reiter, M.Z. Tokar', *Improved kinetic test particle model for impurity transport in tokamaks*, Nucl. Fusion **38** (1998) 165.
- [18] Francis F. Chen, *Introduction to Plasma Physics*, Plenum Press, New York (1974).
- [19] Per Helander, Dieter J. Sigmar, *Collisional Transport in Magnetized Plasmas*, Cambridge University Press, New York (2005).
- [20] K. Hoshino, *Study of Flow Structure and Transport Process of Heavy Metal Impurity in Tokamak Edge Plasmas*, PhD Thesis, Keio University, Japan (2007).
- [21] プラズマ・核融合学会編, 「プラズマエネルギーのすべて」, 日本実業出版社 (2007).
- [22] P.C. Stangeby, C. Farrell, S. Hoskins, *et al.*, *Monte Carlo modelling of impurity ion transport for a limiter source/sink*, Nucl. Fusion **28** (1988) 1945.
- [23] K. Shimizu, H. Kubo, T. Takizuka, *et al.*, *Impurity transport modelling and simulation analysis of impurity behavior in JT-60U*, J. Nucl. Mater. **220-222** (1995) 410.
- [24] J. Hogan, *et al.*, Proc. 16th IAEA Int. Conf. on Plasma Phys. and Controlled Fusion Research (Montreal, 1996) vol. **2** p. 625.
- [25] T.E. Evans, D.F. Finkenthal, M.E. Fenstermacher, *et al.*, *Quantitative comparisons between experimentally measured 2D carbon radiation and Monte Carlo impurity (MCI) code simulations*, J. Nucl. Mater. **266-269** (1999) 1034.
- [26] A. Fukano, M. Noritake, K. Hoshino, *et al.*, *Modeling of multi-dimensional impurity transport in a realistic tokamak geometry*, J. Nucl. Mater. **363-365** (2007) 221-215.
- [27] K. Hoshino, M. Toma, K. Shimizu, *et al.*, *Inward pinch of high-Z impurity in a rotating tokamak plasma: effects of atomic processes, radial electric field and Coulomb collisions*, Nucl. Fusion **51** (2011) 083027.

BIBLIOGRAPHY

- [28] J. Neuhauser, W. Schneider, R. Wunderlich, *et al.*, *Modelling of impurity flow in the tokamak scrape-off layer*, Nucl. Fusion **24** (1984) 39.
- [29] K. Shimizu, T. Takizuka, H. Kawashima, *Kinetic effect of thermal force on impurity transport: Simulation of JT-60SA divertor with integrated divertor code SONIC*, J. Nucl. Mater. **390-391** (2009) 307.
- [30] Y. Homma, A. Hatayama, *Numerical modeling of the thermal force in a plasma for test-ion transport simulation based on a Monte Carlo Binary Collision Model (II) – Thermal forces due to temperature gradients parallel and perpendicular to the magnetic field*, J. Comput. Phys. **250**, 206-223 (2013).
- [31] M.N. Rosenbluth, W.M. MacDonald, D.L. Judd, *Fokker-Planck equation for an inverse-square force*, Phys. Rev. **107** (1957) 1.
- [32] T. Takizuka, H. Abe, *A binary collision model for plasma simulation with a particle code*, J. Comput. Phys. **25** (1977) 205.
- [33] V.E. Golant, *Fundamentals of Plasma Physics*, Wiley, New York (1977).
- [34] T. Takizuka, K. Shimizu, *Impurity transport code based on Monte Carlo techniques (IMPMC)*, ITER Workshop (Proc. Workshop Garching, 1994), ITER JCT, Garching Co-Center (1994).
- [35] S. Sengoku, M. Azumi, Y. Matsumoto, *et al.*, *Effects of metal impurity re-cycling in the scrape-off plasma of a large tokamak*, Nucl. Fusion **19** (1979) 1327.
- [36] J.N. Brooks, *Modeling and Analysis of Erosion and Redeposition For Limiter and Divertor Impurity Control Systems*, Fusion Science and Technology **4** (1983) 33.
- [37] J.N. Brooks, *Two-dimensional impurity transport calculations for a high recycling divertor*, J. Nucl. Mater. **145-147** (1987) 837.
- [38] J. Hogan, *et al.*, Proc. 16th IAEA Int. Conf. on Plasma Phys. and Controlled Fusion Research (Montreal, 1996) **2** 625.
- [39] Jean Jacod, Philip Protter, *Probability Essentials*, Springer-Verlag, New York (2003).
- [40] T. Takizuka, K. Shimizu, *et al.*, *Kinetic modelling of impurity transport in detached plasma for integrated divertor simulation with SONIC (SOLDOR/NEUT2D/IMPMC/EDDY)*, Nucl. Fusion, **49** (2009) 065028.
- [41] A. Hasegawa, M. Wakatani, *Plasma Edge Turbulence*, Phys. Rev. Lett. **50** (1983) 682.

BIBLIOGRAPHY

- [42] W. Fundamenski, *Parallel heat flux limits in the tokamak scrape-off layer*, Plasma Phys. Control. Fusion **47** (2005) R163-R208.
- [43] C. K. Birdsall, A. B. Langdon, *Plasma physics via computer simulation*, Adam-Hilger, New York (1991).
- [44] R. Landshoff, *Transport Phenomena in a Completely Ionized Gas in Presence of a Magnetic Field*, Phys. Rev. **76** (1949) 904-909.
- [45] S.P. Hirshman, D.J. Sigmar, *Neoclassical transport of impurities in tokamak plasmas*, Nucl. Fusion **21** (1981) 1079
- [46] J. Miettunen, T. Kurki-Suonio, T. Makkonen, *et al.*, *The effect of non-axisymmetric wall geometry on 13C transport in ASDEX Upgrade*, Nucl. Fusion **52** (2012) 032001
- [47] K. McCormick, N. Asakura, S. Bosch, *et al.*, *ITER edge database investigations of the SOL width*, J. Nucl. Mater. **266-269** (1999) 99-108.
- [48] M. Toma, K. Hoshino, K. Inai, *et al.*, *Coupled IMPGYRO-EDDY simulation of tungsten impurity transport in tokamak geometry*, J. Nucl. Mater. **390-391** (2009) 207.
- [49] M. Toma, X. Bonnin, K. Hoshino, *et al.*, *Development of Coupled IMPGYRO-SOLPS Codes for Analyzing Tokamak Plasmas with Tungsten Impurities*, Contrib. Plasma Phys. **52** (2012) 450.
- [50] Y. Homma, A. Hatayama, *Numerical modeling of thermal force in a plasma for test-ion transport simulation based on Monte Carlo Binary Collision Model*, J. Comput. Phys. **231**, 3211-3227 (2012).
- [51] Y. Homma, A. Hatayama, *Test simulations of the kinetic model for the thermal force based on the Monte Carlo Binary Collision model*, Contrib. Plasma Phys. **52**, No. 5-6, 505-511, (2012).
- [52] Y. Homma, A. Hatayama, *Numerical modeling of the thermal force for the kinetic test-ion transport simulation based on the Fokker-Planck collision operator*, Contrib. Plasma Phys. (Accepted for publication).
- [53] C. Gardiner, *Stochastic Methods, A Handbook for the Natural and Social Sciences (Fourth Edition)*, Springer-Verlag, Berlin (2009)
- [54] Don S. Lemons, Dan Winske, William Daughton, Brian Albright, *Small-angle Coulomb collision model for particle-in-cell simulations*, J. Comput. Phys. **228** (2009) 1391-1403.
- [55] Bruce I. Cohen, Andris M. Dimits, David J. Strozzi, *A grid-based binary model for coulomb collisions in plasmas*, J. Comput. Phys. **234** (2013) 33-43.

BIBLIOGRAPHY

- [56] M. Toma, X. Bonnin, K. Hoshino, *et al.*, *First Steps Towards the Coupling of the IMPGYRO and SOLPS Codes to Analyze Tokamak Plasmas with Tungsten Impurities*, *Contrib. Plasma Phys.*, Volume **50**, Issue 3-5, p. 392-397 (2010).

Acknowledgement

First of all, I would like to express the deepest appreciation to my supervisor Professor Dr. Akiyoshi Hatayama. He guided me through my Master course and Ph.D. course research, and taught me the joy of science. His knowledge about the plasma physics and the nuclear fusion, his enthusiasm and commitment, and his clear advices have always encouraged me to continue the study. And I also thank him to have given me precious chances to participate in many academic conferences.

I would like to express my gratitude to Professor Dr. Yozo Tamura, Associate Professor Dr. Nobuhiko Nakano, and Associate Professor Dr. Kohei Yokoi of Keio University for their helpful comments on this dissertation.

I would like to thank Dr. Tomonori Takizuka, Dr. Katsuhiko Shimizu, Dr. Nobuhiko Hayashi, and Dr. Kazuo Hoshino for fruitful discussions and comments.

I would like to express my gratitude to Dr. David Coster, Dr. Andreas Bergmann, Dr. Alex Chankin, and Dr. Taina Kurki-Suonio for their effective and careful comments. I also appreciate very much the support from Professor Dr. Sibylle Guenter, Professor Dr. Karl Lackner, Professor Dr. Shinnosuke Obi and Professor Dr. Kohei Itoh who gave me the opportunity to study at Max Planck Institute for Plasma Physics (Garching, Germany) and at Technische Universität München (Garching, Germany) for 6 months, in the framework of ERASMUS MUNDUS BEAM program.

I would like to thank all the members of Hatayama laboratory of Keio University. My campus life was made so cheerful, active and splendid with them. In addition, I would like to thank Dr. Mitsunori Toma and Mr. Shohei Yamoto for providing and maintaining the computational environments.

This work was supported by Grant-in-Aid for JSPS (Japan Society for the Promotion of Science) Fellows.

Finally I would like to show my greatest appreciation to my parents for their support and encouragement.

発表論文

1. 主論文に関連する原著論文

- 1-1. Yuki Homma, Akiyoshi Hatayama, *Numerical modeling of the thermal force in a plasma for test-ion transport simulation based on a Monte Carlo Binary Collision Model (II) – Thermal forces due to temperature gradients parallel and perpendicular to the magnetic field –*, Journal of Computational Physics **250** (2013) 206 - 223.
- 1-2. Yuki Homma, Akiyoshi Hatayama, *Test Simulations of the Kinetic Model for the Thermal Force based on the Monte Carlo Binary Collision Model*, Contributions to Plasma Physics **52** (2012) 505 - 511.
- 1-3. Yuki Homma, Akiyoshi Hatayama, *Numerical Modeling of Thermal Force in a Plasma for Test-Ion Transport Simulation Based upon Monte Carlo Binary Collision Model*, Journal of Computational Physics **231** (2012) 3211 - 3227.
- 1-4. Yuki Homma, Akiyoshi Hatayama, *Numerical modeling of the thermal force for the kinetic test-ion transport simulation based on the Fokker-Planck collision operator*, Contributions to Plasma Physics (Accepted for publication).

2. 国際会議発表

- 2-1. Y. Homma, A. Hatayama, *Numerical modeling of the thermal force for the kinetic test-ion transport simulation based on the Fokker-Planck collision operator* (Poster presentation), 14th International Workshop on Plasma Edge Theory in Fusion Devices (Sep. 23-25, 2013. Dom Polonii, Cracow, Poland).

BIBLIOGRAPHY

- 2-2. Y. Homma, M. Toma, A. Hatayama, *Kinetic Modeling of the Thermal Force Based on the Monte Carlo Binary Collision Model* (Oral presentation),
US-Japan JIFT Workshop on Integrated Modeling and Simulation in Toroidal Plasmas (May 24, 2010. Kyoto University, Kyoto, Japan).

他 3 件

3. 国内学会発表

- 3-1. 本間裕貴, 畑山明聖, 澤田悠, 矢本昌平, 「モンテカルロ二体衝突モデルを用いた新しい熱力モデルによる核融合プラズマ中のテスト不純物粒子輸送シミュレーション」(招待講演), プラズマ・核融合学会第30回年会, 東京工業大学大岡山キャンパス, 東京都 2013年12月5日(木).
- 3-2. 本間裕貴, *Numerical modeling of thermal force for test-ion transport simulation based on Monte Carlo Binary Collision Model – Thermal force due to temperature gradients parallel and perpendicular to the magnetic field –* (口頭発表),
「原型炉に向けた周辺・炉心プラズマ統合モデリングによるダイバータ熱・粒子制御研究」研究作業会, 核融合科学研究所, 岐阜県土岐市 2013年2月21-22日.

他 3 件

4. その他の論文

- 4-1. M. Toma, X. Bonnin, Y. Sawada, Y. Homma, A. Hatayama, K. Hoshino, D. Coster, R. Schneider, *Comparison of kinetic and fluid models for tungsten impurity transport using IMPGYRO and SOLPS*,
Journal of Nuclear Materials **438** (2013) 620 - 624.

他 3 件